The Biomechanics of Pregnancy: Simulating Pregnancy Mechanics, Evaluating Preterm Delivery Interventions, and Measuring *in-vivo* Mechanical Properties

Michael Fernandez

Submitted in partial fulfillment of the
requirements for the degree of
Doctor of Philosophy
in the Graduate School of Arts and Sciences

COLUMBIA UNIVERSITY

2017

ABSTRACT

The Biomechanics of Pregnancy: Simulating Pregnancy Mechanics, Evaluating Preterm Delivery Interventions, and Measuring *in-vivo* Mechanical Properties

Michael Fernandez

Preterm birth is a public health problem affecting almost 15 million newborns each year, with almost one million cases annually being fatal. Despite many decades of research, identifying high-risk pregnancies remains difficult. Even with the therapies currently available to clinicians, 95% of preterm births are seemingly intractable. We see a great opportunity for engineers to collaborate with clinicians to help reduce the adverse health impact of this phenomenon. This work is a multi-faceted contribution to the study of the biomechanical problem of preterm birth. We portray the successful, full-term, pregnancy as a delicate balance of organ geometry, tissue deformation behavior, and the physical interaction between the uterus, cervix, and fetal membranes. The cervix is our focus, as its preterm ripening and dilation are the final pathway to premature delivery. We consider a selection of geometric and material factors, studying their impact on the loading that occurs in the cervix. We also study the mechanical implications of the use of a cervical pessary on the mechanical environment of pregnancy. Our mechanical analyses use a custom parameterized model of the pregnant anatomy, coupled with Finite Element Analysis techniques, to allow for rapid model development. In addition, we present a push towards the *in-vivo* measurement of cervical material properties by way of a phantom study using modern MRI techniques.

Table of Contents

List of Charts, Graphs, Illustrations

Acknowledgements

Thank you to my advisor, Dr. Kristin Myers, for your ongoing guidance, expertise, and encouragement. This work would not have been possible without the help of our clinical collaborators, Drs. Ronald Wapner, Sachin Jambawalikar, Joy Vink, Noelia Zork, Chia-Ling Nhan-Ching, and others. Thanks to Dr. Michael House for all the guidance and insights over the years. Thank you to my undergraduate assistant, Martin Perez-Colon, for your hard work on coding, and to my lab partner, Andrea Westervelt, for your real partnership on the model project presented in this dissertation.

Thanks to Dr. Eduardo Mazza and Alexander Ehret for providing the material model for amnion.

I would like to thank my Ph.D. committee members for their time, guidance, and support.

Dedicated to my parents, grandparents, and great-grandparents,

for nurturing my curiosity.

Preface

This dissertation is an original work of the author, M. Fernandez. The parameterized biomechanical model of pregnancy presented herein was the product of combined efforts by the author and Andrea Westervelt.

The cervical materials were generated by K. Myers based on mechanical test data from excised human tissue [1].

The amnion material model in section 2.7 was developed by A. Ehret at ETH Zurich based on prior work by Burzle and Mazza [2].

1 Introduction

More than half a million babies are delivered preterm in the US each year [3]–[5], and the nearly 12% of infants that are delivered preterm account for as much as 35% of all perinatal deaths [6], [7]. Despite extensive research in the medical community over many decades, current methods to stop preterm birth (PTB) are lacking. Strategies to address known risk factors of PTB in early pregnancy (e.g. genitourinary infection and poor nutrition) have been ineffective, as have drug therapies targeted against uterine contractions, infection, or inflammation [8], [9]. Patients at high-risk for PTB receive progesterone supplementation, a hormonal treatment thought to quiet preterm uterine contractions, but the target mechanism of progesterone treatment is currently unclear [10]. Premature mechanical weakening and shortening of the cervix during pregnancy is thought to be a final common pathway for multiple etiologies of preterm birth (PTB) [11], [12].

Several current PTB interventions appear to be motivated by intuition to reduce mechanical loading on the cervix. These treatments include a cervical cerclage – a surgical suture tied around the cervix — or a cervical pessary, a silicon ring-shaped implant inserted into the vaginal canal, and placed around the cervix to close it. While therapeutic interventions such as progesterone and cervical cerclage/pessary exist, the fact that 95% of PTBs are intractable to current therapies suggests that substantial further research is needed [13].

1.1 Current Clinical Standard for Evaluating PTB Risk

Currently, PTB risk is assessed primarily on the basis of obstetric history [11], with a previous history of spontaneous PTB being the most important factor. Additionally, ultrasound assessment of cervical length is used to screen for short cervix, where a cervical length under 25 mm indicates a high risk for PTB. Deformation in the cervix is called “change” in the clinical setting [11]. The clinician may refer

to three modes of cervical deformation: funneling, effacement, and dilation; the former two are illustrated in Figure 1. Early presentation of funneling or effacement indicates higher PTB risk.

Uterocervical angle, the angle between the uterine wall and the cervical canal, has also been proposed as a PTB risk biomarker. A study by Dziadosz, et al. [14] found that in the cohort studied, uterocervical angle was a better predictor of PTB than cervical length. The Bishop score [15] is less commonly utilized, but it represents an attempt to combine multiple risk factors like cervical geometry, stiffness, and the current deformation state of the cervix into a single value estimate of PTB risk. The bishop score was shown to correlate with PTB in a 2008 study [16].

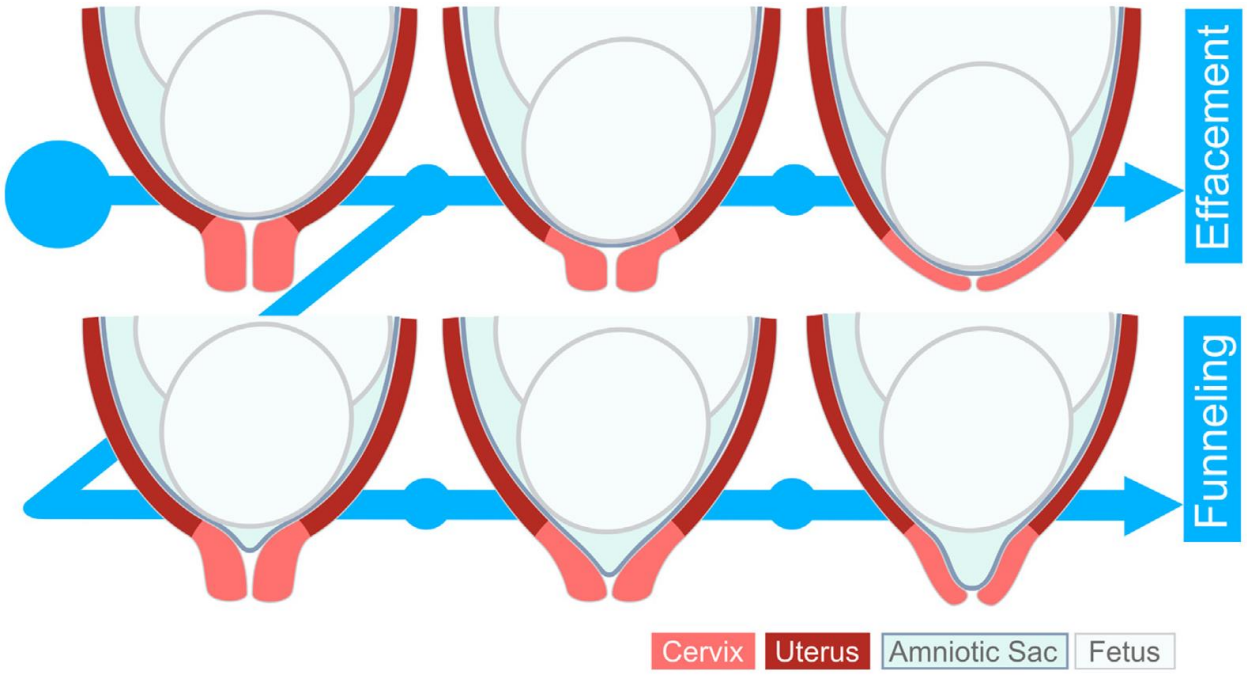

Figure 1: Cervical deformation patterns and clinical definitions: Cervical length is clinically measured as the portion of the cervix that is closed. Effacement progresses in normal pregnancy when the fetal head descends and shortens the cervix. Funneling is a pathologic condition related to an abnormal cervical deformation pattern when the membranes slip into the inner canal and the cervix prematurely shortens. Presented previously by our group in 2015 in the Journal of Biomechanics [17].

From a mechanical engineering perspective, clinical studies often focus too narrowly on one variable (such as cervical length), neglecting the coupled effects of other anatomic geometry, cervical material stiffness, fetal membrane mechanics, and the physical interactions between the uterus, cervix, and

membranes. A mechanical structure's performance depends on its geometry and how its constitutive material(s) respond when subjected to deformation. That is why a coordinated effort between engineers and clinicians is needed in order to develop a full understanding of, and then therapies to address, the problem of PTB.

1.2 Stretch of the Tissue in the Cervix

Though the cervix predominantly comprises collagen, it contains smooth muscle cells capable of expressing chemical signals related to cervical tissue remodeling. Our group hypothesizes that over distention of the cervical smooth muscle may be part of a biochemical chain reaction where over distention occurs, triggering tissue remodeling, leading to softer cervical material properties and therefore more stretch, in a positive feedback loop. Our larger research group is investigating this phenomenon using biochemical assays performed on cervical smooth muscle under strain. Preliminary results indicate that cervical smooth muscle cells "secrete [matrix metalloproteinases], which are thought to be critical for cervical remodeling" [18].

A reactive relationship between distention and remodeling has been hypothesized to exist in uterine tissue, and that hypothesis was tested in a nonhuman primate model by Waldorf, et al. in 2015 [19]. The researchers used an inflatable balloon placed inside the amniotic sac to induce distention of the uterine wall. They found that over-distention was "associated with an inflammatory pulse that precedes and correlates with preterm labor," and concluded that there is evidence "of uterine tissue remodeling and muscle growth as a common, perhaps compensatory, response to uterine distension."

We have chosen to focus on the internal *os* of the cervix, as it is the final common pathway to PTB [11], [12]. This work in biomechanical modeling is one piece of a larger body of work aimed at developing a more thorough understanding of the problem of PTB.

1.3 A Delicate Equilibrium

A successful pregnancy depends on the mechanical function and equilibrium between specific organs and tissues of the reproductive system [20]–[22]. Although individual roles for each of these tissues can be identified, they act not independently, but in cooperation, and they all need to function properly for a pregnancy to last to term. The fetal membranes and uterus (Figure 2) sustain intrauterine fluid pressure (IUP), growing and stretching to accommodate the increasing volume of the fetus. The fetal membrane (i.e. amniotic sac) maintains a sterile growth environment for the fetus in addition to providing mechanical support to the uterus [2], [22]. The cervix acts as a sphincter (a mechanical barrier), with its material stiffness decreasing through extracellular matrix remodeling by about four orders of magnitude over the nine months of gestation, before recovering post-delivery [21], [23].

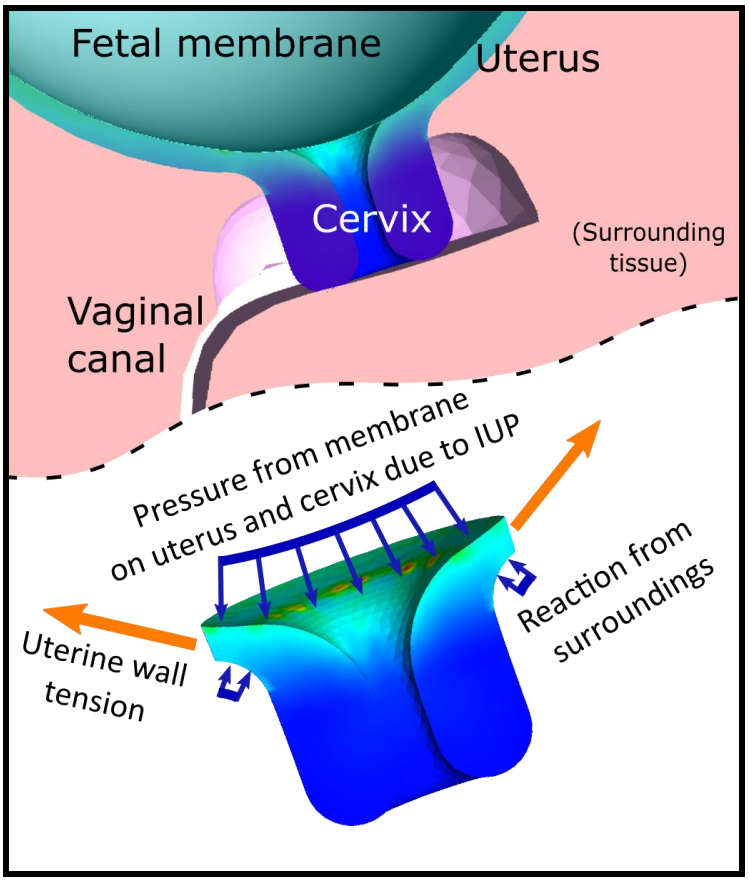

Figure 2: Free body diagram of the cervix in situ. The intrauterine pressure transmitted through the fetal membrane onto the top of the cervix is balanced by tension in the uterine wall and reaction forces from the tissues surrounding the cervix.

In pregnancy, intrauterine pressure (IUP) (Figure 2) acts on the interior of the fetal membranes. Bonded to the uterine wall, and having relatively high material stiffness, the membrane takes some of the load of the IUP but also transmits loading to the uterus. In turn, the uterus provides reaction forces in the form of tensile wall stresses, depicted by the long orange arrows in the lower half of Figure 2. These tensile forces are also present around the cervix where they contribute to an "opening" tensile force at the top of the cervix's internal *os*. The soft tissue contents of the abdomen provide the last notable source of loading on the cervix (Figure 2.3).

1.4 Literature Review

Previous studies have investigated the mechanical loading state of the cervix through finite element models with CAD-based [11], [24], [25] and 2D [20] geometry measured from medical images. House, et al. [24] scanned patients with transabdominal ultrasound and constricted patient-specific 3D geometry using CAD software.

Existing work on FEA modeling of the pregnant anatomy highlights the potential of the method for conducting research on preterm birth. However, current barriers to rapid progress in the area include the difficulty of building realistic finite element models and the lack of availability of appropriate biomechanical material models. Our group has previously developed constitutive relationships for the mechanical deformation behavior of cervical tissue, capturing the tension-compression nonlinearity with a fiber composite material model [1], [26].

According to Mahmoud, et al., finite element modeling is important because "clinical scenarios can be simulated without the use of humans or animals." Promoting a rational and thorough approach to useful model building, Mahmoud et al. discusses the importance of gathering accurate material models and accounting for the complex geometries of pregnancy. A 2D finite element model is presented in this work, serving to illustrate the method's utility in addressing questions in pregnancy biomechanics.

House, et al. constructed 3D FEA simulations from ultrasound images of pregnant patients. House describes the lengthy process of generating models as the greatest limitation to the methodology described in the work. Indeed, he characterizes the conversion of ultrasound images to numerical model as a several-day process. House, et. al consider the clinical standard for cervical strength to be lacking, as "cervical strength assessment is based primarily on clinical history," and note that there is no objective definition for cervical strength based on a biomechanical evaluation.

Paskaleva published a dissertation containing 3D finite element modeling of the pregnant anatomy with the goal of simulating cervical insufficiency through material models featuring growth and remodeling. Her models showed that there were concentrated circumferential loads near the internal cervical *os* especially when the fetal membrane was allowed to slide against the interior uterus. FEA was further used by Paskaleva for evaluation of the placement of cervical cerclage at different positions on the cervix. She found that placing the cerclage closer to the internal *os* resulted in less funneling of the fetal membrane and, hypothetically a more favorable outcome. Her results are consistent with clinical results on cerclage placement. She hypothesizes that "a cerclage placed closer to the internal *os* is more capable of structurally supporting" the load on the cervix.

In this work, we extend the use of FEA in the study of pregnancy in three primary ways. First, we define a standard for detailed geometric characterization of the pregnant uterus and cervix, allowing clinical protocols to be written to produce repeatable measurements and FE model geometries. Second, we describe a method to quickly build, and solve FEA models based on that geometric standard to study how varying specific measurements changes biomechanical loading in the cervix. This addresses the primary roadblocks of model complexity and model assembly time which currently prevent the clinical use of FEA as a diagnostic tool. Finally, we simulate the use of a cervical pessary in the model, evaluating its effect on cervical loading as its placement and angle are varied.

1.5 Vision for New Clinical Tool

Predictive biomarkers like cervical angle and Bishop score are useful but incomplete. There is a need for a quantitative, scientific, and intuitive way for clinicians to take advantage of the available information in each biomarker, and to capture any coupled effects that may arise from geometry and material properties. Our group's aim is to create a tool that takes the most important inputs for cervical mechanical performance, combines the inputs in a simulation, then generates quantitative simulation results that correlate with PTB risk. Such a tool will be clinically accessible, fast, simple, and accurate. It will incorporate all of the most

important uterine and cervical geometric variables, whether relating to geometry, material stiffness, or the interactions between the membrane, uterus, and cervix. The tool will take into account cervical mechanical stiffness while incorporating new discoveries on stretch-mediated cervical remodeling and any other biomarkers that are determined to play a role in cervical performance.

1.6 This Work

Pregnancy is a protected environment and accessing organs to measure anatomical and tissue properties during this time is difficult to impossible. Hence, we combine experimental data and computational tools to calculate and visualize the *in vivo* loading state of the organs that support the fetus during pregnancy. Computing power and computational tools, both in terms of software and hardware, are now highly available and capable of addressing many biomechanical hypotheses relevant to pregnancy, PTB, and therapies meant to treat PTB.

The work in this dissertation is part of a larger effort by our team of collaborating clinicians, radiologists, and engineers to develop a better understanding of the many facets of the process of pregnancy and preterm birth. In this work, we tackle the challenges that arise when generating a mechanical simulation of the pregnant anatomy, including the requirement to meaningfully represent geometry and material properties in a model. In Chapter 2, we use detailed 3D geometry segmented from MRI to build finite element simulations of the pregnant anatomy, studying how loading varies between individual patient models, using different cervical material models, and with and without adhesion between the fetal membrane and the uterine wall. In Chapter 3, we develop a new paradigm for building useful parameterized models of pregnancy biomechanics. From our standardized clinical protocol, anatomic measurements are taken and used to determine the geometry of a parameterized 3D model of the uterus, cervix, membrane, and vaginal canal. We describe a custom-developed software which converts each newly generated model into a simulation which can be solved using FEBio [27], an open source finite element package. Using this streamlined modeling pipeline, we study how variations in cervical geometry affect the patterns of stress

and stretch in the cervix. In Chapter 4, we utilize the model developed in Chapter 3 to perform a detailed mechanical analysis of the cervical pessary, a nonsurgical implant intended to reduce the risk of PTB. Chapter 5 addresses the question of cervical material properties. We present there a detailed study on hydraulic permeability of pregnant and nonpregnant cervical tissue as well as a proof-of-concept study for *in-vivo* characterization of the mechanical property of permeability. Cumulatively, the work presented in this dissertation brings biomechanical modeling tools like FEA closer to reaching their potential of helping patients in the clinic.

2 Biomechanical Pregnancy Model Based on High-Resolution MRI

Preterm birth is a critical health problem affecting more than 15 million infants per year in the U.S. and caused 1 million deaths in 2013 [28]. Preterm infants account for 35% of all perinatal deaths and \$26 billion in health care costs [29]. Although multiple etiologies lead to preterm birth, a short cervix as measured by transvaginal ultrasound is associated with increased risk of preterm birth [30]. Thus, ultrasound measurement of cervical length is a key component of clinical algorithms to prevent preterm birth [30], [31].

Although the clinical significance of a short cervix is well known, there is no clinical consensus to what extent a short cervix is causally related to preterm birth or a consequence of a different pathogenesis. Limiting clinical investigation of cervical shortening is a lack of understanding of the deformation mechanisms leading to a short cervix. The structural antecedents of cervical shortening are not known, so prediction of cervical shortening is not possible. An improved understanding of deformation mechanisms leading to a short cervix is urgently needed to elucidate the etiology of a short cervix and its relation to preterm birth.

Here we present a finite element (FE) study to calculate the stress and strain in the cervix during pregnancy. The models in our study are based on anatomical geometry from MRI and cervical mechanical properties of human cervical tissue [1], [26], [32], [33]. Principal stress and strain patterns in the cervix and lower uterine segment are calculated as a function of cervical length, cervical tissue properties and interaction with the fetal membrane. We pay particular attention to the top of the cervix, called the internal cervical os, because cervical shortening is initiated at this location [34], [35].

An important variable affecting the stress pattern in the cervix is the three-dimensional anatomy of cervix and uterus during pregnancy [24]. Large geometric changes occur with fetal growth, and these changes are poorly understood because pregnancy is a protected environment [36]. Anatomical geometry

is irregular, asymmetric, and different for every pregnancy, and external forces on the uterus and cervix vary between patients as a result of these geometric differences. Those factors make it difficult to discern the detailed mechanical stress state of the organs. Previous studies have investigated the mechanical loading state of the cervix through finite element models with CAD-based [11], [25], [37] and 2D [20] geometry measured from medical images. Our study builds upon past knowledge using anatomy-based models with fewer simplifying geometric assumptions. These new models can help elucidate the effects of asymmetry and anatomical irregularity on resulting stress and strain patterns.

In addition to the complexity of the pelvic geometry, the material response to loading of the tissue plays an equally important role in the mechanical function of the cervix. Material properties of *ex-vivo* tissue samples of the uterus and fetal membrane have been reported by others, with tensile modulus ranging from 0.5 to 2 MPa for the uterus [38] and 2 to 30 MPa for the fetal membrane [39], [40]. The material characteristics of the cervix have been measured by our research group [1], [26], [32], [33], [41], where the tissue material response to loading is nonlinear, time-dependent, and anisotropic. In this study, we consider steady-state mechanical loading of the cervix. We investigate five cervical material models, two neo-Hookean and three fiber composite models, where material parameters are obtained from fitting model equations to equilibrium tension and compression data [1], [32]. One of the most salient features of the equilibrium behavior of cervical tissue is the nonlinearity between tension and compression, where the tensile stiffness is orders of magnitude higher than the compressive stiffness. To account for this nonlinearity, we explore three fiber composite cervical material models, specifically: a non-dispersed fiber model with preferentially aligned collagen fibers directed circumferentially around the cervical canal, an ellipsoidal continuously distributed collagen network model with circumferential preferential alignment, and a random, continuously distributed collagen network model where collagen fibers are recruited in the direction of principal tensile loading.

In this study, we describe the methodology we used to create a 3D finite element model of the lower uterine segment (LUS), fetal membrane, and cervix of two pregnant patients: one at 22 weeks of gestation with a normal cervix length (38 mm) and one at 28 weeks with a short cervix (9 mm). A "short cervix" is defined as a (non-dilated) cervical length $\leq$ 25 mm. We simulate the effects of the intrauterine pressure (IUP), which at baseline levels is clinically called the *uterine tone*. IUP is prescribed as a variable hydrostatic pressure applied to the interior of the fetal membrane. We then model the interaction between the membrane and the uterus and cervix for IUP values spanning the full physiological range [42]. FE results for the two patients are given, and our analysis contrasts the cervical stress and strain patterns between the normal and short cervix geometries using random continuous fiber distribution models for both the LUS and the cervix. Then, we shift focus to the normal cervix model to compare material models for the cervix that feature different levels of complexity and mechanical properties. Lastly, we consider the effect of membrane adhesion and membrane stiffness on the cervix's loading state. Through this modeling effort, we show that the positioning, symmetry, and shape of the organs play a large role in the mechanical stress state of the cervix, where asymmetric features drive large concentrations of stress and strain. We also show that adhesion of the fetal membrane to the LUS and cervix reduces the load on the cervix and that the choice of material model for the cervix will influence the stress and strain in the cervix. These results are examples of the countless opportunities for the study of pregnancy that detailed biomechanical models such as ours make possible.

The pelvic anatomy of pregnancy is complex, and large geometric changes occur with growth of the fetus. The uterine anatomy is somewhat irregular and can be asymmetric. This portion of our modeling work uses true-to-anatomy models with fewer simplifying geometric assumptions. These models can help us understand the effects of asymmetry and anatomical irregularity on resulting stress and strain patterns. We built two finite element biomechanical models of this type based on two clinical case studies.

In addition to the complexity of the pelvic geometry, the material response to loading of the tissue also plays a key role in the mechanical function of the cervix. Material properties of *ex-vivo* tissue samples of amniotic sac have been reported by others, with tensile modulus ranging from 2 to 30 MPa for the amniotic sac [39], [40]. Uterine mechanical properties were adapted from the literature and provide approximate deformation in the uterus. The material characteristics of the cervix have been measured by our research team [1], [32] where the tissue material response to loading is nonlinear, time-dependent, and anisotropic. We considered steady state mechanical loading on the cervix. We investigated five types of cervical material models, two neo-Hookean, and three fiber composite models, where material parameters were obtained from fitting model equations to equilibrium tension and compression data [1], [32]. One of the most salient features of the equilibrium behavior of cervical tissue is the nonlinearity between tension and compression, where the tensile stiffness is orders of magnitude higher than the compressive stiffness. Fiber composite models are able to reproduce this behavior better than simple neo-Hookean materials. These composite models reproduce nonlinear material behavior by emulating fibers that only maintain tension, and are embedded in a compressible, isotropic neo-Hookean ground substance. The tensile response is thereby dominated by the nonlinear collagen fibers while the compressive strength is maintained by the extracellular matrix (ECM) ground substance and the collagen network when fibers are engaged due to Poisson's effect. Here we investigated a single family of preferentially aligned collagen directed circumferentially around the inner canal, a random continuously distributed collagen network model where collagen fibers are recruited in the direction of principal tensile loading, and an ellipsoidal fiber distribution model where the reference configuration featured a continuous fiber distribution with preferentially higher stiffness directed circumferentially around the cervical canal.

We developed a methodology to create a 3D finite element model of the lower uterine segment (LUS), amniotic sac, and cervix of two pregnant patients: one at 20 weeks of gestation with a normal cervix length (38mm) and one at 28 weeks with a short cervix (9mm). We simulated the effects of the IUP, which

at baseline levels is clinically called the *uterine tone*. Buhimschi et al. documented IUP in 40 women at baseline levels, during contractions, and while pushing [43]. We prescribed IUP as a hydrostatic force applied to the interior of the amniotic sac. We then modeled the interaction between the amniotic sac and the uterus and cervix for IUP values spanning the full physiological range. Here, we present FE results for the two patients, comparing and contrasting the cervical stress and strain patterns using a simplified neo-Hookean material model for the LUS and cervix. Then, using the healthy long cervix model, we studied two additional material models for the cervix with varying levels of complexity and different mechanical properties. Lastly, we considered the effect of membrane adhesion on the cervix's loading state. Through this modeling effort, we show that the positioning, symmetry, and shape of the organs play a major role in the mechanical stress state of the cervix, where asymmetric features drive concentrations of stress and strain. We also show that adhesion between the fetal membrane and the LUS and cervix alters the load on the cervix. Lastly, we show that the choice of material model for the cervix influences the stress and strain pattern in the cervix and that accounting for the tension/compression nonlinearity material response of the tissue gives more realistic results.

2.1 Patient Demographic

Eligible patients were recruited and consented under an IRB-approved research protocol at the Columbia University Medical Center. Exclusion criteria included women with premature rupture of membranes, placenta accrete, placenta previa, chorioamnionitis, placental abruption, concerning fetal or maternal status and preterm labor. All scans were approved by the patients' physicians. Patients were compensated for their time. No health complications were reported as a result of this study. Patient demographics and obstetric history are given in Table 1.

Table 1: Patient demographics

	Patient 1	Patient 2
Age	32	25
Gestation Time	22 Weeks	28 Weeks
Gravida	1	3
Parity	0	1
Delivery	39 weeks, 1 day	39 weeks, 2 days

2.2 Data Acquisition and Pulse Sequence

MRI data sets were acquired using a 1.5 Tesla GE HDxt scanner with a 16 channel body coil (the lower half with 8 channels was used). The pulse sequence was a Sagittal T2 Cube, 3D Spin Echo sequence with $TR = 2000\,ms$, $TE = 103\,ms$, and $Echo\ Train\ Length = 60$. The slice thickness was $2.2\,mm$ with a field of view (FOV) of $260{\times}260\,mm^2$ and image resolution of $512{\times}512$ for each slice. With a slice gap of 1.1 mm, this resulted in voxelized data with 1.1 x 0.55 x 0.55 mm^3 resolution over a FOV of 90 x 260 x 260 mm^3 in the sagittal, axial, and coronal directions, respectively. This pulse sequence was chosen to achieve high image resolution with a large FOV while minimizing patient discomfort (scanning time was approximately 6 minutes and required no breath holding).

2.3 Segmentation of MRI Data

The MRI image stack was loaded into the Simpleware ScanIP software (Version 6.0, Exeter, UK). We identified the uterus and cervix within the image volume, and manually segmented the organ in each image slice. In general, fluids and tissues with increased water content show up brighter on T2 images. Tissues with low proton density, or fibrous tissues, show up darker. Cervical stroma is noticeably darker on the scans than the cervical mucous plug, amniotic fluid, and the bladder. The uterine wall can also be seen as a slightly darker band within the images, and it surrounds the fetus and placenta. In areas where the uterus was not clearly visible due to patient movement or low contrast, the tissue was assumed to be

continuous with constant thickness and to connect to the visible regions of tissue in agreement with other anatomical constraints.

Each segmented pixel on a given slice generates a voxel in the 3D model, and adjacent voxels connect to form the 3D shape of the segmented volume. After segmenting each slice, we employed Gaussian smoothing filters (with a radius between 0.5 and 5 mm) to reduce noise in the segmented model. A smooth surface is required for successful volume element formation. The segmented volumes are shown for each patient with a sagittal cutaway in Figure 3.

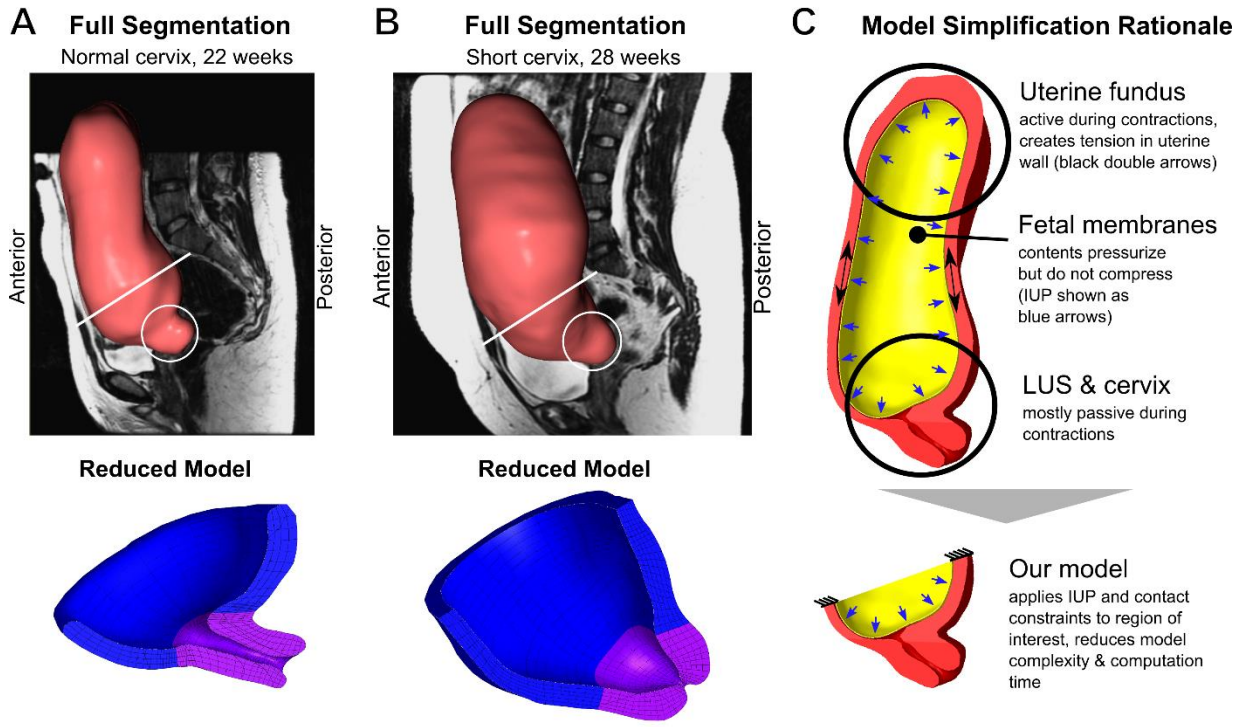

Figure 3: 3D geometry of (A) normal and (B) short cervix pregnancy at 22 and 28 weeks, respectively. Circles indicate the location of the cervix. (C) Translation from whole uterine geometry to partial model of LUS and cervix.

2.4 Volume Meshes

For computational efficiency, we developed a partial model to focus on the interaction between the amniotic sac, LUS, and the cervix. See **Boundary Conditions and** Loads on page 19 and Figure 3(C) for details on how the partial model accounts for uterine loading. Surface meshes for the LUS and cervix were

imported into IA-FEMesh[1] for the creation of the volumetric finite element meshes. Within the software, we positioned structural guiding blocks (Figure 4(B)) around the surface mesh previously created. We then seeded the boundaries of these blocks to specify the mesh density for the model. Near the cervical canal, we increased the mesh density to improve model accuracy and resolution of the results.

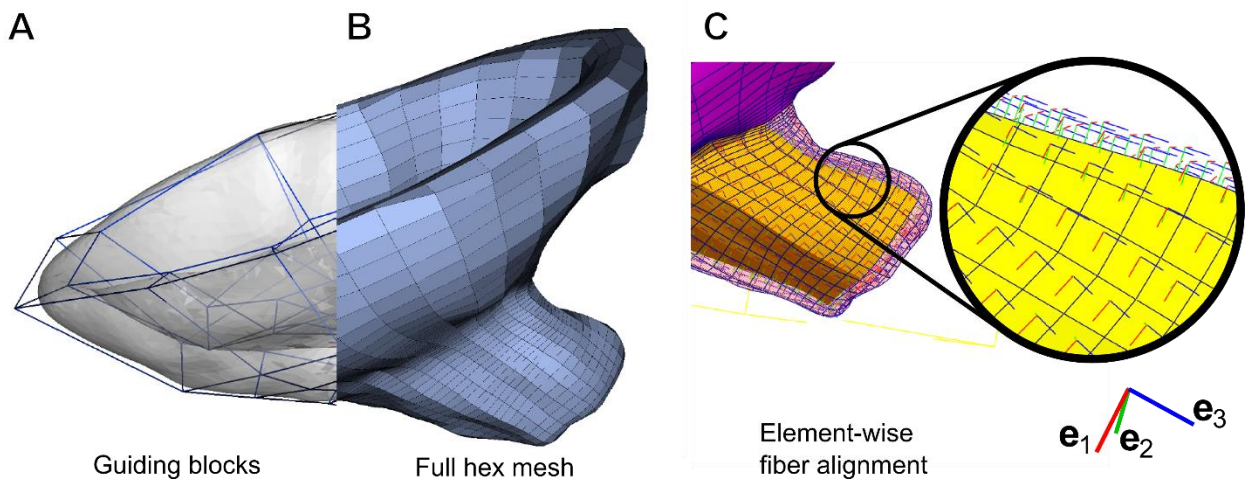

Figure 4: IA-FEMesh bounding box meshing strategy. (A) Surface mesh shown in translucent gray with guiding blocks for IA-FEMesh shown as a blue framework of polyhedra. (B) Resulting hexahedral mesh of the LUS and cervix. (C) Local fiber coordinates were prescribed in each hexahedral element. Each local $\boldsymbol{e_i}$ points circumferentially around the inner cervical canal.

To create a volume mesh for the amniotic sac, a mask representing the interior of the uterus was generated. A surface mesh was fitted to that volume, then extruded inward 0.5 mm to form a thin volumetric mesh representing the amniotic sac. We chose 0.5 mm thickness because it is representative of reported literature values for amniotic sac thickness [39], [44], [45]. Figure 4 shows the completed meshes, with mesh statistics given in Table 2.

Table 2: Mesh properties for MRI-based models.

	Long Model Uterus + Cervix	Long Model Amniotic Sac	Short Model Uterus + Cervix	Short Model Amniotic Sac
Element Type	Hexahedra	Hexahedra	Hexahedra	Hexahedra
Element Count	5332	2450	2652	2180

[1] Version 1.0. http://www.ccad.uiowa.edu/MIMX/Projects/IA-FEMesh.

Min, Max, Mean Volume (mm^3)	1.0, 216.5, 17.5	1.9, 14.4, 3.6	0.23, 331, 31.9	0.03, 5.3, 25.4
Min, Max, Mean Jacobian	0.06, 144, 14.6	0.7, 12.9, 3.3	0.002, 36.7, 3.6	0.003, 3.0, 0.62

2.5 Building the Finite Element Model

Model assembly and model calculations were done with the FEBio[2] finite element package. Volume meshes were imported and assembled within FEBio's PreView program [27]. For both the long and short cervix models, we defined the cervix as the region of tissue from the external os to the internal *os* and partitioned these elements separately from the rest of the LUS. In the short cervix model, we observed the "neck" of the funneling cervix and took it to be the histological internal *os* (Figure 3).

Models were built to investigate the effect of three different factors on the mechanical stress state of the cervix: 1) geometry of the anatomy, 2) cervical material model, and 3) amniotic sac mechanical properties including adhesion to the uterine wall. To investigate geometric considerations, the cervical stress state of the long and short cervix models are compared using the same cervical material model and model parameters. To investigate different forms of the cervix material model (models described in Section 2.7) and the effect of amniotic sac properties (properties described in Section 2.8), the long cervix model was used as a platform for comparison.

Table 3: Mesh properties.

	Normal LUS + Cervix	Normal Membrane	Short LUS+Cervix	Short Membrane
Hexahedral elements	5332	2450	2652	2180
Min, max, mean volume (mm^3)	1.0, 216, 17	1.9, 14.4, 3.6	0.23, 331, 32	0.03, 5.3, 32
Min, max, mean Jacobian	0.06, 144, 15	0.7. 13, 3.3	0.002, 37, 3.6	0.003, 3.0, 0.62

[2] Version 2.1.0. http://www.febio.org.

Table 4: Material models and properties used in the LUS, amniotic sac, and cervix, for MRI-based geometric models.

Location, Material Type	Properties
LUS, random continuous fiber distribution	E = 0.006 MPa, ν = 0.3; β = 3; ξ = 0.1 MPa
Amniotic sac, neo-Hookean	E = 20 MPa, ν = 0.3
Cervix, neo-Hookean tensile	E = 0.97 MPa, ν = 0.3
Cervix, neo-Hookean compressive	E = 0.004 MPa, ν = 0.3
Cervix, single fiber family (power law)	E = 0.003 MPa, ν = 0.37; β = 3; ξ = 0.137 MPa
Cervix, random continuous fiber distribution	E = 0.001 MPa, ν = 0.4; βi = 3; ξi = 0.018 MPa
Cervix, ellipsoidal fiber distribution	E = 0.001 MPa, ν = 0.4; βi = 3; ξ1 = 0.03 Mpa, ξ2,3 = 0.015 MPa

Note: For material fits to experimental data, see Figure 6 and [26]. Material properties are defined as in the FEBio 2.0 software. For fiber stiffness parameters ξ_i, subscripts indicate correspondence to a local basis direction in each element. In this study, direction e_1 indicates a basis vector aligned circumferentially around the cervical canal. The EFD model is rotationally symmetric around this preferential direction. For the SFD model, the same property is specified for every orthogonal direction. Subscript NH refers to a neo-Hookean material model.

2.6 Boundary Conditions and Loads

The position of the cervix in the abdomen is passively maintained by the pubovesical ligaments in the anterior-posterior direction and the cardinal ligaments in the lateral direction. These ligaments act as a "sling" supporting the organ but not exerting large forces on it. During labor, the upper portion of the uterus contracts, resulting in increased IUP which must be balanced by stress in the cervix and LUS. In contrast to the uterine fundus, the LUS and cervix are primarily mechanically passive during labor [46]. The IUP during uterine contraction and pushing is three to four times greater than the IUP of passive loading conditions [43].

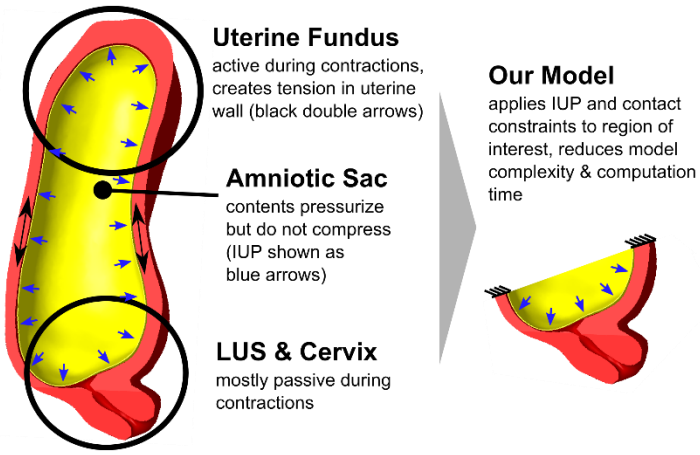

Figure 5: Conversion from whole uterine geometry to partial model of LUS and cervix in MRI-based models.

In this study, we replicate the dominant loading forces in the LUS and neglect passive interactions with ligaments, though ligament effects may be included in subsequent models. In this model, the top edge of the LUS is fixed in 3D space while the remaining portion is free to deform. A similar fixed boundary condition also holds the top edge of the amniotic sac section in place. To investigate the response of the model under varied biologically relevant loading conditions, the interior side of the amniotic sac is subjected to a prescribed pressure that sweeps the range of 0-20,kPa, covering the IUP ranges of pregnancy and delivery. Three IUP levels found in the literature are of note, corresponding to the baseline tone (3 kPa), the maximum pressure during contraction (8.6 kPa), and the maximum pressure during pushing (12.8 kPa) [43]. Generally, we have presented stress and strain maps at the 8.6 kPa level to represent a contraction.

2.7 Material Models

We investigate five material modeling scenarios for the cervix, focusing on models of varying complexity for the cervix based on previous experimental data. In this initial investigation, we ignore the transient effects caused by the viscoelasticity and poroelasticity of the tissue. The first model is an isotropic neo-Hookean material model, where the Young's modulus E_{NH} and Poisson's ratio ν_{NH} are adjusted to capture the equilibrium tensile behavior. The second model is also of the ordinary neo-Hookean type, but

employs the compressive modulus and Poisson's ratio, the first of which is much lower in compression than in tension. The third through fifth models are fiber composite models designed to capture the tension/compression nonlinearity and anisotropy of the tissue. The third model treats the collagen fibers as a single fiber family circling around the inner canal with no dispersion. The fourth model treats the collagen fibers as a randomly distributed continuous fiber network, where fibers are evenly distributed around a unit sphere and fibers reorient and stretch in the direction of principal tensile stresses. Somewhat combining the ideas of the previous two models, the fifth model features a continuous but weighted direction-dependent ellipsoidal fiber distribution, with high-stiffness directions circling around the cervical canal. For all three of these fiber composite models, the collagen is phenomenologically prescribed as a nonlinear power law, with material parameters ξ as the fiber stiffness measured in kPa and β as the power (set to 3 for all MRI-based simulations). In all of these fiber composite models, the fibers are embedded in a compressible isotropic neo-Hookean ground substance, with Young's modulus E_{GS} and Poisson's ratio ν_{GS}.

All cervical material properties are determined by material model fits to previously published uniaxial tension and compression equilibrium data of human cervical tissue [1], [32], [33]. Material properties for the amniotic sac and LUS were estimated from literature values [39], [40]. Material parameters for five different material models are in Table 4 and all models were implemented within FEBio [47]–[49].

2.7.1 Neo-Hookean material model

The simplest kind of material model used in our study was a hyperelastic NH model containing no fibers. It is an isotropic material, similarly stiff in tension and compression. The strain energy per unit reference volume for a NH material is given by

$$\Psi^{\mathrm{NH}} = \frac{\mu}{2}(I_1 - 3) - \mu \ln J + \frac{\lambda}{2}(\ln J)^2. \quad (1)$$

In the expression above, μ and λ are the Lamé constants from linear elasticity, and $J = \det \mathbf{F}$ is the Jacobian where $\mathbf{F}$ is the deformation gradient (Holzapfel 2000). Young's modulus and Poisson's ratio are related to the Lamé constants by $E^{NH} = \mu(3 + 2\mu/\lambda)/(1 + \mu/\lambda)$ and $\nu^{NH} = 1/[2(1 + \mu\lambda)]$, respectively. We investigated two NH models for cervical material behavior, one fitted to compression data and the other fitted to tensile data. The two NH models served as points of comparison by approximating the possible extremes of nonpregnant tissue response.

2.7.2 Fiber composite material models

Fiber composite models have been described by several authors (Lanir 1983; Holzapfel 2000; Ateshian 2007, 2009), and applied specifically to describe human cervical tissue material behavior by our group (Myers et al. 2015). For more information on the models in this section, one may consult those works as well as the FEBio documentation (Maas et al. 2012).

To explore the effects of modeling different fiber distributions, we chose three model configurations: no fiber dispersion (NFD), preferentially aligned ellipsoidal fiber distribution (EFD), and a random or spherical fiber distribution (SFD). Each model was independently fitted to experimental data from tension and compression tests on human nonpregnant cervical tissue. The curve fits are shown in Figure 3. Tension–compression nonlinearity in fiber composite material models occurs because the fibers only sustain tension while a NH ground substance is used to provide the required compressive support. Fibers were modeled in each case to undergo affine deformation with the ground substance. The total strain energy for each fiber composite material in this study is the sum of the strain energy density of a NH ground substance Ψ_{Ground}^{NH} and that of a particular fiber configuration Ψ_{Fibers}:

$$\Psi_{\text{Total}} = \Psi_{Ground}^{NH} + \Psi_{Fibers}. \tag{2}$$

The Cauchy stress tensor is then

$$\sigma_{\text{Total}} = \frac{1}{J}\frac{\partial \Psi_{Total}(\mathbf{F})}{\partial \mathbf{F}}\mathbf{F}^{\text{T}}. \tag{3}$$

The simplest fiber composite model we utilized has fibers directed along only the local $\boldsymbol{e}_1$ direction of each element in the reference configuration. Organ-level fiber directionality was achieved by using a custom python script to prescribe the orientation of a local basis $\{\boldsymbol{e}_i\}$ in each element with respect to the global coordinate system according to manually defined anatomical landmarks and the orientation of the hexahedral element faces within the model. The resulting model featured a local $\boldsymbol{e}_1$ axis (and therefore fibers) in each element, circumferentially oriented around the cervical canal (Figure 4(C)). The fiber strain energy density for this NFD model – called the Fiber with Exponential Power Law model in FEBio – has the form

$$\Psi_{Fibers}^{NFD} = \mathrm{H}(I_n - 1) \cdot \frac{\xi^{NFD}}{\beta^{NFD}} \cdot (I_n - 1)^{\beta^{NFD}}. \tag{4}$$

The Cauchy stress tensor is then

$$\sigma_{\mathrm{Total}} = \frac{1}{J} \frac{\partial \Psi_{Fibers}^{\mathrm{NFD}}(\mathbf{F})}{\partial \mathbf{F}} \mathbf{F}^{\mathrm{T}} \tag{5}$$

$$= \frac{2I_n}{J} \frac{\partial \Psi_{Fibers}^{\mathrm{NFD}}}{\partial \mathrm{I_n}} \mathbf{n} \otimes \mathbf{n}, \tag{6}$$

where $\mathbf{n} = \mathbf{F} \cdot \mathbf{n}^r / \sqrt{I_n}$ is the current fiber direction, given an initial direction $\mathbf{n}^r$ (equal to $\boldsymbol{e}_1$ in this model), and $I_n = \mathbf{n}^r \cdot \mathbf{F}^{\mathrm{T}}\mathbf{F} \cdot \mathbf{n}^r$ is the square of the fiber stretch. In this model, $\xi^{NFD} > 0$ is the fiber "modulus" with units of stress, $\beta^{NFD} \geq 2$ is a unitless stiffening parameter, and $H(\cdot)$ is a unit step function that is zero-valued for negative arguments and unity-valued for positive arguments.

While a fiber model with no dispersion is highly appropriate in some circumstances (for example, when modeling ligaments), it may not be the closest reflection of collagen fiber alignment in the cervix, which is more dispersed (Aspden, 1988; Gan et al. 2015). For that reason, we fitted two distinct distributed fiber composite models to tension–compression data from nonpregnant human tissue. The first model assumed an ellipsoidal distribution of fiber stiffness as a function of spherical angles θ and ϕ, while the

second model prescribed a random (or spherical) distribution. The strain energy density for EFD or SFD is given by the integral

$$\Psi_{Fibers}^{NFD} = \int_0^{2\pi}\int_0^{\pi} \mathrm{H}(I_n - 1)\cdot \Psi_n^{EFD}(I_n, \mathbf{n}^{\mathrm{r}}) \sin\phi \, d\phi d\theta. \tag{7}$$

where H and I_n are as previously defined. The fiber strain energy $\psi_n^{EFD}(I_n, \mathbf{n}^{\mathrm{r}})$ in this material is governed by the power law defined in FEBio in the form

$$\Psi_n^{EFD}(I_n, \mathbf{n}^{\mathrm{r}}) = \xi^{EFD}(\mathbf{n}^{\mathrm{r}})(I_n - 1)\beta^{EFD}, \tag{8}$$

where $\xi^{EFD}(\mathbf{n}^{\mathrm{r}})$ is the fiber stiffness distribution function. For this morel, it is written in the form of the ellipsoid

$$\xi^{EFD}(\mathbf{n}^{r}) = \left(\frac{\cos^2\theta \sin^2\phi}{\xi_1^2} + \frac{\sin^2\theta \sin^2\phi}{\xi_2^2} + \frac{\cos^2\phi}{\xi_3^2}\right)^{-1/2}, \tag{9}$$

where ξ_1 and $\xi_{2,3}$ are the lengths of the semi-major axis (in the local $\boldsymbol{e}_1$ direction) and both semi-minor axes ($\mathbf{e}_2$ and $\mathbf{e}_3$), respectfully, of the ellipsoid defining the fiber distribution. The unit vector $\mathbf{n}^r$ points in the direction of fibers passing through dA and is given in terms of the spherical coordinates θ and ϕ by $\mathbf{n}^{\mathrm{r}} = \sin\phi\cos\theta\,\mathbf{e}_1 + \sin\phi\sin\theta\,\mathbf{e}_2 + \cos\phi\,\mathbf{e}_3$. The Cauchy stress tensor for EFT fibers is given by

$$\sigma_{Fibers}^{EFD} = \frac{1}{J}\frac{\partial \Psi_{Fibers}^{\mathrm{EFD}}(\mathbf{F})}{\partial \mathbf{F}}\mathbf{F}^{\mathrm{T}} \tag{10}$$

$$= \frac{2}{J}\int_0^{2\pi}\int_0^{\pi} \mathrm{H}(I_n - 1)\cdot I_n \frac{\partial \psi_n^{EFD}(\mathbf{F})}{\partial \mathbf{F}}\mathbf{n}\otimes\mathbf{n}\sin\phi\, d\phi d\theta. \tag{11}$$

where $\beta^{EFD} \geq 2$ is the fiber stiffening parameter taken as a constant, $I_n = \mathbf{n}^r \cdot \mathbf{F}^{\mathrm{T}}\mathbf{F}\cdot\mathbf{n}^{\mathrm{r}}$ is the fiber stretch squared and $\mathbf{n} = \mathbf{F}\cdot\mathbf{n}^r/\sqrt{I_n}$ is the current direction of the fibers that were directed along $\mathbf{n}^{\mathrm{r}}$ in the reference configuration.

Implicit in our ellipsoidal model was the assumption of an equal fiber dispersion in all directions perpendicular to the semi-major fiber axis e1 (equivalent to setting $\xi_2 = \xi_3$). The ratio of ξ_1 to ξ_2 for our EFT model was fitted to X-ray diffraction fiber orientation density data of cervical stroma from (Aspden 1988). Note that the SFD is simply the spherically symmetric case of an EFD, and was achieved by setting $\xi_1 = \xi_2 = \xi_3$ in the relations above.

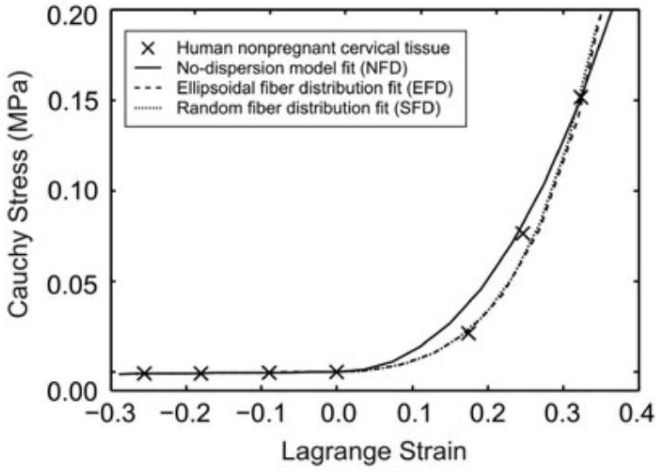

Figure 6: Curve fits for three fiber composite models to tension and compression data from experiments on nonpregnant human cervical tissue specimens done by our group [1], [26], [32]. The fits were done using a combination of manual iteration and least-squares regression. The final material property values are listed in Table 4.

2.8 Fetal Membrane and Contact

Two different contact scenarios were used for this study. With the exception of the adhesion comparison, all simulations were carried out using FEBio's "tied" contact interface, which constrains two adjacent surfaces to deform and translate together without sliding relative to each other. This type of contact represents a healthy pregnancy in which the amniotic sac is still attached to the decidua parietalis. In contrast, a "facet-to-facet" sliding contact interface was used to represent the interaction between detached

amniotic sac and the decidua. In both cases, an augmented Lagrangian method was used to enforce the contact interface.

We chose a nominal value for amniotic sac modulus of 20MPa for the simulations presented in this paper. This value is in the range of literature values for stiffness of amnion under high strain [39], [40]. To determine how large an effect the amniotic sac stiffness has on results, we varied this parameter and plotted the resulting strains in a representative element from the cervix in Figure 7.

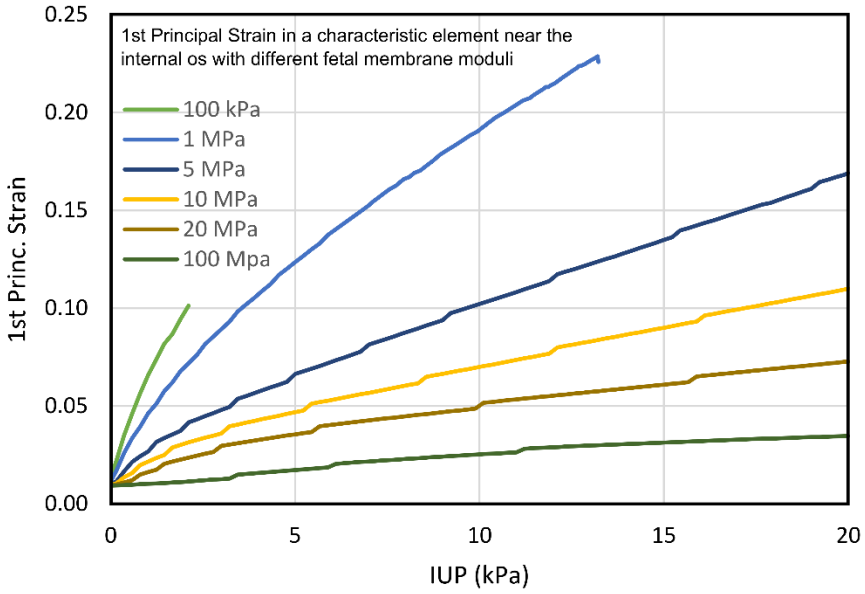

Figure 7: Illustration of how membrane modulus affects the resulting strain levels in the internal *os* of the cervix. Literature values for amniotic sac stiffness vary between 1 and 40 MPa.

2.9 Simulation Steps

Each simulation is done in two time steps. The first step is an initialization process to ensure good surface alignment between the uterus and amniotic sac volume meshes. This step applies no load to the model but gradually increases the contact penalty from 0 to 100% of its value (scaling the Lagrange multiplier increment). The second step in the simulation linearly increases the IUP applied to the interior of the amniotic sac from 0 kPa to 20 kPa in a minimum of 100 steps.

2.10 Results

The simulations were carried out in FEBio 2.1 on a Windows 7 PC with an Intel Core i7 processor and 32 GB of RAM. The exact convergence times varied between 10-60 minutes, depending on material model and material properties. All models show increasing first principal strain levels as IUP increases.

2.10.1 Long and Short Cervix Models

Principal stresses for the long and short cervix models are given in Figure 8. Stresses are universally lower in the cervix where the material is more compliant. Stress concentrations are observed at the interface between cervix and LUS for both long and short cervix models. The principal strains and their directions for our two models are plotted in Figure 9 for a randomly distributed continuous fiber material in the cervix. In the short cervix model, there are higher strains located within the middle cervix, whereas the long cervix model features strain concentrations mainly in the LUS and top of the cervix.

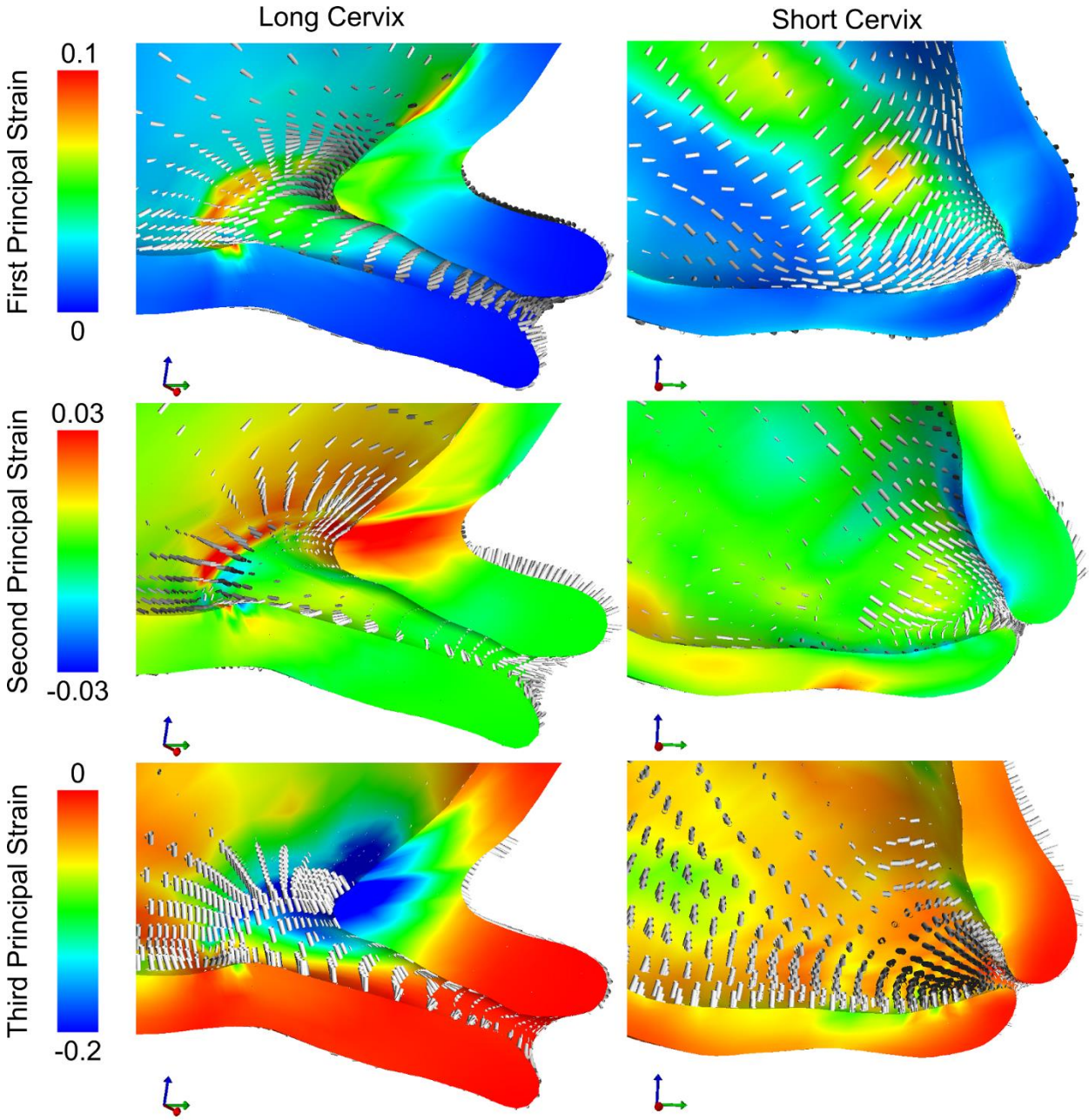

Figure 8: Stress results for the long and short cervix model using a random continous distributed fiber model in the cervix, with an IUP of 8.6 kPa corresponding to the peak IUP during uterine contraction.

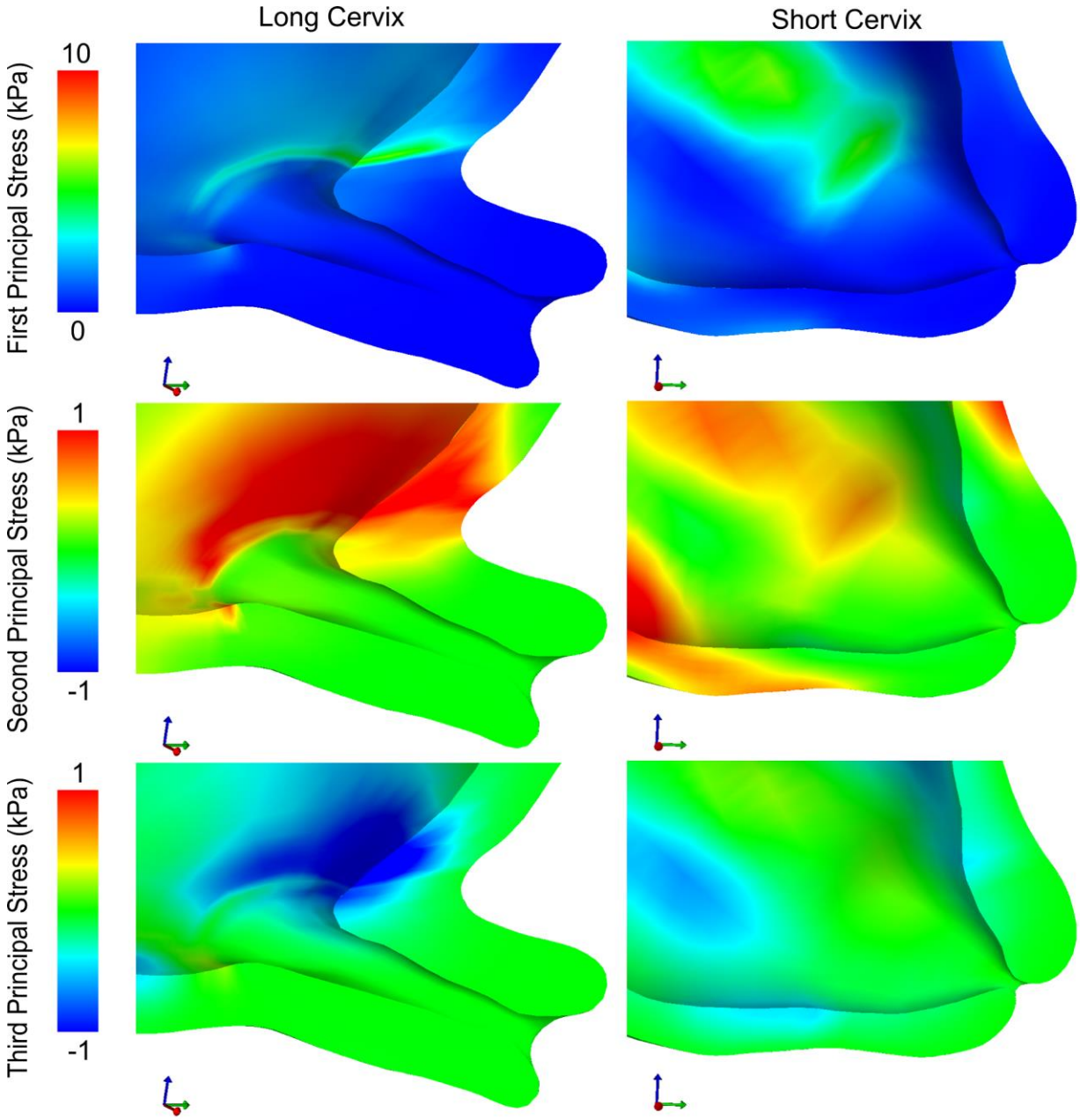

Figure 9: Strain results for the long and short cervix model using a random continuous distributed fiber model in the cervix, with an IUP of 8.6 kPa corresponding to the peak IUP during uterine contraction.

2.10.2 Changing Cervical Material Model

The principal stresses for five cervical material model choices are given in Figure 10. The neo-Hookean materials produce larger stress concentrations than the three fiber-based material choices. Stresses

on the inside of the LUS wall tend to be higher than the stresses on the outside, with the exception of the external posterior part of the cervix where it connects to the LUS. In this location, high stress is observed for the tensile neo-Hookean material choice (top left frame of Figure 10). All models display higher stresses in the LUS near the interface between the LUS and cervix. This is to be expected due to the step change in material properties at the interface. Future models will feature a more gradual property change, but it should be noted that the precise location of this division can only be known through histology.

As shown in Figure 10 and Figure 11, the tensile neo-Hookean cervical model predicts the highest stress and least strain of the models. A ring of higher compressive strain on the order of 0.1 is observed in the uterine wall just outside the cervical boundary. The single fiber family model shows concentrated tensile strains greater than 0.2 around the internal *os*, and large regions of tensile strain on the order of 0.2 within the cervix. The randomly distributed continuous fiber model and the ellipsoidal fiber model show the most uniform strain distributions of all the models, with first principal strains at levels under 0.15 throughout.

The most prominent feature for all of the first principal strain maps is the circumferential strain pattern around the internal *os*. This feature is most consistent within models using the tensile neo-Hookean, the random continuous fiber model, and the ellipsoidal fiber distribution model. Secondly, each model showed tensile strains oriented radially outward from the cervix and pointing tangent to the wall of the LUS. There are visible strain concentrations at and surrounding the location of the internal *os*. Finally, strain in the long cervix model decreases rapidly moving away from the internal *os*, whereas strain in the short cervix model is large through most of the cervix.

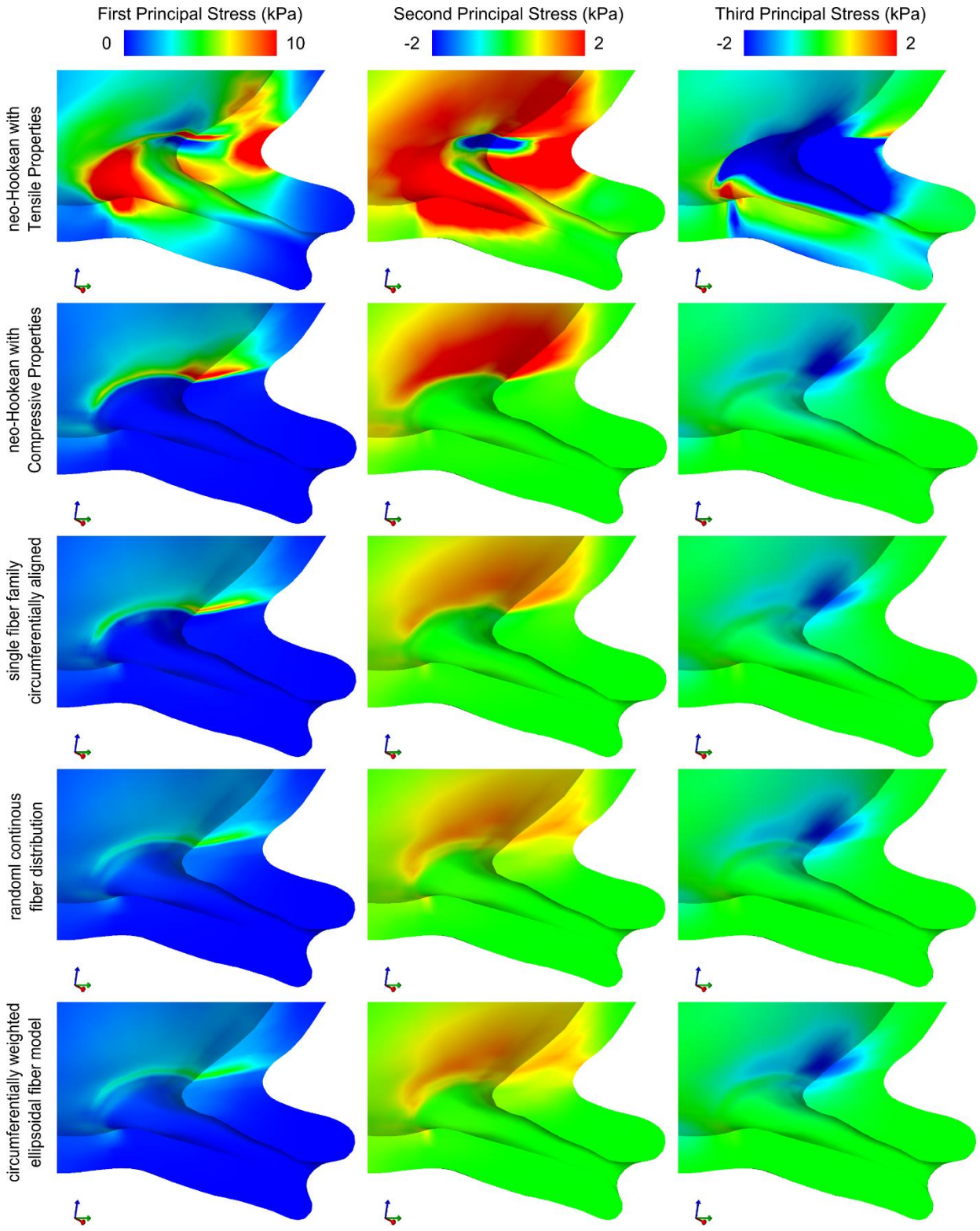

Figure 10: Principal stresses at IUP=8.6 kPa for five different cervical material models.

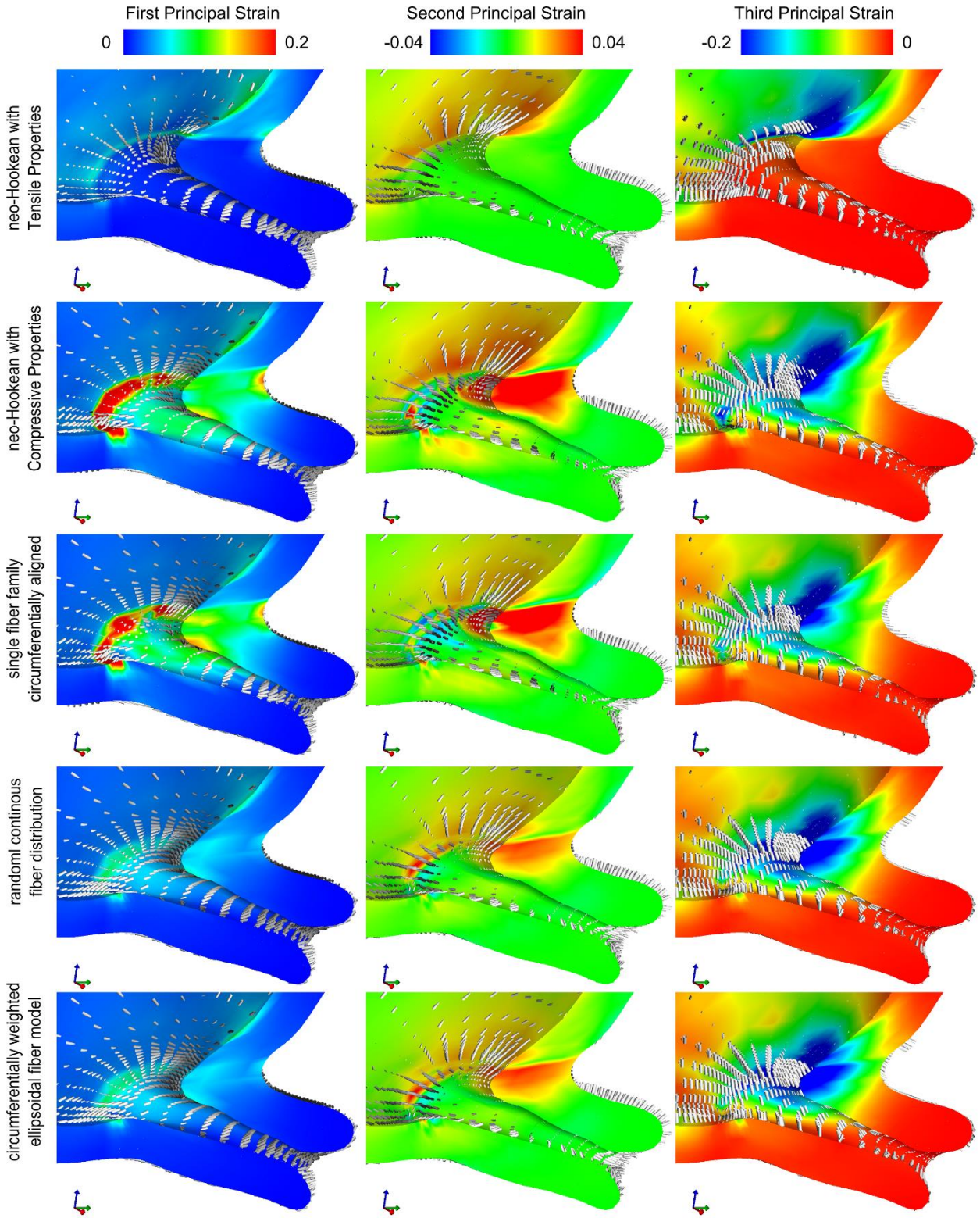

Figure 11: Principal strains and their directions at IUP=8.6 kPa for five different cervical material models.

2.10.3 Effect of Amniotic Sac Adhesion

A variable degree of load sharing occurs between the amniotic sac and the LUS when the amniotic sac is fully adhered to adjacent LUS surfaces. Adhesion reduces the degree of circumferential cervical dilation due to the IUP, and also slightly increases strain levels near the surface of the surrounding LUS, as seen in Figure 13. With membrane adhesion, strain inside the amniotic sac layer is greater over the cervical canal but less over areas in direct contact with the uterine wall. Figure 14 shows an example of how strain varies with and without adhesion for an element near the internal *os*.

2.11 Discussion

In this work, we detail a method to generate an anatomically accurate finite element model of the pregnant pelvis derived from MRI data. We explore the effects of geometry, cervical material properties, membrane properties, and membrane contact assumptions on the stress and strain generated in the cervix for two patients in their second trimester of pregnancy.

The results illustrate that asymmetries of the uterus and cervix impact the magnitude and direction of stress and strain in the cervix. We also demonstrate that cervical material characteristics, particularly the collagen ultrastructure and tissue stiffness parameters, contribute significantly to the level of dilation in the cervix. Lastly, we have demonstrated that the fetal membrane contributes to the load-bearing of the uterine contents during pregnancy, where a fully-adhered fetal membrane results in lower mechanical loading in the cervix than in the case of a membrane which is free to slide in its contact with the decidua.

2.11.1 Anatomical Geometry

Our patient-specific models show a stress concentration at the level of the internal *os* of the cervix, matching findings from previous CAD-based models [11], [37]. In the results presented here, this stress and strain concentration is not centered on the cervical opening but is instead offset due to the asymmetry of the cervical canal and the uterus. Therefore, regions of high stress will vary between patients and may vary between pregnancies. Interrogating an element at the posterior and at the anterior internal *os* (Figure 12) we find that both locations have a first principal strain in tension oriented circumferentially around the cervical canal (see Figure 12, anterior and posterior directions 1).

The posterior element is subjected to more compression along the axis of the cervical canal (Figure 12, posterior direction 3) because of the acute angle between the cervix and the posterior part of the LUS wall. The anterior element experiences compression from the fetal membrane but it occurs in the radial

direction from the canal to the exterior surface of the cervix (see anterior direction 3). This example illustrates how it is possible for non-obvious strain effects to arise from irregular or asymmetric geometry.

2.11.2 Cervical Material Properties

Based on *ex-vivo* mechanical tests of human tissue specimens we know that the material behavior of the tissue is nonlinear, anisotropic, and time-dependent. It is currently unknown how each of these tissue material behavior complexities plays a role in keeping the cervix shut during pregnancy. By comparing results from the different model choices, we highlight the large difference in the cervical stress and strain for two neo-Hookean models, one based on tension data and the other on compression data, and three fiber composite models (Figures Figure 10 and Figure 11). Our findings suggest that by incorporating cervical collagen directionality and dispersion we gain additional mechanical insight into the role of the collagen ultrastructure in maintaining the fetus.

In our results, we find that it is key to account for the distributed nature of the collagen fiber network. A cervical material model with a single fiber family with no dispersion creates high stress and strain concentrations in directions perpendicular to the fiber. Collagen dispersion creates tensile load carrying capability in multiple directions, as illustrated by the results for both continuous fiber models. The randomly oriented and ellipsoidal fiber models predict remarkably similar outcomes, with the addition of the preferred directionality not resulting in significantly lower strains. Further studies with additional material property and collagen ultrastructure measurements based on pregnant tissue samples need to be conducted to understand the exact role of the cervical collagen stiffness and dispersion during pregnancy.

2.11.3 Adhesion between the Chorion and Decidua

In a normal pregnancy, the fetal membrane is firmly adhered to the lower uterus and cervix with the aid of the fetal fibronectin protein [50]. However, in some cases of cervical shortening, lack of adhesion can be seen on vaginal sonography. To investigate how the adhesion of the fetal membrane to the uterus

affects the stress and strain inside the cervix, we equipped our model with two distinct contact conditions: first, a no-slip tied contact interface, representing complete adhesion; and second, a frictionless sliding interface representing detached fetal membrane. Our model demonstrates that load sharing can occur between the fetal membrane and cervix in the case of the model with adhesion. Peak and average stress and strain levels were approximately 60% lower with adhesion acting between the membrane and uterus (Figure 13). These results demonstrate that the interaction between the cervix and membrane could play an important role in cervical shortening, and also that membrane adhesion is a key consideration when building finite element models of pregnancy.

Membrane material model choice and parameters related to membrane stiffness are also important factors to consider because a stiffer membrane will result in lower cervical deformation (Figure 7). In the future, our simulations will incorporate material models based on new experimental data from mechanical testing of amnion [51], which will better replicate the macroscopic mechanical response of the complex membrane microstructure [52].

All of our models show a stress concentration over the internal *os* which propagates to some extent into the cervix. This stress and strain concentration is not centered on the cervical opening but is instead offset likely due to the asymmetry of the cervical canal.

2.11.4 Manifestation of Geometric Asymmetry

Figure 12 illustrates the three principal strain directions at two representative locations in the long cervix model around the internal *os*. Both locations have a first principal strain in tension oriented circumferentially around the cervical canal (see anterior and posterior directions 1). The posterior element is subjected to more compression along the axis of the cervical canal (posterior direction 3) because of the acute angle between the cervix and the posterior part of the LUS wall. The anterior element experiences compression from the amniotic sac but it occurs in the radial direction from the canal to the exterior surface

of the cervix (see anterior direction 3). This example illustrates how non-obvious strain effects can arise from asymmetrical geometry.

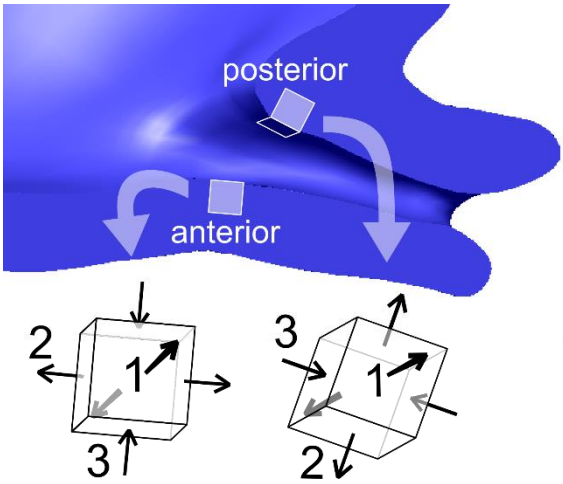

Figure 12: Principal strain directions in two representative locations, one anterior and one posterior to the internal *os*.

2.11.5 Differences Between Cervical Material Models

We utilized two neo-Hookean models based separately on tension and compression data in order to illustrate the large nonlinearity of cervical tissue. These, the top two material models in Figure 10, predict radically different stress patterns even though they use mechanical properties from the same kind of tissue. We suggest the use of a fiber composite model for a more realistic response from a finite element model because the cervix is known to contain distributed fibers [53]. Our random and preferentially aligned fiber models predict remarkably similar strain results (within 1% of each other), but the two models with continuous fiber distributions show less a stress concentration at the LUS interface than the single fiber family model. Anisotropic material models allow for greater fidelity in reproducing the complex mechanical response of soft tissues like the cervix. However, the process of assigning location-specific directionality is nontrivial even in a simple geometry like the cervix, so a random continuous distribution is satisfactory for our purposes.

2.11.6 Effect of Membrane Adhesion

Clinically, altered levels of fetal fibronectin protein in the vaginal fluid is associated with an increased risk of PTB [54]. We hypothesize that the mechanism of this relationship may be increased mechanical loading on the cervix due to a loss of adhesion between the fetal membranes and the inner uterine wall. Such a loss of adhesion, if it causes early cervical tissue remodeling, could potentially lead to preterm effacement and funneling of the fetal membranes into the cervix.

The "membrane sweep" is a technique intended to induce labor in post-term pregnancies. In the procedure, the amniotic sac is manually detached from the decidua parietalis in the area surrounding the internal *os*. This is associated with an increase of prostaglandins and increased contractions.

Previous computational simulations of the mechanical loads at play during pregnancy by our group [22], [55] have shown that adhesion of the fetal membrane to the decidua (representing the function of fetal fibronectin) drastically reduces the baseline mechanical stress (force per cross-sectional area) inside the cervix during pregnancy.

Our model demonstrates that load sharing can occur between the amniotic sac and cervix in the case of the model with adhesion. Peak and average stress and strain levels were approximately 60% lower with adhesion acting between the amniotic sac and uterus (Figure 13). The first principal strain for one element under these two different conditions if given in Figure 14. These results demonstrate how mechanical loading in the cervix and LUS could be part of a bio-mechano-chemical process that expedites the onset of labor in patients who have had the procedure done.

Figure 13 shows the first principal strain in the cervix and LUS under the assumptions of an attached fetal membrane and a detached fetal membrane with no friction. In both cases, the IUP was set to the level experienced in a uterine contraction during labor. The results demonstrate how the detachment of the amniotic sac before delivery increases the mechanical load on the cervix, inducing deformation.

Simulations use the random continuous fiber model for the cervix, with IUP=8.6 kPa (peak contraction value).

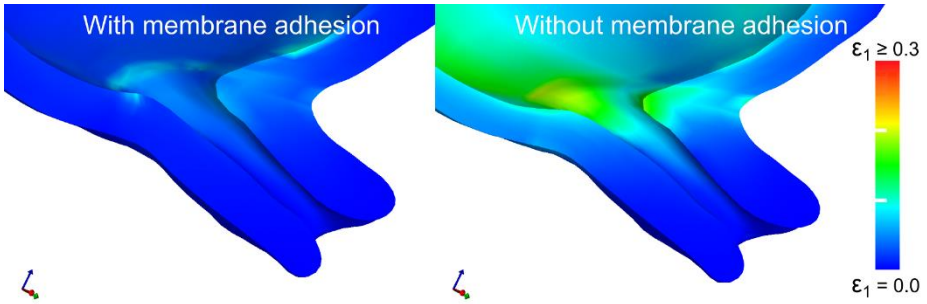

Figure 13: First principal strain with and without membrane adhesion.

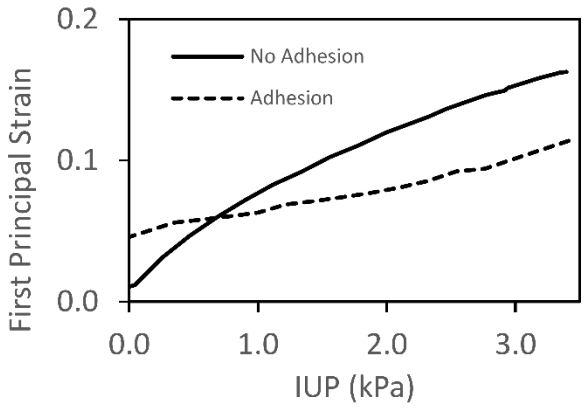

Figure 14: Typical differences in first principal strain, with and without membrane adhesion, for an element in the region of the internal *os*. Some initial strain is expected in the adhesion case due to the small space between the membrane mesh and the uterine mesh near the internal *os*.

2.11.7 Limitations

We made several assumptions for the purposes of this model which may influence the results. It is noted that *in-vivo* imaging of the abdomen produces geometry of an already loaded configuration. The reference configuration used to calculate stresses and strains is therefore technically incorrect, and the results presented in this paper should be viewed as an approximation or extrapolation. Additionally, the mechanical properties of cervical tissue have been characterized only in the nonpregnant and the full term

cervix. We have used the nonpregnant properties for these simulations because the scans were done before dramatic cervical softening is expected to occur.

Lastly, we have neglected any influence of the pubovesical and cardinal ligaments, which may have some effect on the loading state. Our model includes the LUS, cervix, and a portion of the amniotic sac. The components accounted for in the model should create a representative stress and strain configuration in the cervix under the loading conditions of interest, but it is not designed to accurately reproduce deformation far away from the cervix.

Mechanical loading patterns have long been known to be correlated with tissue microstructure in bone [56]. Mechano-regulated cell behavior exists in articular cartilage [57] and in artery [58] which, like the cervix, are tissues featuring a collagen-rich extracellular matrix. A mechanically mediated cervical remodeling process, if it exists, should not come as a surprise. It is therefore of interest to investigate the mechanical stress and strain state of the cervix, in order to investigate possible biomechanical pathways to cervical remodeling. It is our goal to generate a longitudinal series of finite element models of a woman with a history of PTB, following her through pregnancy to understand the evolution of the strain pattern during cervical failure.

2.12 Conclusion

With this work, we simulated the stress and strain in the LUS and cervix under physiological IUP levels in two anatomically precise finite element models. This work represents the first 3D finite element model of the mechanical loading state of the cervix at this high a level of anatomical fidelity. It also accounts the interaction between the uterus and cervix and the amniotic sac at physiological IUP levels. We believe that these organs and interactions are the dominant factors affecting the mechanical stress and strain state within the cervix, particularly near the internal *os*.

Our results from this study support the inclusion of a fiber composite material for the cervix. The difference between a fiber model with preferentially aligned, ellipsoidal fiber distribution and a random distribution was minimal, so it is probably not worth including such detail in these first models.

One important insight gained from this work was the recognition that the fetal membrane material, and in particular, its adhesion to the uterine wall, have a dramatic influence on loading in the cervix. In future studies, great care must be taken to guarantee the fetal membrane is being accurately represented by the model assumptions.

This MRI-based model is a good "gold standard" in terms of replicating the pregnant anatomic geometry, but due to the time required to create a model, as well as the accompanying efforts required to solve a model with increased complexity, it is currently an unfeasible approach for translating engineering capabilities into the clinical setting.

2.13 Related Manuscripts and Conference Proceedings

1. M. Fernandez, M. House, S. Jambawalikar, N. Zork, J. Vink, R. Wapner, K. Myers. Investigating the mechanical function of the cervix during pregnancy using finite element models derived from high-resolution 3D MRI. Computer methods in biomechanics and biomedical engineering. 2016 Mar 11;19(4):404-17.
2. M. Fernandez, A. Ehret, E. Mazza, M. House, J. Vink, R. Wapner, and K. Myers, "The effect of fetal membrane prestretch on cervical loading during pregnancy." *Proceedings of the 39th annual meeting of the American Society of Biomechanics*, 2015, pp. 4–5.
3. M. Fernandez, M. House, S. Jambawalikar, J. Vink, N. Zork, R. Wapner, and K. Myers, "Biomechanical simulations of pregnancy: the effect of collagen stiffness and membrane adhesion on cervical deformation and shortening," *Conference poster at the 62nd Annual Scientific Meeting of the*

Society of Reproductive Investigators, *San Francisco, CA*, March 24-28, 2015. Reprod Sci 22: 326A S-089 Supp 1, March 2015.

3 Parameterized Biomechanical Pregnancy Model Using Ultrasound

To replicate anatomic geometry to a high degree of fidelity is a very time consuming venture. We explored this above in our MRI-based study. In this section, however, we present a new model that uses simplifying anatomic assumptions to build a new pregnant pelvic anatomy automatically, such that it can match anatomic measurements acquired for a specific patient during a simple ultrasound scan.

3.1 Motivation

Previous studies have investigated the mechanical loading state of the cervix through finite element models with CAD-based [11] and 2D [59] geometry measured from medical images. House, et al. simulated cervical funneling using CAD-based geometry, and proved the utility of the finite element method as a tool to study the mechanical deformation of the cervix. The models in those studies and the MRI study in section 1.4 were all generated manually, one geometric entity at a time. Such a process requires knowledge and skill in CAD and takes too long (typically days) to be practical in a clinical setting.

To reduce the time required for a patient-specific biomechanical simulation of pregnancy and to, therefore, bring our engineering analysis techniques closer to translational implementation in the clinic, we developed a rapid approach to building models which is detailed in the following section.

3.2 Methods

3.2.1 Standardized Anatomic Measurements

To enable geometric flexibility in the model while allowing it to reflect the anatomy as closely as possible, we developed a set of characteristic length, thickness, distance, and angle measurements for the uterus and cervix. They were chosen after thoughtful discussion with our clinical collaborators and represent a balance between geometric specificity, flexibility, and the feasibility of measuring them quantitatively via clinical ultrasound.

All of the defined measurements (Figure 2) can be taken transabdominally or transperineally. Uterine diameters (UDs) can be measured with the extended view imaging feature of modern ultrasound scanners (the Voluson E8 was used in our study) which automatically registers adjacent ultrasound images as the probe is swept across the abdomen from the fundus to the pubic bone at a steady rate of 2 cm/s. With this sagittal view, we obtain measurements of uterus longitudinal diameter (UD1), anterior-posterior diameters (UD2+UD3), and the offset of the cervical internal *os* from the uterus longitudinal diameter (PCO). To measure the transverse uterine diameter (UD4) in an extended axial view, the transabdominal probe can be swept from left to right across the mid-abdomen and the uterus measured at its widest point (Figure 15B). Uterine wall thicknesses (UT1-5) are measured at multiple locations from the fundus to the lower uterine segment (LUS) with the transabdominal probe in a standard clinical resolution. (Fig. 1C & D), and are considered the echogenic signal from the serosa to the decidua. Cervical length (CL), diameter (CD1), canal width (CD2), angle with the anterior LUS (AUCA), and angle with the periosteum of the symphysis pubis (CA1) were assessed via transperineal scans (Fig. 1E & F).

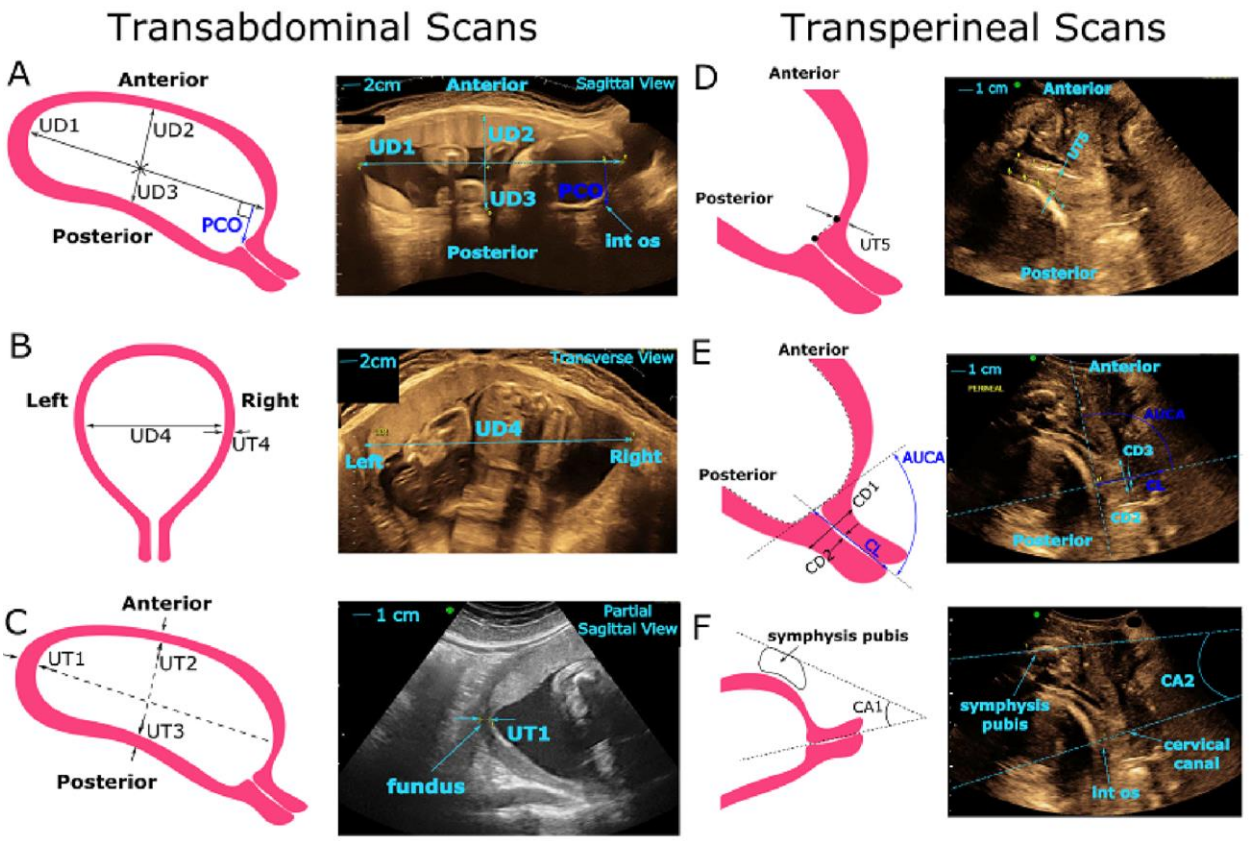

Figure 15: Ultrasound-measurable anatomic parameters. Parameters beginning with UT are uterine thickness measurements, UD are uterine distance measurements, CA are cervical angles, and CD are cervical distance measurements.

3.2.2 Modeling Strategy

In order to facilitate rapid, repeatable model creation, we wrote a custom scripted routine that operates within the Trelis (v 15.1, csimsoft LLC) finite element meshing software. Our routine uses the anatomical measurements described in section 3.2 as inputs and creates geometric primitives representing the uterus, cervix, membranes, abdomen, and vaginal canal. These geometries are subjected to Boolean addition and subtraction in such a manner as to generate the appropriate matching boundaries between organs. Within the scripted routine, geometric entities are named and tracked after being generated, or identified dynamically by position, so that they can be modified in a later step within the routine.

In addition, we developed a software tool dubbed “inp2feb” to translate ABAQUS-formatted .inp files into the FEBio finite element model input format. The tool is agnostic to what is being modeled and allows for unprecedented speed in developing mechanical FE models through the Trelis → FEBio pipeline. In addition to saving time in model generation, automation of this procedure reduces the frequency of human error in the model creation process. An image of the graphical interface of inp2feb is given below, in Figure 16.

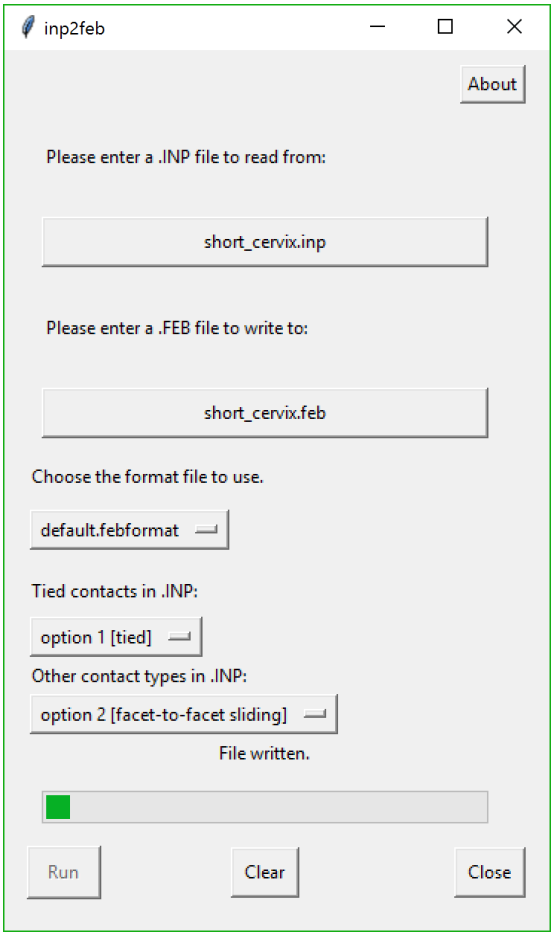

Figure 16: Graphical user interface for inp2feb.

A more detailed description of inp2feb and how to use it is given in section A.1 in the Appendix.

3.2.3 Components of the Model

3.2.3.1 Uterus

The uterus is represented by ellipsoidal geometry (Figure 17) for simplicity. Two ellipsoidal shells are transformed with scaling, translation, and rotation operations such that the inner uterine dimensions are correct and the space between the shells matches the uterine wall thicknesses given as input. These shells are subsequently filled, then one is subtracted from the other, to generate a solid uterine wall. In this initial version of the model, UT5-UT9 are averaged to reduce measurement uncertainty. In future models, these values may be used to generate a more detailed lower uterine segment thickness profile.

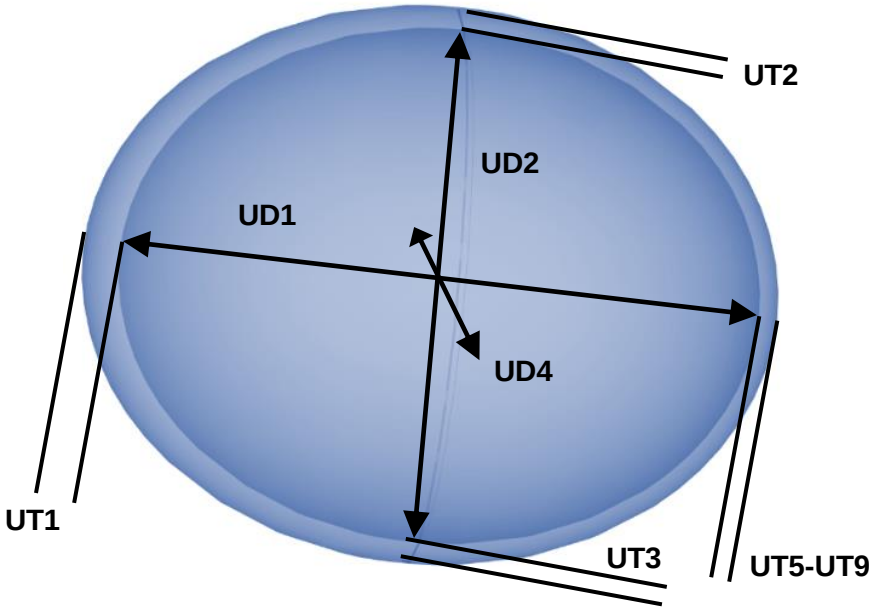

Figure 17: Ellipsoidal representation of uterus. Parameters beginning with UT are uterine thickness measurements, UD are uterine distance measurements, CA are cervical angles, and CD are cervical distance measurements.

3.2.3.2 Cervix

The cervix is generated as a long solid cylinder of specified width CD2 that is positioned on the lower uterine segment according to the posterior cervical offset (UD4 in Figure 15) and cut down to a specific length according to the model inputs. The cervical angle CA1 defines the angle of incidence of the cervix with respect to the lower uterus. The inner canal, another narrower cylinder of diameter CD3, is Boolean subtracted from the cervix to complete the hollow thick-walled cylinder geometry of the cervix.

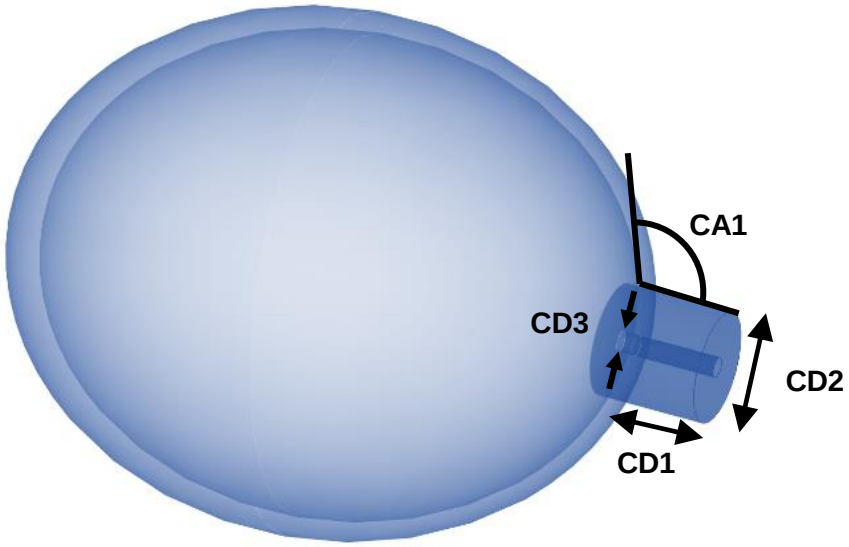

Figure 18: Uterus with cervix attached

After assembling the uterus and cervix, the two volumes are blended together so that the sharp corners at the interface between them are removed. Rounding radii are calculated to create a smooth transition from the uterine wall thickness to the cervical wall thickness. The result, shown in Figure 19, is a geometry that better matches the organic, rounded features that can be seen in vivo. This smoothing and rounding have the added benefit of reducing unrealistic strain concentration artifacts that would have occurred if sharp corners had been left in this part of the model.

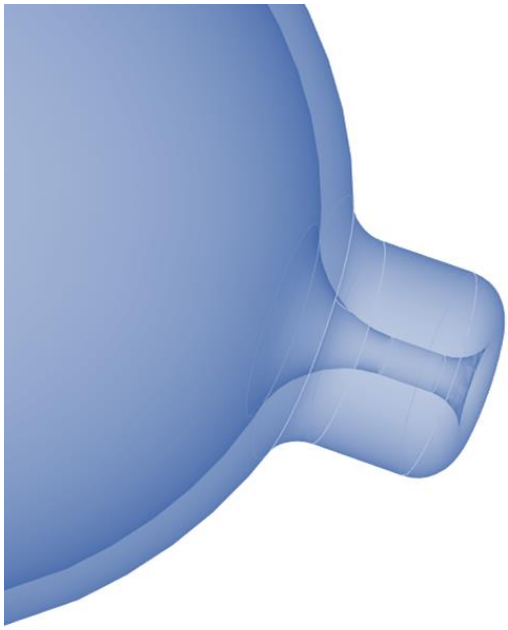

Figure 19: Rounding of the connection between the uterus and cervix.

For the purposes of enabling a more granular post-simulation analysis, the cervix is subdivided into three regions at this step, as illustrated in Figure 20: Partitioning of the cervix. The cervix is sliced 15 mm from the internal *os*, perpendicular to the inner cervical canal. The portion of the cervix distal to that cut plane is designated as the "lower cervix." The remaining proximal portion of the cervix is further subdivided using a cylindrical cut at twice the diameter of the inner cervical canal. The inner resulting volume is arbitrarily defined to be the "internal *os*" for our analyses. The remaining portion is designated as the "upper cervix."

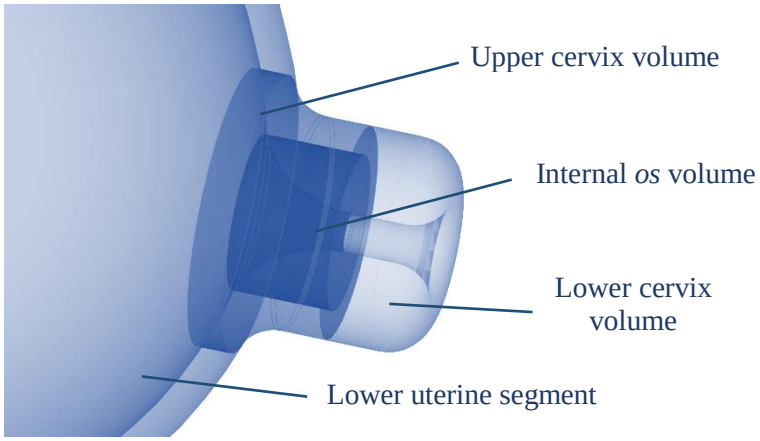

Figure 20: Partitioning of the cervix.

3.2.3.3 Fetal Membrane/Amnion

The dominant load bearing portion of the fetal membrane is the amnion [2]. In our model, the inner uterine wall ellipsoid is copied to generate the outer wall of the fetal membrane. The outer wall is then extruded inward a distance of 0.1 mm to reflect a nominal membrane thickness [2]. The membrane is procedurally meshed using hex elements at this stage (Figure 21).

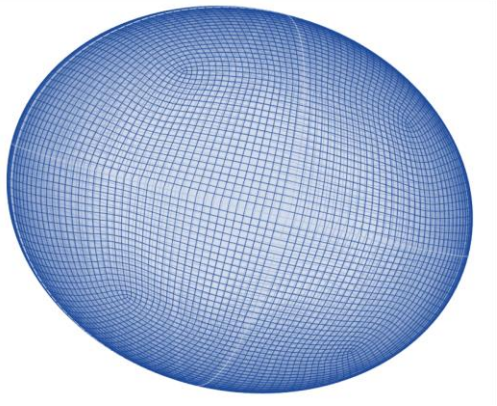

Figure 21: One-element-thick layer forming the amnion, 0.1 mm thickness.

3.2.3.4 Abdomen and Vaginal Canal

The abdomen is generated by extruding splines to form a 3D volume, then the vaginal canal is Boolean subtracted along with the uterus and cervix.

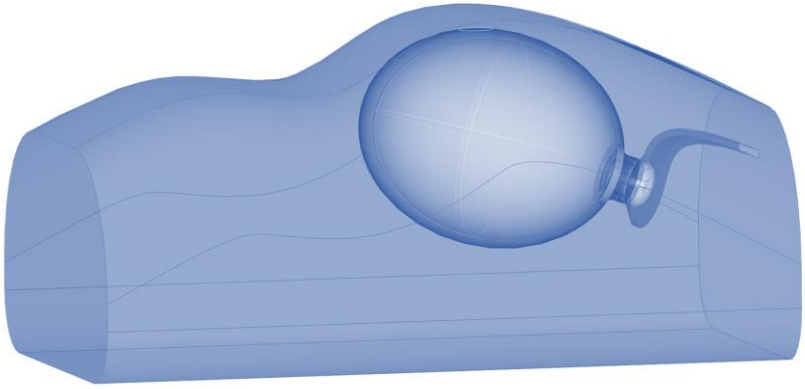

Figure 22: Parameterized model with abdomen, uterus, cervix, and vaginal canal.

3.2.4 Geometries Built

Table 5: Model geometries compared in the parameterized study. Bold emphasizes varied parameter.

Model	Cervical angle (deg)	Cervical length (mm)	Cervical offset (mm)	Cervical stiffness
Baseline	90	30	25	soft (term), stiff
AUCA	**90 → 110**	30	25	soft (term), stiff
CL	90	**25 → 40**	25	soft (term), stiff
PCO	90	30	**0 → 25**	soft (term), stiff
Cervical stiffness	90	30	25	**soft (term) → stiff**

3.2.5 Mesh

With the exception of the fetal membrane, we meshed all volumes with tetrahedral elements. The mesh density is an easily modifiable parameter of the model, and as such varies from case to case, but information about a typical mesh is given in Table 6.

Table 6: Mesh properties for a typical generated model

	Total	Uterus	Cervix	Membrane	Abdomen
Element Type	-	Tet	Tet	Hex	Tet
Element Count	110,200	26,000	42,000	9,600	32,600
Average Element Volume	-	19 mm^3	0.5-1.0 mm^3	0.8 mm^3	1050 mm^3

The fetal membrane is a single continuous layer of hexahedral elements with a thickness of 0.1 mm and no edges longer than 3 mm. We wrote a step-by-step, single layer hex meshing routine for the membrane into the model generation script. A typical membrane mesh contains 9600 hexahedral elements.

The uterus and cervix are connected at the node level to each other, so their boundaries are shared and must move congruently. Where the uterus and cervix share a boundary with the abdomen volume, those boundaries are also node-tied. The lower cervix is not tied to the interior vaginal canal but floats freely inside the vaginal fornix.

3.2.6 BCs and Loads

In order to have supportive but compliant boundary conditions for the uterus and cervix, we chose to surround them with a uniform abdominal material volume with a low stiffness (~1kPa) neo-Hookean material definition. The anterior, posterior, left, and right surfaces of the abdominal volume are fixed in 3D space, replicating the ribcage, but the superior and inferior ends are free to deform so that changes in volume can be accommodated.

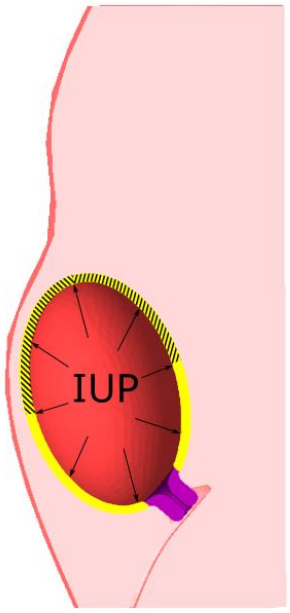

Figure 23: Boundary and load conditions applied to the FM. The superior half of the uterus and fetal membrane are fixed in 3D space, while a uniform intrauterine pressure is applied inside the membrane. The inferior half of the uterus and the cervix are free to deform and displace the much softer abdominal tissue.

To achieve numerical solver stability and to reproduce the correct mechanical loading state near the internal *os*, the superior half of the fetal membrane is fixed in 3D space while its interior is prescribed an intrauterine pressure that ramps linearly over a range of 0 to 3 kPa. This range of IUP values spans the range of reported pressures we found in the literature [60] for baseline uterine tone up to 40 weeks.

3.3 Material Models

3.3.1 Uterus and Cervix Models

For the uterus and cervix, a fiber composite material with a neo-Hookean ground substance and random orientation continuous fiber distribution was used. The fiber network strain energy density Ψ_r, is given by

$$\Psi_r(\boldsymbol{C}) = \int_A H(I_n - 1)R(\boldsymbol{n})\Psi_n(I_n)dA. \quad (12)$$

In this equation, **n** is the unit vector along the fiber orientation in the reference configuration, $I_n = \boldsymbol{n} \cdot \boldsymbol{C} \cdot \boldsymbol{n}$ is the normal component of the right Cauchy-Green deformation tensor **C** along **n**, and $\boldsymbol{A}$ represents the unit sphere over which the integration is performed. Inside the integrand, $\boldsymbol{H}$ is the Heaviside unit step function that includes only fibers that are in tension, $\boldsymbol{R}$ is the fiber density distribution function that specifies the spatial normalized distribution of fibers, and Ψ_n represents the strain energy density of the fiber bundle oriented along **n**. The fiber density distribution function satisfies the constraint

$$\int_A R(\boldsymbol{n})dA = 1. \quad (13)$$

The fibers in the uterus and cervix are represented by an exponential power law. The fiber strain energy density Ψ_n is given by

$$\Psi_n(I_n) = \frac{\xi}{\beta}\left(\exp\left[(I_n - 1)^{\beta}\right] - 1\right) \quad (3)$$

where $\xi > 0$, and $\beta \geq 2$. This model accounts for the fibrous nature of the uterus in its passive state (We did not simulate active uterine contractile behavior).

3.3.1.1 "Soft" Cervical Material

The material properties of the cervix were found by fitting the model to uniaxial tension/compression force-displacement data from our previous work [1] similar to the procedures in [26]. This material represents a pregnant cervix that has remodeled and gone through an initial softening phase but not the last ripening phase. These tissue samples were taken via caesarean hysterectomy before the labor process began (as described in [1]).

Table 7: Soft cervical material properties

Neo-Hookean ground substance

Property	E	ν	β	ξ	distribution
Value	0.00065	0.3	2	0.0017	spherical

3.3.1.2 "Stiff" Cervical Material

This model follows the same considerations as the soft material model, except that mechanical test data are from nonpregnant tissue specimens.

Table 8: Stiff cervical material properties

Neo-Hookean ground substance

Property	E	ν	β	ξ	distribution
Value	0.00065	0.3	3.12	0.077	spherical

3.3.1.3 Uterine Material Model

Stretch data from tensile tests of human uterine tissue [61] were employed to generate material properties for this fiber composite model of passive pregnant uterus.

Table 9: Uterine material properties

Neo-Hookean ground substance

Property	E	ν	β	ξ	distribution
Value	0.002	0.3	2.72	0.019	spherical

3.3.2 Amnion Material Model

The FM was modeled as an Ogden nonlinear material meshed with hexahedral elements (Trelis). In an Ogden material, the uncoupled hyperelastic strain energy function, Ψ, is given in terms of the eigenvalues of the deformation tensor:

$$\Psi = \sum_{i=1}^{N} \frac{c_i}{m_i^2}\left(\tilde{\lambda}_1^{m_i} + \tilde{\lambda}_2^{m_i} + \tilde{\lambda}_3^{m_i} - 3\right) + U(J), \tag{3}$$

where $\tilde{\lambda}_i^2$ are the eigenvalues of $\widetilde{\boldsymbol{C}}$, c_i and m_i are material coefficients and N ranges from 1 to 6. The properties used were derived from data on biaxial tension tests of delivered FMs [2] and are reported in Table 10: Ogden Material Properties for the Amnion.

Table 10: Ogden Material Properties for the Amnion

(as specified in FEBio)

Property	k	*c*1	m1	c2	m2	c3	m3
Value	1000	0.85875	27.21	0.00368	27.21	0.75645	-16.64

3.4 Simulation Steps

The simulations ran for IUP levels from 0 to 10 kPa. The intrauterine pressure was increased linearly after contact interfaces initialized. The models were solved on a PC with an Intel Core i7 processor and 32 GB of RAM. Simulations took between 20 minutes and two hours to completely solve.

3.5 Results

Large differences in right Cauchy-Green stretch occur between each variation in cervical parameters. Results are shown for each geometric variation using both soft and stiff cervical material properties and indicate that geometric variations in length and offset are more crucial in a softer cervix, while geometric variation in angle is more crucial in a stiffer cervix. At a uniform IUP of 8.67 kPa, circumferential stretch is observed in the internal *os* region, and radial stretch upward from the uterus is observed at the uterocervical interface in the anterior and posterior directions Figure 24. This radial stretch is likely contributed to by fetal membrane adhesion at both the inner uterine surface and the inner surface of the top cervix region. Arrows in the plot indicate directionality of the principal stretch.

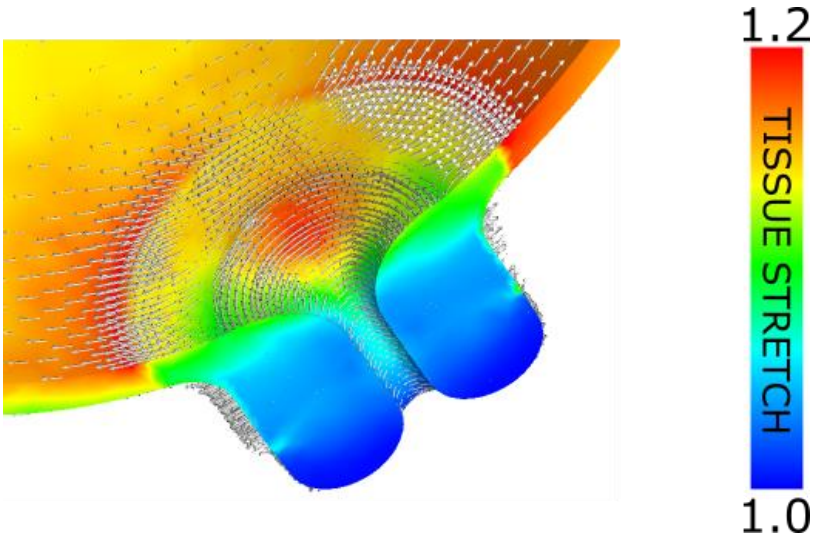

Figure 24: Right Cauchy-Green stretch results using a random continuous distribution fiber model in the cervix.

3.5.1 Anterior Uterocervical Angle

Anterior uterocervical angle (AUCA) was varied in ten-degree increments from 90° in the baseline model to the most extreme value of 110° with respect to the anterior LUS. AUCA in this analysis can be defined as the angle between the cervical inner canal and the anterior LUS (CA1 in Figure 15). Our results show that as AUCA is increased, cervical right Cauchy-Green stretch of the internal *os* region increases. This result contradicts recent clinical findings related to the impact of cervical angle as an indicator of PTB [14].

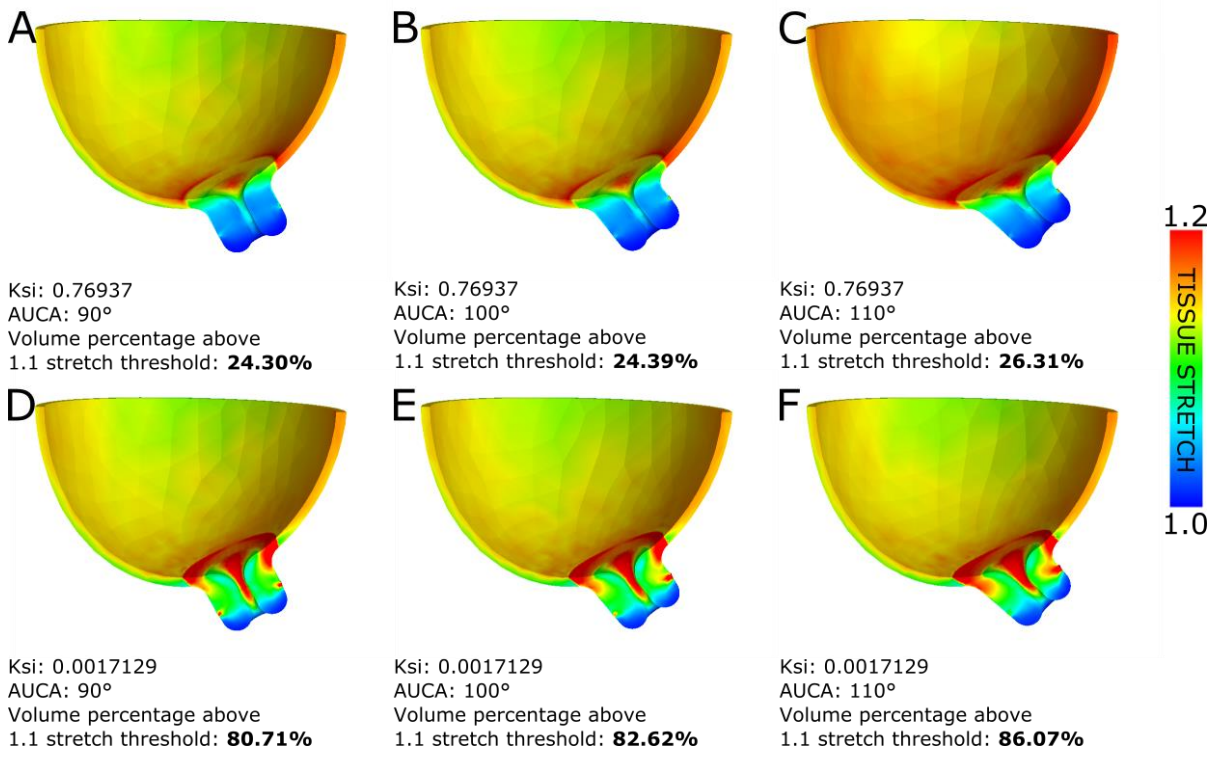

Figure 25: Cervical stretches increase in the internal *os* region as the AUCA increases. We show here the percentage of the internal *os* region above a 1.1 stretch threshold for (A) stiff cervix with AUCA of 90°, (B) stiff cervix with AUCA of 100°, (C) stiff cervix with AUCA of 110°, (D) soft cervix with AUCA of 90°, (E) soft cervix with AUCA of 100°, and (F) soft cervix with AUCA of 110°.

In the stiff cervix material model, the 110° AUCA experiences an 8.3% increase in cervical stretch from the 90° AUCA. In the soft cervix material model, the 110° AUCA experiences a 6.6% increase in cervical stretch from the 90° AUCA. In both models, a perpendicular AUCA presents minimal stretch in the cervical internal *os* region.

3.5.2 Cervical Length

CL was varied in 5 mm increments from 25 mm (the clinical definition of a "short cervix") to 40mm. CL in this analysis can be defined as the length of the inner canal from the internal *os* to the external os (CD1 Figure 15). Our results show that as CL is increased, cervical right Cauchy-Green stretch of the

internal *os* region decreases (Figure 26). This trend is in agreement with the use of short sonographic cervical length as an indicator for higher PTB risk.

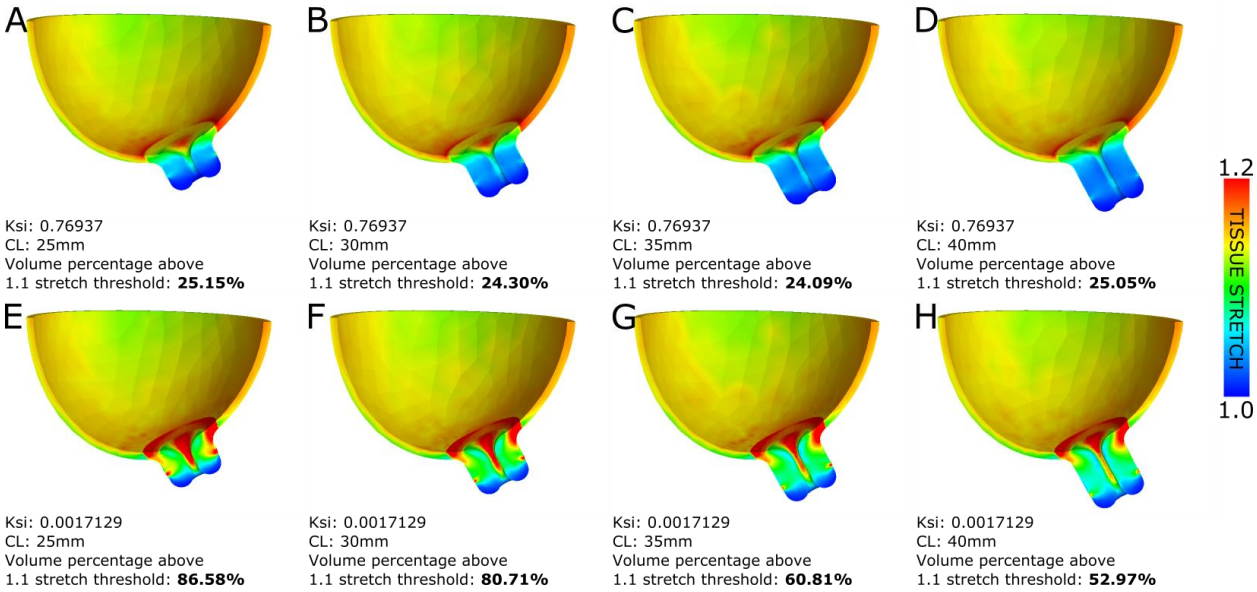

Figure 26: For a soft cervix, short cervical length leads to higher stretches in the internal *os* region. Shown here are volume percentages of the internal *os* region above a 1.1 stretch threshold for (A) stiff cervix with CL of 25 mm, (B) stiff cervix with CL of 30 mm, (C) stiff cervix with CL of 35 mm, (D) stiff cervix with CL of 40 mm, (E) soft cervix with CL of 25 mm, (F) soft cervix with CL of 30 mm, (G) soft cervix with CL of 35 mm, and (H) soft cervix with CL of 40mm.

In the stiff cervix material model, the 25 mm CL experiences a 0.4% increase in cervical stretch from the 40 mm CL. However, this trend is inconsistent in the intermediary 30 mm and 35 mm CLs. However, a trend is more prominent in the softer soft cervix material model, where the 25 mm CL experiences a 63.5% increase in stretch from the 40 mm CL, with intermediary values corresponding to this increasing trend. The minimal increase in the stiff cervix material model suggests that clinically, sonographic cervical length and cervical stiffness measurements should be taken simultaneously, as a short cervix could result in a false positive of PTB in patients with a stiff cervix.

3.5.3 Posterior Cervical Offset

PCO was varied in 5 mm increments from 0 mm to the baseline value of 25mm. PCO in this analysis can be defined as the distance from the longest uterine diameter to the cervical internal *os* (UD4 Figure 15). Our results show that as PCO is increased, cervical right Cauchy-Green stretch of the internal *os* region increases (Figure 27).

A

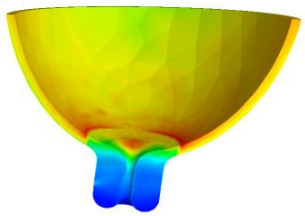

Ksi: 0.76937
PCO: 0mm
Volume percentage above
1.1 stretch threshold: **17.72%**

B

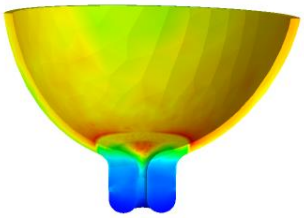

Ksi: 0.76937
PCO: 5mm
Volume percentage above
1.1 stretch threshold: **18.12%**

C

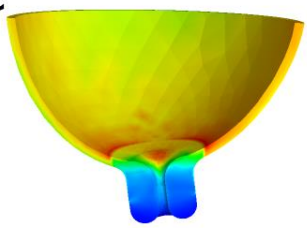

Ksi: 0.76937
PCO: 10mm
Volume percentage above
1.1 stretch threshold: **19.03%**

D

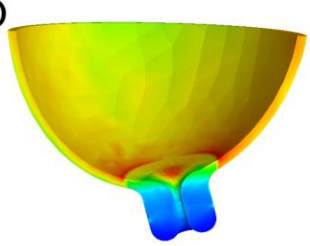

Ksi: 0.76937
PCO: 15mm
Volume percentage above
1.1 stretch threshold: **20.87%**

E

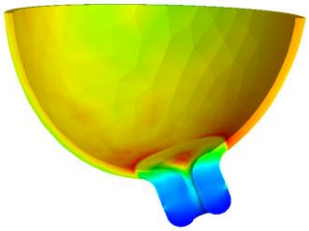

Ksi: 0.76937
PCO: 20mm
Volume percentage above
1.1 stretch threshold: **22.03%**

F

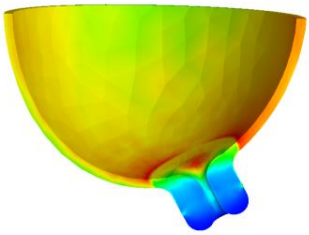

Ksi: 0.76937
PCO: 25mm
Volume percentage above
1.1 stretch threshold: **24.30%**

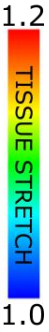

G

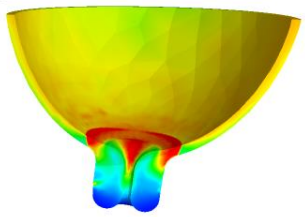

Ksi: 0.0017129
PCO: 0mm
Volume percentage above
1.1 stretch threshold: **30.71%**

H

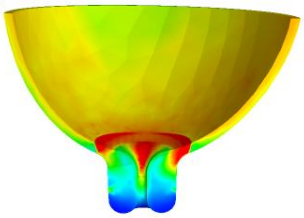

Ksi: 0.0017129
PCO: 5mm
Volume percentage above
1.1 stretch threshold: **31.90%**

I

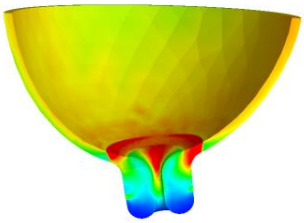

Ksi: 0.0017129
PCO: 10mm
Volume percentage above
1.1 stretch threshold: **32.95%**

J

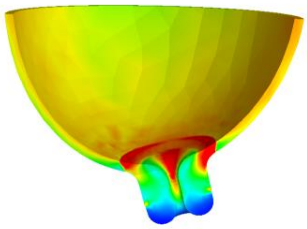

Ksi: 0.0017129
PCO: 15mm
Volume percentage above
1.1 stretch threshold: **38.93%**

K

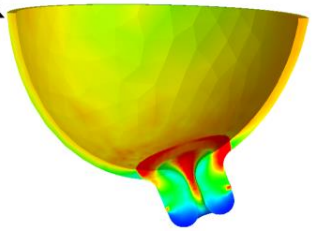

Ksi: 0.0017129
PCO: 20mm
Volume percentage above
1.1 stretch threshold: **66.64%**

L

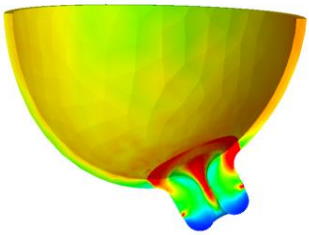

Ksi: 0.0017129
PCO: 25mm
Volume percentage above
1.1 stretch threshold: **80.71%**

Figure 27: Stretch increases as the posterior cervical offset distance is increased, especially in the case of a soft cervix. We show here volume percentages of the internal *os* region above a 1.1 stretch threshold for (A) stiff cervix with PCO of 0 mm, (B) stiff cervix with PCO of 5 mm, (C) stiff cervix with PCO of 10 mm, (D) stiff cervix with PCO of 15 mm, (E) stiff cervix with PCO of 20 mm, (F) stiff cervix with PCO of 25 mm, (G) soft cervix with PCO of 0 mm, (H) soft cervix with PCO of 5 mm, (I) soft cervix with PCO of 10 mm, (J) soft cervix with PCO of 15 mm, (K) soft cervix with PCO of 20 mm, and (L) soft cervix with PCO of 25mm.

In the stiff cervix material model, the 25 mm PCO experiences a 37.1% increase in cervical stretch from the 0 mm offset, with intermediary values corresponding to this increasing trend. In the soft cervix material model, the 25 mm PCO experiences a 162.8% increase in cervical stretch from the 0 mm offset, with intermediary values corresponding to this increasing trend.

3.5.4 Cervical Stiffness

Cervical stiffness was varied by decreasing fiber stiffness from the stiff value of 0.76937 by an order of 4.6 to reach the soft value of 0.0017129. All other parameters in the material model were kept constant. Our results show that as the cervix is made softer, cervical right Cauchy-Green stretch of the internal *os* region increases (Fig. 9). The soft cervix material model experiences a 232.1% increase in cervical stretch from the stiff cervix material model.

Table 11: Uterine and cervical tissue variables taken from material fits to experimental data. These values are implemented in a continuous fiber distribution material model used in FEBio 2.4.1.

Tissue description	E	ν	β	ξ
Uterus – NP	0.002	0.3	3	0.19
Cervix – term PG	0.002	0.3	3.12	0.0017129
Cervix – intermediate 1	0.002	0.3	3.12	0.007886
Cervix – intermediate 2	0.002	0.3	3.12	0.036302
Cervix – intermediate 3	0.002	0.3	3.12	0.167122
Cervix – NP	0.002	0.3	3.12	0.76937

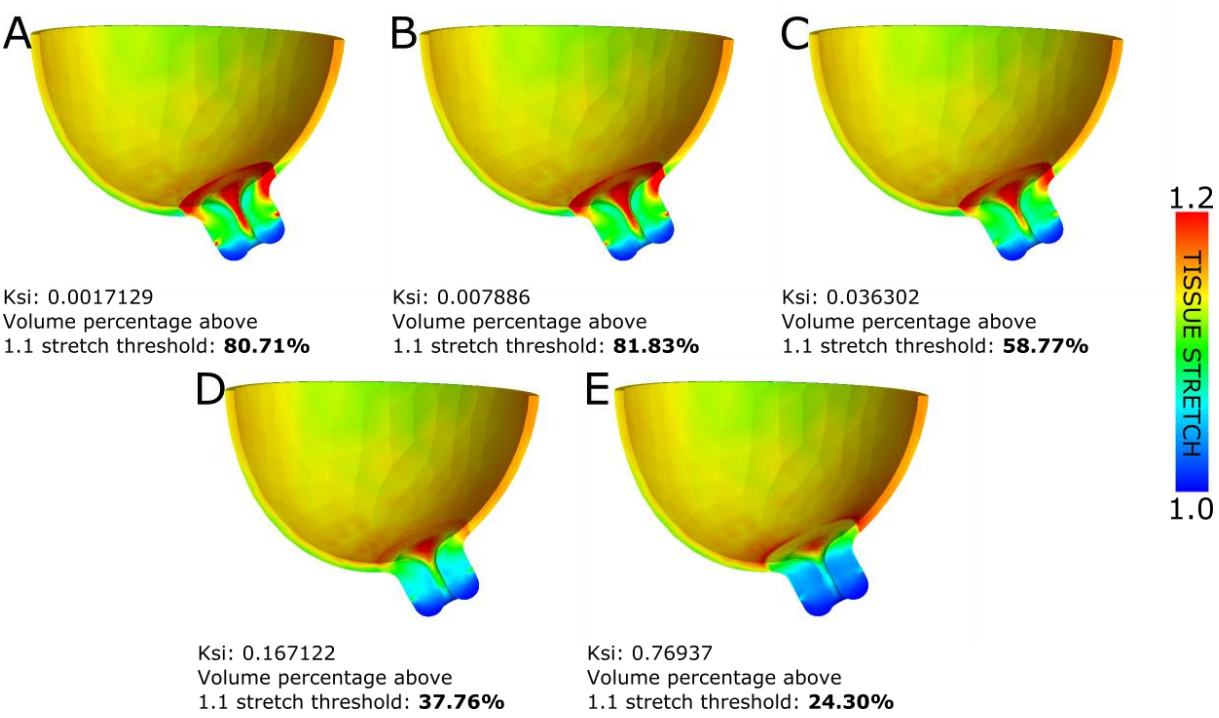

Figure 28: Cervical stretches decrease as cervical material fiber stiffness increases. Volume percentage of internal *os* region above a 1.1 stretch threshold for (A) soft cervix, (B) cervix – intermediate 1, (C) cervix – intermediate 2, (D) cervix- intermediate 3, (E) stiff cervix. Details for material properties are given in Table 11.

3.6 Discussion

Results indicate that geometric variations in cervical length and offset are more impactful in a softer cervix, while geometric variation in angle causes larger differences in deformation patterns in a stiffer cervix. At a uniform IUP of 8.67 kPa, circumferential stretch is observed in the internal *os* region, and radial stretch upward from the uterus is observed at the uterocervical interface in the anterior and posterior directions. This radial stretch is likely contributed to by fetal membrane adhesion at both the inner uterine surface and the inner surface of the top cervix region.

Changing uterocervical angle within the ranges we simulated did not contribute significantly to stretch levels in the cervix. This result contradicts recent clinical findings related to the impact of cervical angle as an indicator of PTB [14]. In the stiff cervix material model, the 110° AUCA experiences an 8.3% increase in cervical stretch from the 90° AUCA. In the soft cervix material model, the 110° UCA

experiences a 6.6% increase in cervical stretch from the 90° AUCA. In both models, a perpendicular AUCA presents minimal stretch in the cervical internal *os* region.

Our results show that as CL is increased, cervical right Cauchy-Green stretch of the internal *os* region decreases (Fig. 7). This conforms to the current clinical sonographic indicator of a short cervix. In the softer soft cervix material model, the 25 mm CL experiences a 63.5% increase in stretch from the 40 mm CL, with intermediate values following this increasing trend. The minimal change in stretch the stiff cervix material model as cervical length was varied suggests that clinically, sonographic cervical length and cervical stiffness measurements should be taken simultaneously, as a short cervix could result in a false positive of PTB in patients with a stiff cervix.

Posterior cervical offset (PCO) was varied in 5 mm increments from 0 mm to the baseline value of 25mm. PCO in this analysis can be defined as the distance from the longest uterine diameter to the cervical internal *os* (UD4 in Figure 15). Our results show that as PCO is increased, cervical right Cauchy-Green stretch of the internal *os* region increases (*Figure 27*).

Cervical stiffness was varied by decreasing fiber stiffness from the stiff value of 0.76937 by a power of 4.6 to reach the soft value of 0.0017129. All other parameters in the material model were kept constant. Our results show that as the cervix is made softer, cervical right Cauchy-Green stretch of the internal *os* region increases (Fig. 9). The soft cervix material model experiences a 230% increase in cervical stretch from the stiff cervix material model.

3.7 Limitations

Simplifying assumptions in this model include the difference between actual anatomic geometry and the simplified geometry, the assumption of material property homogeneity, the lack of dynamic analysis and tissue growth, the fact that measurements were taken *in-vivo* in a loaded configuration then used as the dimensions for the reference configuration, and others. Any finite element model is an imperfect

representation of a mechanical system, but we believe this model is the most flexible and detailed biomechanical model of pregnancy to date, and that it can be confidently used to study relative comparisons in loading under the specific scenarios we described.

3.8 Validation

3.8.1 Validation Goal

While the MRI-based segmentation method to acquire pelvic anatomic geometry can produce detailed representations of the anatomy, it is a very time consuming (days) and difficult process to complete, requiring many steps from MRI scan to segmentation, meshing, mesh repair, manual model assembly, boundary condition specification, and more. It is difficult to imagine such a process taking hold clinically as a widely used tool. To facilitate the creation of a more clinically applicable simulation, we aimed to find a faster method to create anatomical geometry of the pregnant uterus, cervix, and fetal membrane.

Such geometry can be built using a set of anatomic measurements which are then used to build custom-sized geometric features representing the uterus, cervix, membrane, and abdomen. The measurements can be taken using any sufficient medical imaging modality. In our case, ultrasound measurements have been identified to provide adequate information while fitting inside the scope of typical clinical imaging practices. This kind of parametric model, because it is fundamentally primitive geometric objects, is more suitable for automatic finite element mesh generation and automated boundary condition and loading specifications. This enables remarkable possibilities for our overall modeling goals in the areas of general process automation and speed improvement.

The details of how the new geometry method works are given in Section 3.2. Here, we compare results derived from the MRI segmentation-based geometry to results that came from the parametric geometry method. From the comparison, we can understand the impact of changing our geometry strategy on the resulting loading patterns predicted by our models.

3.8.2 Validation Methods

For comparison against our original MRI-based method, we took characteristic maternal anatomy measurements from a pregnant 28-week patient for which an MRI-based model was previously created. The measurements were taken using the point-to-point 3D measuring tool within the Simpleware ScanIP software (Version 6.0, Exeter, UK). The measurements, shown in Table 12, were input into the new parameterized model, then both models were subjected to the same IUP loading with identical material properties and boundary conditions, including a sliding membrane condition. Within both the MRI-based and parametric models, we used the same fiber-composite uterine and cervical material models and a 0.1 mm membrane layer, removing all surrounding tissue boundary conditions and fixing the uterus in 3D space at the top of the lower uterine segment. The membrane was placed in contact with the inner uterine wall, using a sliding contact condition over the entire area of contact.

Table 12: Maternal anatomy measurements are given as taken from the MRI image stack of Patient 2. (Scan performed at 28 weeks' gestation. See section 2.1 for detailed obstetric history.)

Measurement	Value
Uterine transverse inner diameter	10.5 cm
Uterine ant/post inner diameter	8.9 cm
Uterus longitudinal inner diameter	20.1 cm
LUS thickness	0.85 cm
Uterine fundus thickness	1.0 cm
Uterus transverse thickness	0.85 cm
Uterus ant/post thickness	0.85 cm
Cervical canal diameter	0.6 cm
Cervix outer diameter	2.3 cm
Cervix length	3.8 cm
Anterior uterocervical angle	55 degrees
Posterior cervical offset	0.5 cm

For the MRI geometry, we used FEBio's multi-generation material model to achieve the membrane contact condition. A neo-Hookean material with modulus $E = 2.5\ kPa$ and Poisson's ratio $\nu = 0.3$ was used for the membrane from $t = 0$ to $t = 0.001$ seconds in the simulation. During that time, the intrauterine pressure was increased from 0 to 0.001 kPa, which was adequate to achieve conformity and contact between the membrane and the interior uterine wall. After contact was achieved, the Ogden material model described in Section 3.3.2 was enabled, and it dominates the stress-strain response of the simulation results we present here (effects from the underlying neo-Hookean material can be neglected). In the parameterized model, the membrane is precisely created to be in perfect conformity with the uterine geometry, so use of the multi-generation model was not necessary. Only the Ogden material described in Section 3.3.2 was used for the membrane of the parametric model.

An IUP from 0 to 0.817 kPa was applied gradually to the interior of the membrane, and the results were compared in both models at an IUP of 0.817 kPa, a value representing a nominal intrauterine pressure without contraction. Note that for the MRI model, all strains were calculated using the time step after membrane conformity as the reference configuration, to eliminate any initial artifacts of strain.

3.8.3 Validation Results and Discussion

Comparisons of the first principal strain and the effective (RMS) strain in the MRI-based model and the parameterized model are shown in Figure 29 and Figure 30. The parameterized model has a more uniform strain distribution than the MRI-based geometry. In the area adjacent to the internal *os*, where the cervix forms an acute angle with the uterine wall, the MRI-based model predicts compressive strains near 0.3 and tensile strains on the order of 0.25, while the parameterized model predicts the strains to be closer to 0.1 and 0.1, respectively.

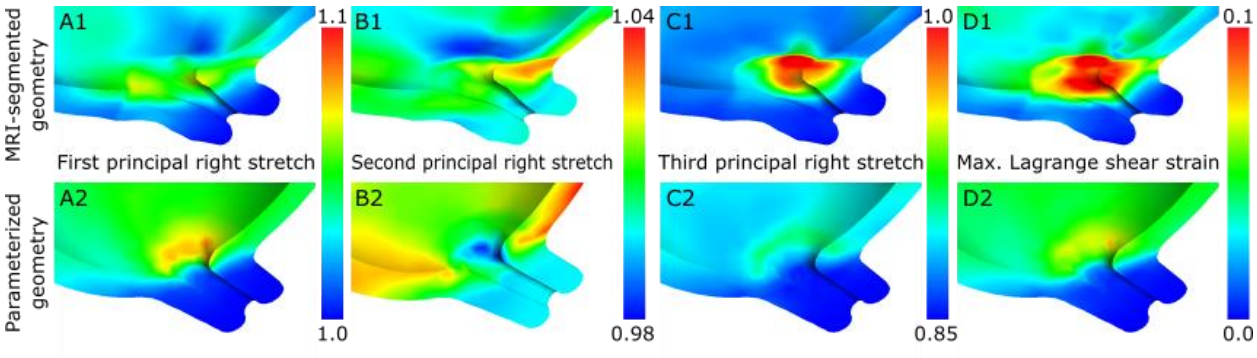

Figure 29: Principal right stretch plots of the MRI geometry model (A1) and the parameterized geometry model (A2) under an IUP of 0.816 kPa applied to the fetal membrane. First principal stretches (A1, A2) reflect the areas of highest tension and are concentrated around the internal *os* and the proximal portion of the cervix. Third principal strains (C1, C2) represent areas of compression, which are most prominent in the MRI model (C1). Shear strains are shown in figures D, and are also concentrated over the internal *os*, but are approximately twice as large in the MRI-derived model due to the irregular surface of the geometry.

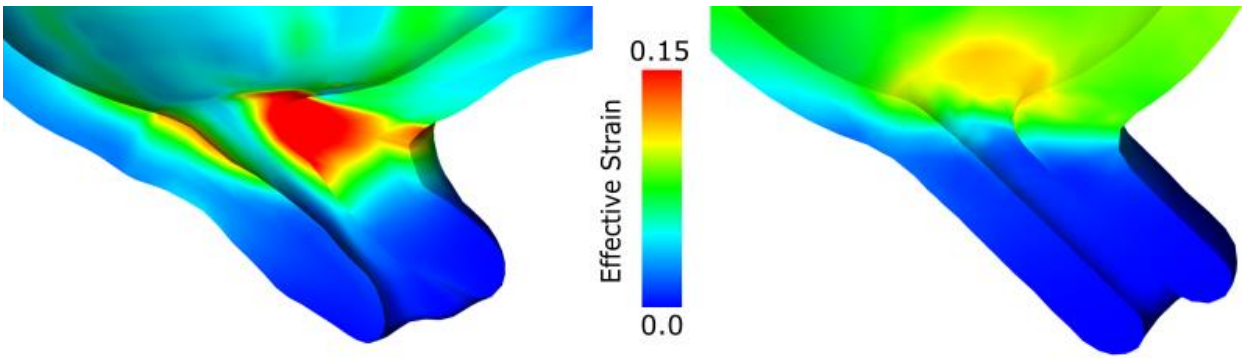

Figure 30: Effective strains in the MRI geometry model and the parameterized geometry model under an IUP of 0.816 kPa applied to the fetal membrane. The MRI model shows much greater effective strain levels near the internal *os* resulting from geometric irregularities that are not fully captured by the parametric model.

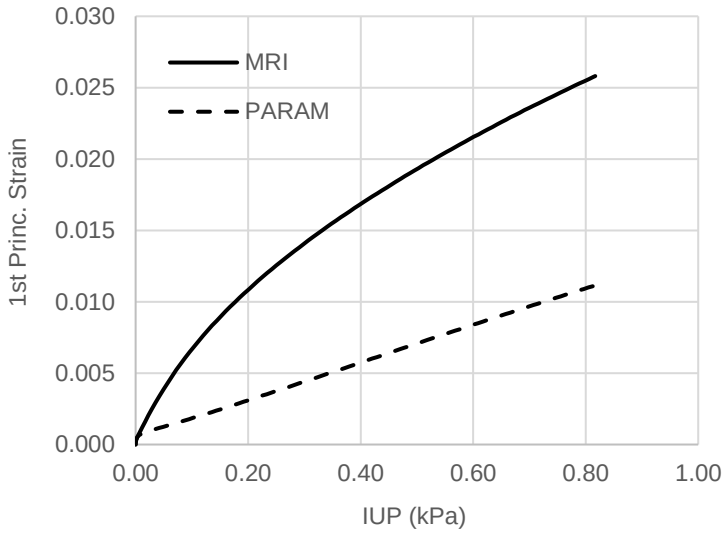

Figure 31: Average first principal strain as a function of intrauterine pressure applied to the membrane. Strain was calculated in each element then an element volume-weighted average was performed. Results from the MRI-based geometry are compared to the parameterized geometry. The gradual decrease in slope in the strain of the MRI geometry is partially explained by the straightening out and "un-wrinkling" of the geometry.

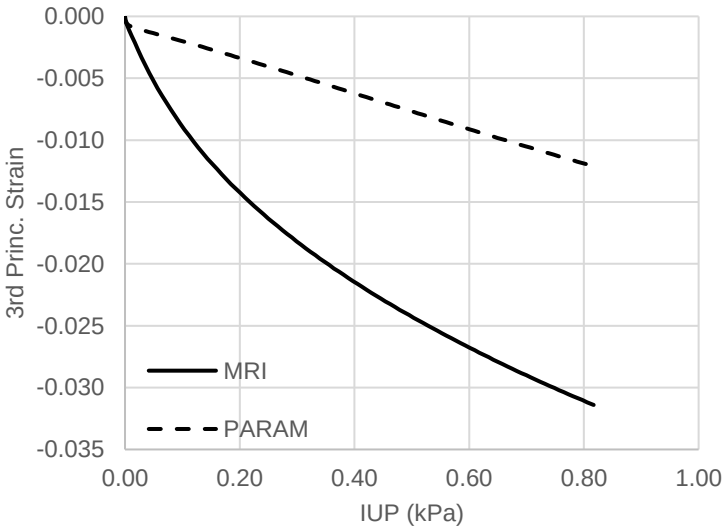

Figure 32: Average third principal strain as a function of intrauterine pressure applied to the membrane. Strain was calculated in each element then an element volume-weighted average was performed. Results from the MRI-based geometry are compared to the parameterized geometry. The gradual increase in slope in the strain of the MRI geometry is partially explained by the straightening out and "un-wrinkling" of the geometry.

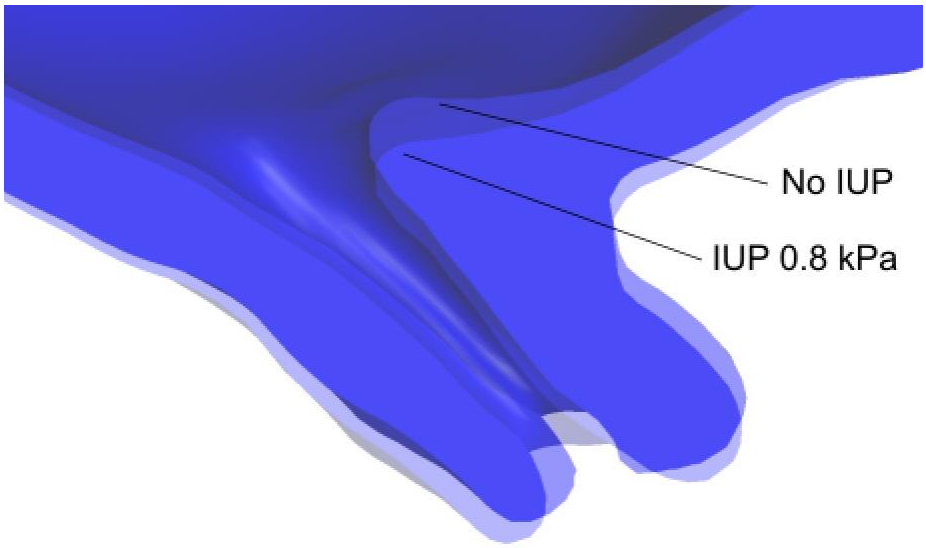

Figure 33: There is a large change in shape near internal *os* of the MRI-based model when IUP is applied to the membrane.

.

Overall, the parameterized model predicts similar locations for strain concentration patterns as the MRI-segmented model does. Figure 29: A1-D2 demonstrate that the largest differences occur at the site of a geometric feature in the MRI-based model at the location of the posterior internal *os*. At this location, the top of the cervix protrudes slightly into the volume of the uterus. This geometric irregularity cannot be captured in the current set of geometric measurements we have defined. Clinically, any measurements need to be well-defined, repeatable, and easily teachable to ensure correct procedures are followed. Characterization of these kinds of geometric features is doubly challenging as the internal pelvic anatomy is not static, and can change substantially even during the same ultrasound session (for example, with contractions or from the bladder filling or being emptied).

Because both models use exactly the same material models and membrane contact definitions, this disagreement must arise from differences between the geometries. In particular, the MRI model geometry is inherently less geometrically stiff in the mode of internal pressurization because it has “hills” and “valleys” on the surface, making it equivalent to a rope with slack being pulled under tension. On the other

hand, the geometric primitive-based ellipsoidal geometry in the parameterized model has less play under increasing internal pressurization, because its basic geometry is more stable.

These effects will be important to characterize in future iterations of the model, and a mechanism to capture this behavior will be developed. The mechanism may take the form of better replicating the *in-vivo* geometry or of modifying the constitutive model to reduce the low-strain stiffness to an amount equivalent to the geometric slack we see in the MRI-models.

Despite the differences between the results of each method, the parameterized model is an important tool in bridging the gap between future numerical clinical tools and the current clinical state of the art due to its unlimited flexibility and much reduced "patient measurement to simulation" timeline.

4 Evaluating the Function of the Cervical Pessary Using FEA

4.1 Motivation

The cervical pessary, also known as the cerclage pessary or Arabin pessary, is a flexible silicon device which encircles the pregnant cervix [62]. It is used in patients who are at risk for spontaneous PTB associated with a short cervix and cervical insufficiency [63]. Figure 34 illustrates the location of a pessary after the trans-vaginal, nonsurgical insertion procedure is performed. The pessary is intended to rest on the posterior vaginal wall while mechanically supporting the cervix at its connection to the vaginal canal.

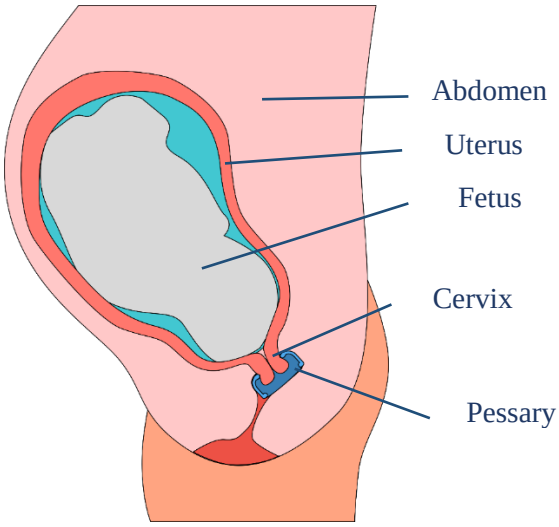

Figure 34: The pessary (blue) is placed within the vaginal canal, encircling the cervix.

The cervical pessary is intended to reduce the likelihood of PTB by slowing or reversing the progression of funneling and preterm dilation. Several mechanisms for how it could work are postulated by the inventors of the pessary and other clinicians. Proposed mechanisms include: a) angling the cervix toward the posterior, bringing the external *os* toward the sacrum [62], [64], b) mechanically closing the cervix with the constraining geometry of the device [62], [65], and c) preserving the mucous plug [62], [66].

The efficacy of the pessary has been investigated in several notable clinical studies. A randomized controlled 2012 study [67] by Goya, et al. found that the pessary was effective at reducing PTB in women with cervical length less than 25 mm or less, reporting a frequency of PTB of 27% in the control group and 6% in the pessary group. A study [68] in 2013 by Liem, et al. on prophylactic use of the cervical pessary to treat women pregnant with twins reported no significant difference in PTB rates in prophylactic use when cervical length was not considered. For the group with cervical length less than 38 mm, poor perinatal outcome *was* reduced in the pessary group. This was not the case in the group with a cervical length greater than or equal to 38 mm. In a small 2015 study [65] by Gimovsky, pessary was *not* found to perform better than expectant management and was associated with more frequent PTB compared to treatment with a cerclage. Two 2016 studies by Nicolaides et al. found no reduction in PTB from pessary use over expectant management for both twin and singleton pregnancies [69], [70]. On the other hand, Goya et al. in the "PECEP" [71] study found a significant reduction (from ~40% to ~16%) in PTB rates for twin mothers with a short cervix who were treated with a pessary. The Nicolaides studies described how researchers "introducing the cervical pessaries received instruction on selecting the appropriate size and introducing the device," while a single pessary size was used for all patients who participated in the 2015 study by Goya, et al.

The size of a pessary may have a large effect on its efficacy. Without controlling for and standardizing the reporting of pessary sizes used in clinical trials, it will likely be difficult to extract useful information. As we demonstrate in this study, the size of the device directly impacts its mechanical interactions with the cervix [64]. Here, we analyze the cervical pessary and its performance within the complex mechanical environment of the pregnant human body through the use of parametric finite element analysis (FEA). We assess the relative change in magnitude and placement of the mechanical load on the cervix with pessary placement in various anatomical scenarios and show that optimal use of the pessary depends on tissue material and anatomical variables.

4.2 Materials and Methods

Multiple 3D finite element analysis (FEA) computer models of the predominant anatomic features of pregnancy were created to understand the distribution and relative magnitude of tissue stretch and strain with and without the application of the cervical pessary. Computer models were built from geometry primitives which were customized in dimension and orientation to replicate clinically relevant pelvic anatomic geometries using a method described in a previous work [72]. The FEA models were informed with previously published tissue material parameters from *ex-vivo* mechanical tests of the uterus, cervix, and fetal membrane. Simplifying assumptions for the boundary conditions, contact, and material properties of the abdomen and the pessary were made to offer a quantitative framework for the comparative analysis of the mechanical performance of the cervical pessary device in various positions.

4.2.1 Model Geometries

Model geometries and finite element meshes were built and generated with Trelis (v 15.1, csimsoft LLC) using a previously reported methodology. The baseline anatomic geometry was defined using literature values for average uterine and cervical dimensions of a 20-week singleton pregnancy. We chose the 20-week time point because the Arabin pessary is typically placed when a short cervix is indicated (around 18-22 weeks). Sources for each dimension used in the model are given in Table 13. The superior-inferior and transverse diameters at 20 weeks of gestation were found in a Gillespie 1950 study [73]. The anterior-posterior diameter was not reported so it was assumed to equal the transverse diameter. Single-parameter adjustments were then made to create models which can simulate clinically interesting geometries that are comparable to the predetermined baseline. The dimensions of each model of interest are listed in Table 13.

Table 13: Anatomic dimensions used in the baseline model and deviations from the baseline model.

Model	Uterine diameter[2]			Uterine wall thickness		Cervix		
Variation	Sup/Inf	Ant/Post[3]	Transverse[3]	Fundus[1]	LUS[1]	Length	Width	Angle

Baseline						30 mm	33 mm	90°
Pessary sizing	|	|	|	|	|	30 mm	33, 34, 35 mm	90°
Pessary position[4]	17.5 mm	14 mm	14 mm	10 mm	6 mm	30 mm	33 mm	90°
Short CX	|	|	|	|	|	25 mm	33 mm	90°
Cervical stiffness						30 mm	33 mm	90°
Angle						30 mm	33 mm	90-95°

[1] Degani et al. 1998 [74]. [2] Gillespie 1950 [73].
[3] Assumption of equal ant/post and transverse diameters of uterus at 20 weeks.
[4] The pessary was simulated at 5 mm, 10 mm, and 15 mm distances between the proximal end of the pessary and the exterior wall of the lower uterine segment.

4.2.2 Pessary Geometry

The Arabin cerclage pessary was also modeled in 3D in the Trelis program and is shown in Figure 35. The Arabin pessary is clinically available in several sizes, where inner diameter (ID) ranges from 32-35 mm, outer diameter (OD) ranges from 65 to 70 mm, and height (H) ranges from 17-30 mm. For our models, we chose to use a pessary with ID=32 mm, OD=65 mm, and H=25 mm. This pessary size was chosen according to the manufacturer's sizing recommendations [75] with the exception of the pessary height, which was increased from 17 to 25 mm (another common pessary height) so that it would be in contact with the vaginal floor of the numerical model. This was necessary to achieve numerical stability, though a shorter height pessary could be used in models with a shorter cervix. To alter the vertical position of the pessary in our model, we adjusted the height of the vaginal floor (and thus the position of the distal rim of the pessary) instead of changing the height of the pessary implant itself.

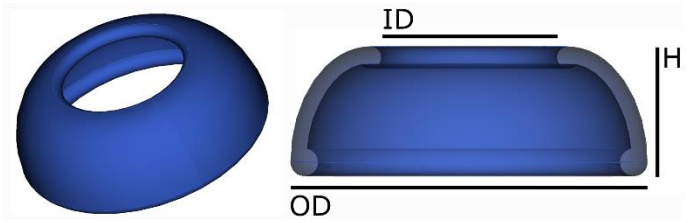

Figure 35: The cervical pessary is geometrically defined by its lower outer diameter (OD), its upper inner diameter (ID), and its height (H).

4.2.3 Mesh

The fetal membrane volume was meshed using hexahedral solid elements, and we meshed all other geometric volumes with linear tetrahedra. The mesh density can be adjusted, but information about typical meshes featured in this study is given in Table 6.

Table 14: Mesh properties for a typical model used in this study

	Total	Uterus	Cervix	Membrane	Abdomen	Pessary
Element Type	-	Tet	Tet	Hex	Tet	Tet
Element Count	143,200	26,000	42,000	9,600	32,600	33,000
Average Element Volume	-	19 mm^3	0.5-1.0 mm^3	0.8 mm^3	1050 mm^3	0.5 mm^3

4.2.4 Material Models

For the uterus and cervix, tissues were modeled as fiber composite materials featuring a neo-Hookean ground substance and a randomly oriented continuous fiber distribution. We modeled two variants of a cervical material, one representing a pregnant patient and one a nonpregnant patient. The details of the uterus and cervix models, including material properties corresponding to the definitions for "stiff" and "soft," are listed in the subsections that follow, along with detailed descriptions of the uterine material model and the fetal membrane material model.

4.2.4.1 "Soft" Cervical Material

The material properties of the cervix were found by fitting a randomly distributed fiber composite model with a neo-Hookean ground substance (described in Section 2.7.2) to uniaxial tension/compression force-displacement data from our previous work [1] according to the procedures in [26]. This material represents a pregnant cervix that has remodeled and gone through an initial softening phase but not the last ripening phase. These tissue samples were taken via caesarean hysterectomy before the labor process began (as described in [1]).

Table 15: Soft cervical material properties

Neo-Hookean ground substance

Property	E	ν	β	ξ	distribution
Value	0.00065	0.3	2	0.0017	spherical

4.2.4.2 "Stiff" Cervical Material

This model follows the same considerations as the soft material model, except that mechanical test data are from nonpregnant tissue specimens.

Table 16: Stiff cervical material properties

Neo-Hookean ground substance

Property	E	ν	β	ξ	distribution
Value	0.00065	0.3	3.12	0.077	spherical

4.2.4.3 Uterine Material Model

Stretch data from tensile tests of human uterine tissue [61] were employed to generate material properties for this fiber composite model of passive pregnant uteruine tissue.

Table 17: Uterine material properties

Neo-Hookean ground substance

Property	E	ν	β	ξ	distribution
Value	0.002	0.3	2.72	0.019	spherical

4.2.4.4 Amnion Material Model

The FM was modeled as an Ogden nonlinear material meshed with hexahedral elements (Trelis 15.1, csimsoft, LLC). In an Ogden material, the uncoupled hyperelastic strain energy function, Ψ, is given in terms of the eigenvalues of the deformation tensor:

$$\Psi = \sum_{i=1}^{N} \frac{c_i}{m_i^2}\left(\tilde{\lambda}_1^{m_i} + \tilde{\lambda}_2^{m_i} + \tilde{\lambda}_3^{m_i} - 3\right) + U(J), \tag{3}$$

where $\tilde{\lambda}_i^2$ are the eigenvalues of $\tilde{\boldsymbol{C}}$, c_i and m_i are material coefficients and N ranges from 1 to 6. The properties used were derived from data on biaxial tension tests of delivered FMs [2] and are reported in Table 10: Ogden Material Properties for the Amnion, below.

Table 18: Ogden Material Properties for the Amnion

(as specified in FEBio)

Property	k	$c1$	m1	c2	m2	c3	m3
Value	1000	0.85875	27.21	0.00368	27.21	0.75645	-16.64

4.2.4.5 Abdomen and Pessary Material Definitions

The abdominal material was a neo-Hookean material with modulus $E_y = 0.5$ kPa and Poisson's ratio $\nu = 0.4$. These highly compliant values were chosen to balance numerical stability with mechanical compliance so that the abdominal volume would act as a surrogate to soft internal organs. The pessary was defined to be a rigid body in these simulations to make the numerical solution more robust. This choice is justified by the fact that silicone rubber is orders of magnitude stiffer than the tissues involved in this simulation. All of these material models are discussed further in a 2016 study by our group [72].

4.2.5 Assembly of the Model

The geometries of the abdomen, uterus and cervix, fetal membrane, and pessary were assembled together and their interactions were defined to represent the natural conditions as closely as possible. The uterus and cervix are connected seamlessly and deform together along their boundary, consistent with histological knowledge of the tissue boundary of the pregnant uterus [76]. The fetal membrane was

connected to the inside of the uterus, but was allowed to slide freely over the top of the cervix at the internal *os*. These contact conditions are meant to replicate the condition of fetal fibronectin adhesion of the amnion with the decidua. The pessary was allowed to slide against the cervical wall, the vaginal fornix, and the lower vaginal wall, consistent with a lack of significant frictional interaction between the smooth silicon rubber material and the vagina and cervix.

4.2.6 Evaluation of the Mechanical Performance of the Cervical Pessary

The cervix serves as a mechanical barrier to delivery. It acts as a sphincter that must resist circumferential stresses resulting from the weight and size of the fetus and the associated tension in the uterine wall. There is also a normal stress acting on the top of the cervix caused by contact with the IUP-bearing fetal membrane. Lastly, connective tissues attached to the cervix and lower uterus contribute reaction forces that balance the fetal weight. In cases of PTB, these forces are present when premature cervical funneling (increasing circumferential stretch at the internal *os*) occurs. In particular, we hypothesize that excessive circumferential stress (and therefore stretch) at the site of the internal *os* may contribute to the early onset of cervical remodeling. Though the cervix predominantly comprises collagen, it contains smooth muscle cells capable of expressing chemical signals related to cervical tissue remodeling. Our group hypothesizes that cervical smooth muscle may be part of a biochemical chain reaction in which over distention occurs, triggering tissue remodeling, leading to softer cervical material properties, resulting in more stretch and a positive feedback loop. Preliminary results from work by our larger cohort indicate that cervical smooth muscle cells "secrete [matrix metalloproteinases], which are thought to be critical for cervical remodeling" [18]. We have therefore chosen to focus on the tensile and compressive loading of the internal *os* of the cervix, as it is the final common pathway to PTB [11], [12].

An idealized cervical pessary would assist the cervix by reducing the tissue stretch in the internal *os* without the side effects of excess loading and deformation of the stroma or other organs. We can see in our simulations and in MRI follow-up studies [64] that the pessary decreases the cervical diameter,

especially near its contact with the cervix, but the external loads and deformation in the cervix resulting from pessary use have not been quantified. Physically, there cannot be a reduction of tissue stretch at the internal *os* by a mechanical device without some type of applied loading; the question is the nature and magnitude of deformations resulting from such loading, and whether they are determined to contribute to tissue remodeling or not.

In our models, the internal os volume is defined to be a cylindrical volume extending from the inner uterine wall to 15mm into the cervix, with a diameter of 4 times the cervical canal diameter, aligned coaxially with the cervix. This standard volume allows comparisons of internal *os* loading to be performed. We used the same cervical canal diameter of 6 mm in all simulations presented in this work. First principal right stretch is our tensile deformation measure, while third principal stretch quantifies compression. For each comparison, we calculated how much of the internal *os* volume deformed in tension to a first principal right stretch level over 1.05 and 1.1. For compression, we considered the third principal right stretch thresholds of 0.95 and 0.90, where smaller values mean more compressive deformation. These four thresholds represent a 5% and 10% change in deformation due to tension and compression relative to the unloaded reference configuration. With these measurements, we can investigate the multifaceted loading effects, both positive and otherwise, caused by the cervical pessary.

4.2.7 Comparative Scenarios for Pessary Analysis

We calculated the change in force acting on the top of the internal *os* with and without a pessary in the model by integrating the stresses on the interior uterine surface in the region of the internal *os*. Then, we quantified the tensile and compressive stretch within the internal *os* for comparative scenarios involving the cervical pessary. Comparisons were carried out in order to study how the sizing and placement of the cervical pessary influences its mechanical interaction with the body. For each comparison, we hold all variables and properties constant except the parameter(s) of interest. With the exception of the pessary sizing study, all simulations used an IUP of 2.33 kPa, which represents a typical value at 40 weeks of

gestation [43]. IUP increases with gestational age, and a 40-week IUP represents a value on the high end of the expected physiological range while providing larger contrast between simulation results.

4.2.7.1 Load on Top of the Cervix With and Without Pessary

In order to investigate whether the pessary may influence or "reduce the load" on the cervix, the force acting on the top of the cervix near the internal *os* was evaluated for the sans-pessary and pessary cases, using the soft cervical material definition. To calculate the force on the cervix perpendicular to the cervical axis, stresses acting on the surface of the internal *os* where the membrane contacts the cervix were integrated.

4.2.7.2 With and Without Pessary for a Soft and a Stiff Cervix Model

Cervical stretch was compared with and without a pessary using the stiff and soft cervical material models. We measured the volume percentage of the internal *os* portion of the cervix exceeding threshold first principal right stretch of 1.05 and 1.10 under an IUP level of 2.33 kPa. Compressive stretches in the internal *os* beneath the 0.95 and 0.90 thresholds were also calculated.

4.2.7.3 Varying Cervical Outer Diameter with Constant Pessary Size

We then tested the effects of using a 32 mm ID pessary on three different cervical outer diameters: 33 mm, 34 mm, and 35 mm. Results are given for 1) compressive stretch levels in the cervix at the pessary contact point, and 2) the reduction in the internal cervical canal diameter at the level even with the top of the pessary (Table 20).

4.2.7.4 Pessary Position Relative to the Lower Uterine Segment

Next, we examined the effect of altering the insertion position of the pessary from the reference distance of 5 mm below the exterior of the uterine wall. We incremented pessary position twice more in 5 mm steps to a final distance of 15 mm below the uterus. For this comparison, we measured the volume percentage of the internal *os* segment of the cervix reaching third principal right stretches less than threshold

values of 0.95 and 0.90 (i.e. 5% and 10% compression). Tensile thresholds were also computed. We simulated an IUP level of 2.33 kPa, representing a characteristic value during the third trimester.

4.2.7.5 Induced Rotation of the Pessary

Finally, a 5-degree posterior rotation was induced in the pessary, resulting in a 2.5-degree posterior (counter-clockwise in the figure) rotation in the cervical canal (an increase to 92.5-degree uterocervical angle). In the simulation, the pessary was free to move except for in the rotational degrees of freedom, which were prescribed in this case. The same tensile and compressive stretch thresholds considered in the other comparisons were calculated for this simulation.

4.3 Results

Loading on the cervix changes when a pessary is present, as the pessary induces a squeezing and lifting of the cervix and lower uterine segment, respectively. Versus the previous free body diagram in section 1.3, Figure 36 below adds one additional force (labeled “Compression from pessary”) caused by the presence of the pessary and its squeezing action around the exterior cervix. Reaction pressures (Figure 35, “Reaction from surroundings”) are also affected by pessary use.

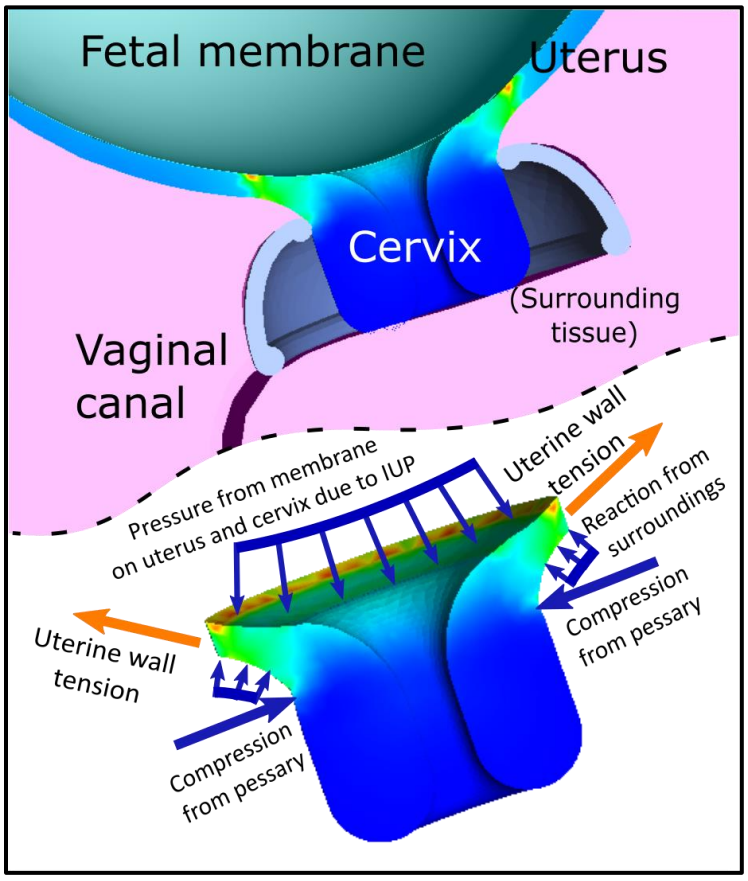

Figure 36: Free Body Diagram of the forces on the cervix when a pessary is present. Adding a pessary causes a compressive force on the exterior of the cervix.

4.3.1 Load on Top of the Cervix With and Without Pessary

In order to quantify the force on the cervix acting along its axis, "down" on the cervix from within the uterus, the component of pressure perpendicular to the internal cervical canal was integrated over the inner surface of the internal *os*. In our simulations, the presence of the pessary increased the force on the top of the cervix by about 50% from its original value (Table 19) at an intrauterine pressure of 2.33 kPa. It is not knowable from this simulation whether the increase of force is detrimental to an otherwise healthy pregnancy, but the perpendicular "force on the cervix" due to uterine contents is increased with the addition of a pessary.

Table 19: Force on the top of the cervix with and without a pessary in place. The force on the top of the cervix was increased by half with a pessary in place.

IUP = 2.33 kPa	*Force on top of cervix (N)*
soft, without a pessary	0.036
soft, with a pessary	0.054

4.3.2 Pessary Effect on Cervical Stretch Levels with a Stiff or Soft Cervix

Circumferential stretch levels in the internal os of the cervix were reduced in our model when the pessary was present. Internal *os* volume stretched over the 1.05 threshold in the "stiff" cervix variation was reduced from 29% to 27%, and from 45% to 39% in the "soft" cervix model. Although the reduction occurred in both the stiff and soft cervical material cases, it was three times more prominent for the model employing soft cervical material properties (Figure 37). The soft cervix model was the only one to exhibit stretches over 1.1 with or without a pessary, though the pessary reduced the 6% portion of the internal *os* over that threshold by 1/3 to 4%. On the other hand, the pessary caused more compression in the internal os, doubling the portion of internal os volume beneath the 0.90 stretch threshold from 3% to 6% for the soft cervix case (Figure 38). A similar but less pronounced trend occurred in the "stiff" cervix model.

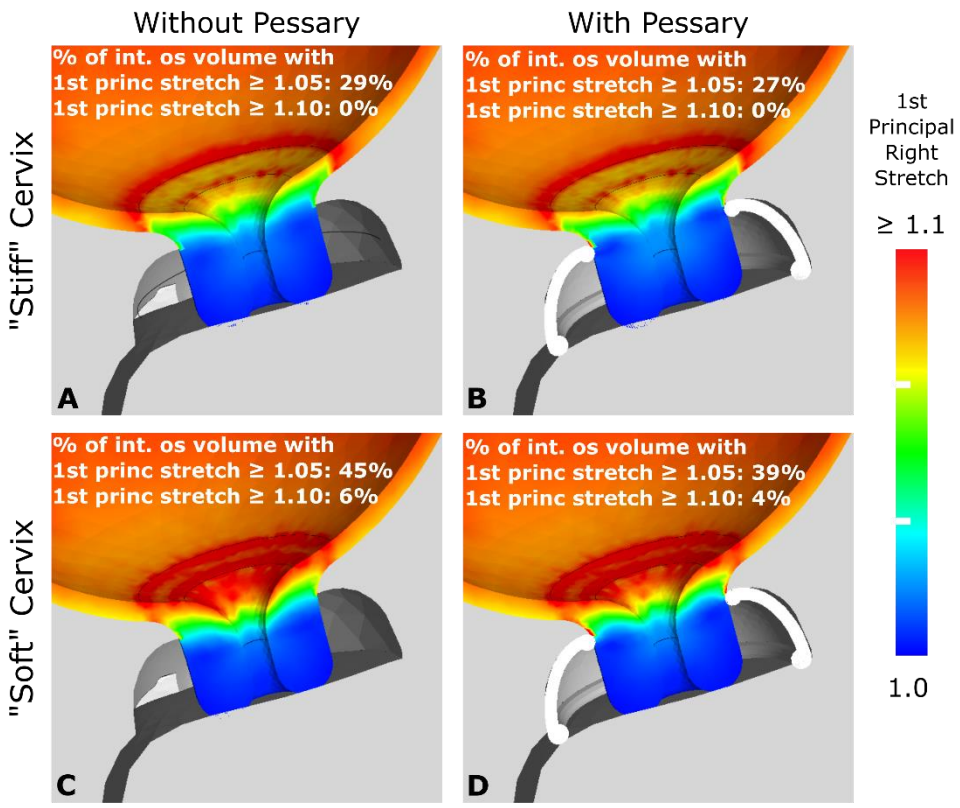

Figure 37: First principal right stretch in the cervix with and without a pessary at an IUP of 2.33 kPa. The pessary in our simulation reduced circumferential stretch levels in the internal *os* of the cervix when it was present in the model. The effect was more prominent for the model using soft material properties in the cervix.

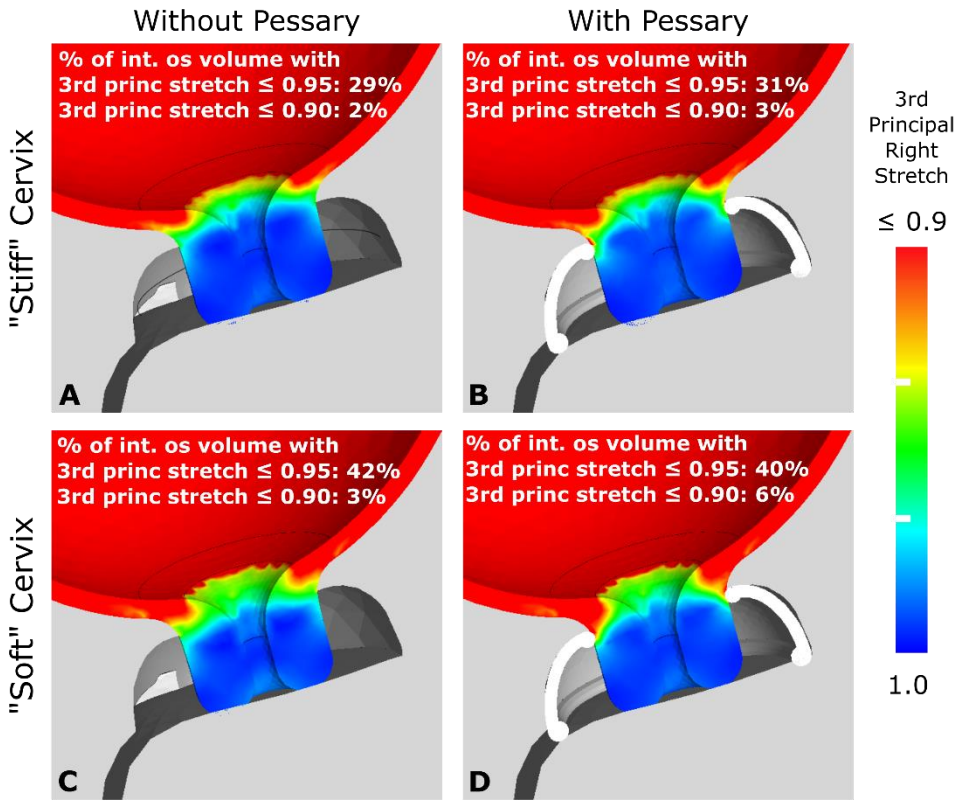

Figure 38: Third principal right stretch in the cervix with and without a pessary at an IUP of 2.33 kPa. In our simulation, the pessary resulted in the portion of internal *os* volume beneath the 0.90 stretch threshold to change from 3% to 6%. (The pessary caused more compression in the internal *os*.)

4.3.3 Cervical Stretch Resulting from Pessary Under-sizing

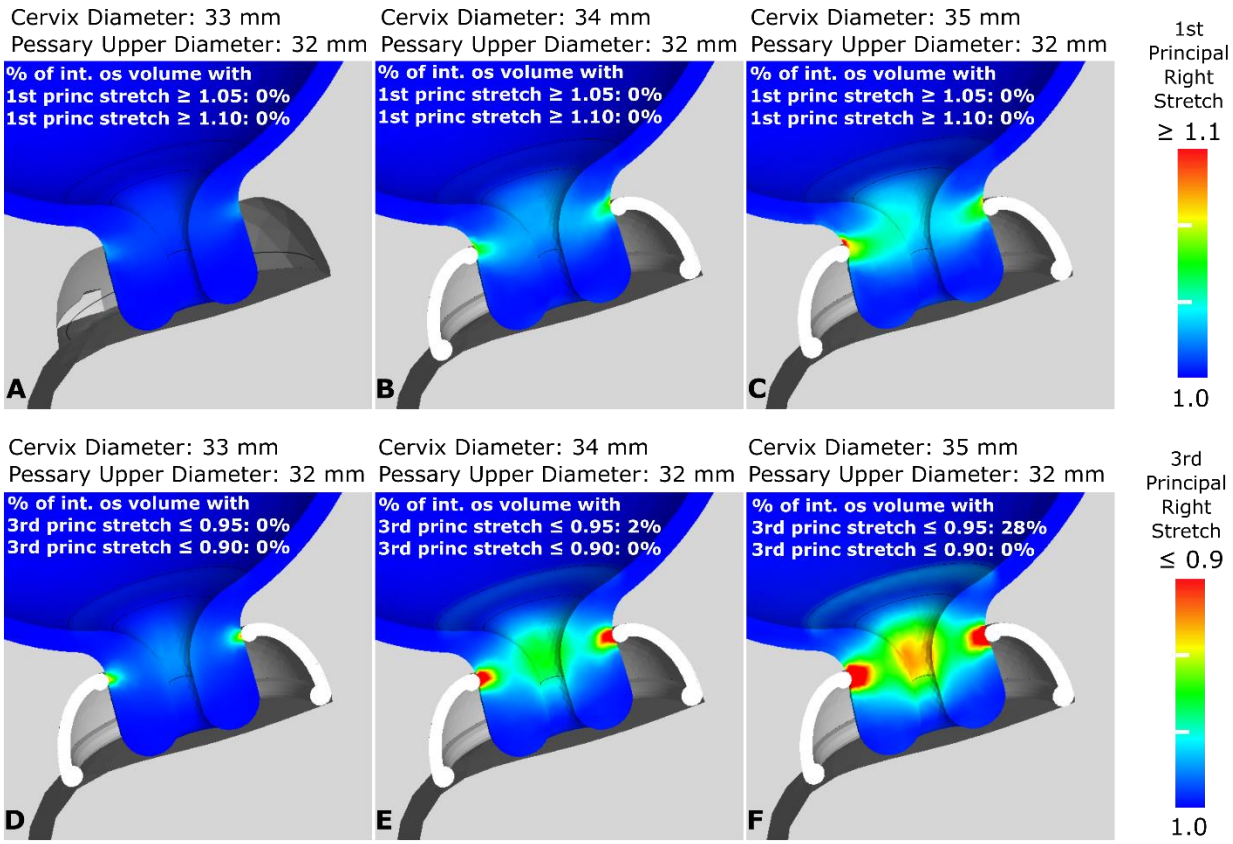

Figure 39: 1st principal right stretch represents tensile stretching due to the pessary while third principal right stretch describes compressive stretch. A pessary with an inner diameter smaller than the cervical outer diameter can cause significant compressive stretches within the cervical stroma under the ring-shaped area where it touches the cervix. The degree of this compression is sensitive to the amount of under-sizing. No IUP was prescribed in these comparisons in order to isolate the undersizing-induced loading.

Figure 39 shows under-sizing of the inner diameter of the pessary to less than the cervical diameter. Compressive stretches were present on the cervix exterior, under the contact area with the pessary. The compression pattern propagates inward toward the cervical canal resulting in a reduction of the cervical canal diameter. There was no IUP loading included in this simulation so that under-sizing effects could be isolated.

Table 20: Impact of pessary under-sizing, in terms of the stretch levels underneath the pessary contact area. A tighter-fitting pessary (in this case, simulated by increasing the cervix size) results in a greater closing effect and more significant compressive stretches on the exterior of the cervix.

Cervix OD		

(Pessary ID: 32 mm)	Compressive stretch level in the cervix where the pessary is in contact	Reduction in cervical canal diameter
33 mm	~0.92	0%
34 mm	~0.85	5%
35 mm	~0.82	9%

Under-sizing by 1 mm had a minimal effect on cervical canal diameter while causing approximately 8% compressive strains at the contact surface between the cervix and the pessary (Table 20). On the other hand, when under-sizing by 3 mm, there was a 9% reduction in the cervical canal diameter with more than an 18% compressive strain observed at the contact point. The highest compressive stretches occurred for the largest cervix size of 35 mm (and therefore the greatest degree of pessary under-sizing) with 28% of the internal *os* volume having third principal right stretch levels under the 0.95 threshold, but no portion of the internal *os* experienced a compressive stretch beyond the threshold of 0.90.

4.3.4 Cervical Stretch with Changes in Pessary Position

Our simulations show that the pessary has the greatest tensile deformation shielding effect when it is positioned near the uterus around the upper portion of the cervix (Figure 40). As the pessary is moved further away from the internal *os*, the shielding effect is reduced. The same holds true for compressive stretch shielding within the internal *os* volume. Outside of the internal os, in the outer portion of the cervix, we can observe that third principal right stretch levels on the order of 0.95 extend from the proximal end of the cervix down until the edge of the pessary lip. This is likely due to the compression of the abdominal volume under the uterus, adding compressive loading against the outer cervix above the pessary.

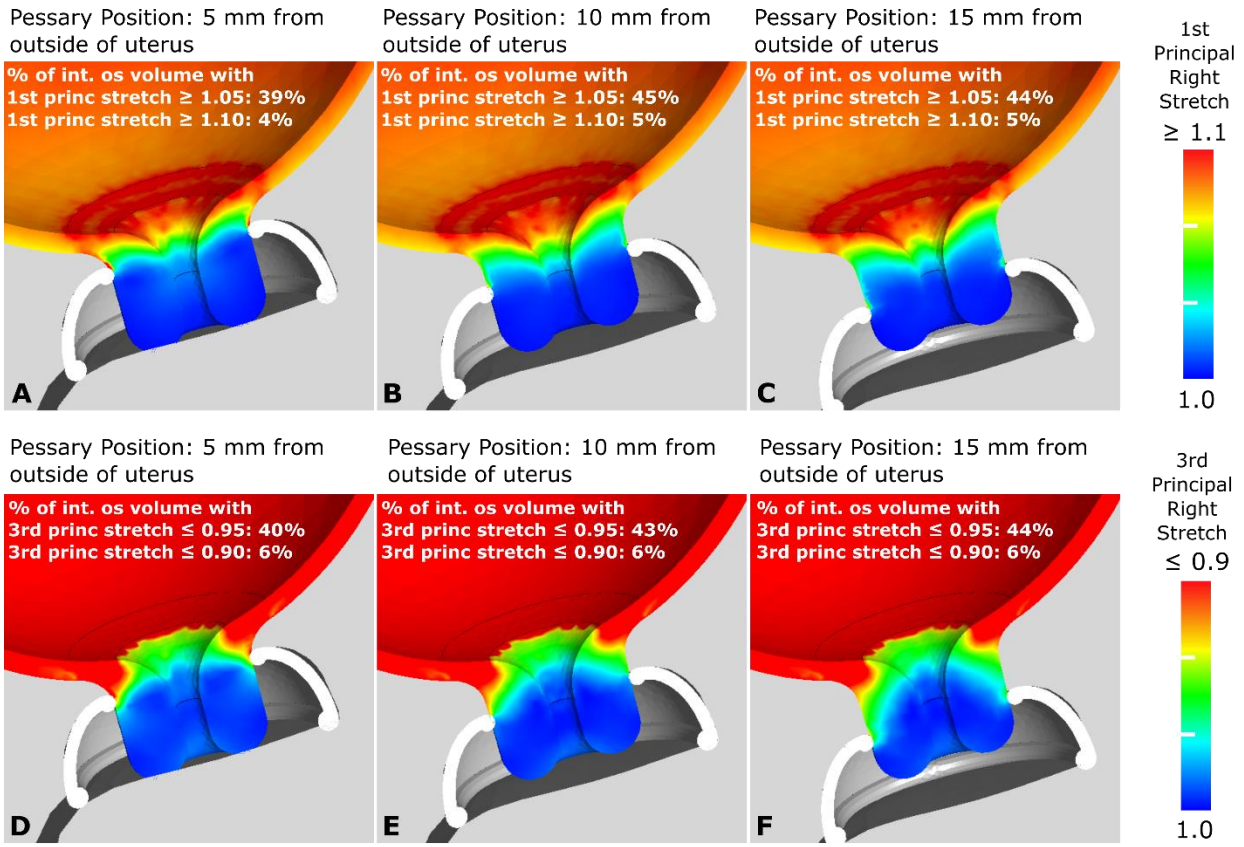

Figure 40: Effect of cervical pessary position on strain patterns in the cervix, for a soft cervix material definition. The highest pessary location provided the largest reduction in first principal strains in the internal *os* region. The IUP was set to 2.33 kPa for these tests.

4.3.5 Effect of Inducing a Rotation on the Pessary to Change Cervical Angle

The stretch results are visualized in Figure 41, below. A five-degree CCW pessary rotation resulted in a 2% increase in the internal *os* volume fraction with stretches exceeding both the 1.05 and 1.1 thresholds. More significant increases occurred for third principal right stretch, with 3% or 4% increases in internal os volume reaching levels below the 0.95 and 0.90 compression thresholds. However, the rotation action caused large spikes in strain at the exterior cervix where the pessary impinged on it. Third right stretch levels there reached as low as 0.6 (a 40% compression) from 0.85 with no rotation. Additionally, peak tensile stretches at that location reached as high as 1.7, far over our comparative threshold for the internal *os*, and significantly higher than the no-rotation peak of 1.25.

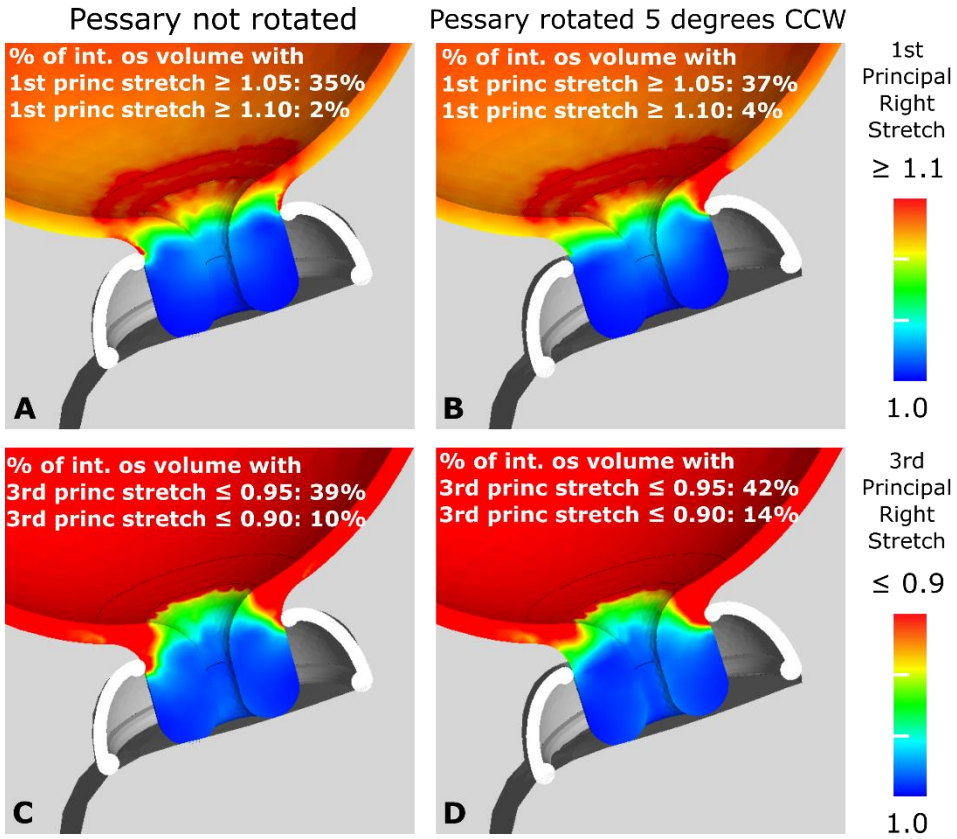

Figure 41: A five-degree pessary rotation causes first principal stretch in the exterior cervix to reach levels greater than 1.7, and compressive third principal stretches to reach 0.6, while stretches in the internal os change less.

4.4 Discussion

Our results show that the pessary is capable of reducing the inner cervical canal diameter by geometrically constraining the cervix from the exterior. This effect is coupled with increased strain and stress levels in the exterior lower uterine segment and in the cervix near the area of contact with the pessary. The pessary mechanically induces a reduction in the opening of the cervical canal by compressing the outside of the cervix. This forced closure results in a relative reduction of the tissue stretch at the internal *os* coupled with increased compressive loading on the outer cervix. The relative reduction of cervical internal *os* stretch decreases with stiffer cervical material properties. Simply, a soft cervix is easier to close

with a pessary, and common sense dictates that a smaller pessary would close a cervix more than a larger pessary. However, the degree of cervical canal closure is not the only important factor.

We know that cervical tissue reacts to induced strains, and strains could therefore contribute to a biochemical remodeling process. Previous studies conducted by our group [18] found increased matrix metalloproteinase (MMP) secretion in cervical smooth muscle cells after they were subjected to 15% strain. MMPs contribute to collagen degradation in mice [77], and they are present at higher levels in human cervix during the ripening phase [78].

There is a theoretical optimal pessary size and geometry that would maximize the cervical closing effect while minimizing any negative impact from forces exerted on the exterior cervix. The strain levels reported in our simulation results are therefore on the order of strains that could make a significant difference in chemical signaling related to enzymatic remodeling of the cervix. Further, these large differences in strain highlight the importance of including pessary size analysis in any future clinical trials.

Our results show that the ability of the pessary to shield the internal *os* from added strains under increased IUP levels depends on the proximity of the pessary to the internal *os*. Put simply, the higher the pessary is placed on the cervix, the better it can reduce strains in the internal *os*. Another complicating factor is that the presence of a pessary appears to significantly *increase* the compressive load that the membrane transfers to the top of the cervix. This important result reminds us that when discussing loading in the cervix, it is important to be specific about the type of loading (tensile, compressive) and its location (internal *os*, exterior cervix), and its orientation (axial, circumferential).

Finally, there is no evidence from our simulations that changing the uterocervical angle with a pessary can reduce the mechanical loads on the cervix. Cervical angle is a proposed biomarker to predict PTB risk [79]. Indeed, a wide uterocervical angle may be indicative of a change in tissue properties,

however, our simulations show that artificially altering the angle of the cervix with a pessary may cause significant (> 0.18) localized strains near the point of contact between the pessary and the exterior cervix.

4.5 Conclusion

With these simulations, we have evaluated the pessary's mechanical influence on the pregnant pelvic environment. Our results found that the therapeutic effect of closing the cervical canal is accompanied by potentially unwanted compressive strains on the cervix's exterior. It is unknown whether this redistribution of mechanical loading caused by the pessary is clinically beneficial or if the added loading to the exterior cervix may exacerbate early cervical remodeling.

Our simulations also highlight the opportunity that modern simulation capabilities and computing resources enable in the context of pregnancy biomechanics. The cervical pessary was originally designed without the aid of finite element modeling techniques and the material constitutive models now available. With these tools, it is possible to pose the (re)design of a biomechanical device like the cervical pessary as an optimization to achieve the desired effect of cervical closing, while minimizing any undesired loading.

There are many unknowns remaining in the context of the pessary and preterm birth biomechanics. With conflicting clinical trial data in the literature claiming pessary efficacy and inefficacy and an incomplete understanding of the in-situ mechanics of the very device being studied, there is a strong need for further investigation of cervical biomechanical interactions involving the pessary. As our group and others continue to learn more about the biochemical cascade of cervical remodeling during pregnancy, we can incorporate that knowledge into future versions of these simulations to help understand the problem more fully. We will then be able to address current unknowns like the level of allowable external forces on the pregnant cervix, and the optimal design for mechanical-device-based PTB interventions.

4.6 Related Publications and Abstracts

1. Abstract and Poster: Michael Fernandez, Andrea Westervelt, Joy Vink, Michael House, Chia-Ling Nhan-Chang, Miaoying Fan, Ronald Wapner, Michal A Elovitz, Kristin Myers. Biomechanical Computer Simulation of the Arabin Cervical Pessary. SRI 2016.

5 Diffusion and Permeability in Hydrogel Phantoms and Cervical Tissue

5.1 Motivation

The gold standard for a measurement of a mechanical property in biomechanics would be one measured *in-vivo*, noninvasively, accurately, and it would be physically meaningful. Thanks to advanced MRI techniques, we may be able to achieve most of these objectives.

An MRI modality called Diffusion Weighted Imaging (DWI) popularized and developed by LeBihan and others [80]–[83] holds unique promise for studying mechanical properties of hydrated tissues *in-vivo*. DWI is able to quantitatively estimate the self-diffusion of water within a hydrated tissue. The relationship between water self-diffusivity and the mechanical property of permeability is still an open question, though in previous work (included in section 5.3) our group has found a well-behaved relationship in hydrogels.

To establish a relationship between the apparent diffusion coefficient (ADC) as measured by DWI and the mechanical property of permeability could be of great usefulness across biomechanics, enabling the probing of mechanical properties in a completely safe manner. These techniques would be of particular value for emerging patient-specific computer modeling and intervention strategies.

5.2 Permeability of Human Cervical Tissue

The mechanical integrity of the uterine cervix is critical for a pregnancy to successfully reach full term. It must be strong to retain the fetus throughout gestation and then undergo a remodeling and softening process before labor for delivery of the fetus. It is believed that cervical insufficiency (CI), a condition in pregnancy resulting in preterm birth (PTB), is related to a cervix with compromised mechanical strength which cannot resist deformation caused by external forces generated by the growing fetus. Such PTBs are responsible for infant developmental problems and in severe cases infant mortality. To understand the etiologies of CI, our

overall research goal is to investigate the mechanical behavior of the cervix. Permeability is a mechanical property of hydrated collagenous tissues that dictates the time-dependent response of the tissue to mechanical loading. The goal of this study was to design a novel soft tissue permeability testing device and to present direct hydraulic permeability measurements of excised nonpregnant (NP) and pregnant (PG) human cervical tissue from women with different obstetric histories. Results of hydraulic permeability testing indicate repeatability for specimens from single patients, with an order of magnitude separating the NP and PG group means ($2.1 \pm 1.4\times10^{-14}$ and $3.2 \pm 4.8\times10^{-13}\, m^4/N \cdot s$, respectively), and large variability within the NP and PG sample groups. Differences were found between samples with similar obstetric histories, supporting the view that medical history may not be a good predictor of permeability (and therefore mechanical behavior) and highlighting the need for patient-specific measurements of cervical mechanical properties. The permeability measurements from this study will be used in future work to model the constitutive material behavior of cervical tissue and to develop in vivo diagnostic tools to stage the progression of labor.

5.2.1 Introduction

5.2.1.1 Cervical Insufficiency

Preterm birth (PTB) impacts the lives of more than half a million infants each year in the United States, with a national PTB rate of 12% [3], [5], [84]. Cervical insufficiency (CI), a condition in pregnancy when the cervix prematurely shortens and dilates, is a leading known contributor to our high PTB rate. Infants surviving these PTBs are at a significant risk for long-term morbidities including neurologic, respiratory, cardiovascular, and gastrointestinal complications [3], [85], [86]. The pathophysiology of CI is hypothesized to be multifactorial, with pregnancy outcomes depending on a combination of congenital, anatomical, obstetric, epidemiological, and biochemical factors [87]. These multiple factors lead to a common feature in CI, a structurally weak and excessively compliant cervix that is unable to remain closed to support the fetus. The lack of quantifiable and comparable outcome measures to assess the structural and material strength of the cervix limits the ability to discern these etiologies, to stage the progression of labor, and to identify and manage high-risk CI patients. In current clinical practice, the diagnosis of CI relies on many qualitative factors including a poor obstetric history, characterized by a history of PTBs preceded by painless cervical dilation or shortening, or a dilated or short sonographic cervix, typically less than 25 mm in the current pregnancy. More recent in vivo imaging and endoscopic tools have advanced the understanding of cervical remodeling during pregnancy. Such tools include ultrasound elastography [88], [89] and acoustic attenuation [90]–[93]. There is agreement that a decrease in cervical strength is associated with both normal maturation and abnormal pathological conditions, and ongoing research seeks to develop diagnostic methods to identify women at risk for premature cervical remodeling. A valuable contribution to this area of research would be a quantitative measure of cervical strength that is based on intrinsic tissue material and extracellular matrix (ECM) properties. The overall goal of our research is to characterize the material properties of the cervix during normal and abnormal cervical remodeling processes related to CI. We aim to establish the framework to evaluate the physiologic state of the cervix and to provide a

quantitative correlation between cervical ECM structure and cervical material properties. In this study, we report direct measurements of cervical permeability, a tissue material property, from ex vivo nonpregnant (NP) and pregnant (PG) hysterectomy specimens. These measurements will serve as a basis to model the time-dependent constitutive behavior of NP and PG cervical tissue.

5.2.1.2 Cervical Tissue Properties

The cervix serves a crucial mechanical role in pregnancy. It must resist complex tension and compression forces to retain the fetus and it must then remodel drastically to allow the fetus passage at time of delivery [11]. The ECM of its collagen-dense stromal core provides the cervix with its overall material strength. Human cervical tissue is 75% and 80% hydrated in its NP and PG state, respectively [94]–[97]. Its ECM consists of a crosslinked type I and III collagen network surrounded by a viscous ground substance of interstitial fluid, proteoglycans (PGs), and glycosaminoglycans (GAGs). The GAGs are present either in the form of PGs (e.g. dermatan sulfate in decorin), or they are embedded in the matrix without a core protein (e.g. hyaluronic acid). The ECM is interlaced with a small fraction of elastin, smooth muscle cells, and cervical fibroblasts, with the cells modulating the ECM constituents during the nonpregnant state and cervical maturation [43], [97]–[100]. Cervical tissue remodeling during pregnancy is facilitated by a progressive shift in the cervical ECM [76], [94], [100]–[108]. This remodeling process has been studied in accessible rodent tissue. Studies by Word et al. [106], Mahendroo [109] and Akgul et al. [110] recently showed that the mouse cervix remodels progressively during pregnancy by using a gestation-timed mouse population. In the mouse model, cervical remodeling is characterized by four distinct phases: softening, ripening, dilation, and repair. Softening starts on approximately day 12 of a 19 day gestation, and is characterized by a gradual increase in collagen reorganization, tissue growth, and vascularity. Ripening, which may be initiated weeks or days before dilation in humans and hours before dilation in mice [107], is characterized by a drastic hydration increase. This fluid increase is facilitated by an increase in hyaluronic acid content [110], an increase in fixed charge density [111], and a turnover of mature crosslinked collagen

fibrils to immature less crosslinked fibrils [100]. After ripening, cervical dilation occurs with a decrease in collagen concentration, an increase in vascularity, and an increase in inflammatory processes. After delivery, the cervix repairs itself with the reversal of these processes [106], [107]. It is unknown if these distinct remodeling phases are present during human cervical remodeling, and the associated mechanical property changes related to this active collagen turnover remain to be determined. We postulate that, due to loosening of the collagen network during pregnancy, the permeability of PG tissue will be higher than the permeability of NP tissue. We further postulate that the permeability of NP tissue taken from women with previous vaginal deliveries will be higher than that of NP tissue from women with no previous vaginal deliveries. Direct permeability studies have been done on similar load-bearing collagenous tissue in the context of describing cartilage and intervertebral disc tissue as a biphasic (i.e. poroelastic) material [112]–[114]. In a similar way, we plan to use our direct permeability measurements and data from corresponding uniaxial and indentation testing to build a constitutive framework for human cervical tissue that includes a poroelastic contribution. We are also currently developing diagnostic tools to stage the progression of cervical remodeling based on our cervical permeability measurements and diffusion-based magnetic resonance image signals.

5.2.1.3 Constitutive Material Considerations

There are limited studies on human whole cervix because of the difficulty in accessing fresh tissue, especially from PG women and patients with diagnosed CI. To build our understanding of the relationship between ECM changes and corresponding material characteristics of cervical stroma, our group studies ex vivo whole cervical tissue taken from hysterectomy patients. *Ex vivo* studies provide crucial mechanical and biochemical testing data to determine cervical ECM-material property relationships for a range of women with varying ages and obstetric histories. Our previous studies have concentrated on uniaxial compression and tension stress-relaxation tests of cervical tissue specimens [1], [32]. We have reported that cervical tissue has a complex nonlinear, time dependent and anisotropic material behavior. We have also

found that this material response is dependent on the obstetric background of the tissue, where PG tissue is considerably less resistant to deformation than NP tissue and NP tissue from women with previous vaginal deliveries is less resistant to deformation than NP tissue from women who have never had a vaginal delivery. The time-dependent stress response from our previous uniaxial tests [1], [32] could be attributed to the poroelastic draining of pressurized interstitial fluid [115], [116] and/or the viscoelastic unraveling of collagen fiber entanglements. In our efforts to build a constitutive material model for human cervical tissue, we aim to isolate and characterize the poroelastic contribution to the time dependent material response in the study presented here. To this end, we developed a mechanical test to directly measure tissue permeability based on Darcy's law [117]. We report here the design of a permeability testing fixture and the results of this mechanical test on multiple cervical tissue samples taken from NP and PG hysterectomy patients.

5.2.2 Methods

5.2.2.1 Permeation Apparatus Design

The unidirectional flow rate of a fluid q through a porous continuum depends on the pressure gradient ∇P, the dynamic viscosity of the fluid μ_{fluid}, and the Darcy permeability of the medium κ, defining Darcy's law $q = (-\kappa \,/\, \mu_{fluid})\nabla P$ [117]. On the basis of this law, we developed a custom experimental rig to measure the fluid flow q through a confined tissue specimen with a known pressure difference ΔP and height $h_{specimen}$ (Figure 42), where $\nabla P = \Delta P / h_{specimen}$. From these values, we calculate the hydraulic permeability k of our tested specimens according to Darcy's law, where k is defined as κ/μ_{fluid}. Throughout this paper, k will refer to the hydraulic permeability measured in $m^4/(N \cdot s)$. An explanation of the difference between intrinsic permeability and the measured hydraulic permeability k is given in the Discussion section. The constant pressure permeability configuration in this paper was chosen over a prescribed flow rate configuration because it reaches a steady state flow condition more quickly. The analytical solution for transient permeation in a biphasic material may be derived using a similar analysis

as for confined compression. It can be shown that the time constant for transient permeation depends on the testing configuration, in analogy to time constants for confined compression creep versus stress relaxation: when permeation is performed using a prescribed fluid velocity, the time constant to reach steady state is $\tau = 4h^2/(\pi^2 H_A k_0)$ (similar to confined compression creep); when prescribing a fluid pressure upstream, the time constant is $\tau = h^2/(\pi^2 H_A k_0)$ (similar to confined compression stress-relaxation).

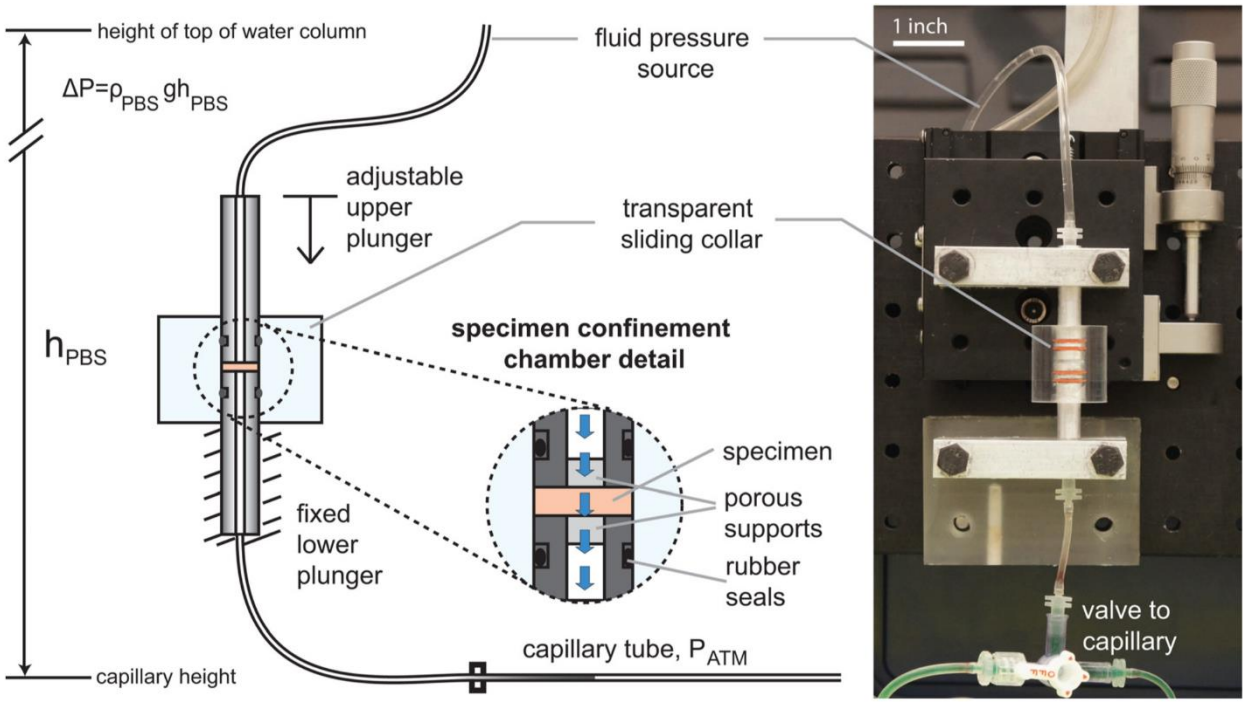

Figure 42: Permeability experiment overview. A soft tissue specimen is placed between two porous supports while a constant fluid pressure gradient is applied. Flow is measured downstream using time-lapse images of dye as it is displaced inside a capillary tube.

The custom-made fixture (Figure 42) comprised three primary components: a fluid pressure source, a specimen confinement chamber, and a flow measurement system. A column of phosphate buffered saline (PBS) of height h_{PBS}, as measured from the top free surface to the open capillary tube, provided a constant upstream fluid pressure source ($\mu_{PBS} = 0.001\, Pa \cdot s,\ \rho_{PBS} = 1000\, kg/m^3$). The specimen chamber consisted of an adjustable upper and fixed lower plunger that formed a mechanical seal around the outer specimen edges. The top and bottom cylindrical plungers were machined out of 6061 aluminum at a diameter of 8 mm, with a 4.05 ± 0.05 mm diameter bore to hold porous polymer supports (Porex X-4898,

pore size: 15–45 μm). The porous polymer plugs prevented tissue specimens from deforming outside the specimen confinement chamber but allowed liquid to pass freely into and out of the specimen. To prescribe the distance between the two plungers (e.g. the specimen height), the adjustable upper plunger was mounted on a linear translating stage (Newport M-423) with an attached Vernier micrometer (25 mm travel, 23 lb load capacity, Newport SM-25). The sample was confined in-place between the upper and lower plunger with a transparent press-fit collar, and the upstream flow was forced through a 4 mm diameter flow path in the center of the specimen. We confirmed this flow path by injecting dye upstream of trial specimens and observing well-defined central flow patterns. In addition, leaking edges were easily detectable because the resulting downstream flow rates were typically hundreds of times higher than adjacent readings. To quantify downstream flow rates during testing, we used time-lapse photography of dye in a 10 cm long, 0.86 mm diameter capillary tube connected to the output of the permeation chamber. Timed images were taken with a Canon T1i digital SLR camera with EOS image sequence acquisition software. An in-frame precision ruler was used to calibrate the pixel scale for each test. This calibration varied between 10 and 14 pixels per mm, depending on the lens zoom setting during a given test. Using IMAGEJ, all frames were converted to binary format according to brightness at each point, and a de-speckling filter with a radius of 6 pixels was utilized in MATLAB to reduce noise. Dye in the tube was converted to black pixels and the background to white pixels. The images were further processed in MATLAB to produce displacement information at representative time points. Using the steady-state flow rate, the apparent hydraulic permeability k was calculated with Darcy's law. The design presented here is flexible enough to measure values of hydraulic permeability from 10^{-11} to 10^{-17} $m^4/(N \cdot s)$.

5.2.2.2 Tissue Samples

Whole cervix specimens were collected using an IRB approved protocol from consented patients at the Columbia University Medical Center. A total of 30 and 17 samples from 6 NP and 6 PG cervices were tested, respectively. Whole cervix specimens were acquired from hysterectomy patients immediately

after surgical removal (obstetric histories of the tested specimens are reported in Table 21). Cesareans on PG patients were all performed prior to the onset of labor. The cervix was cut from the uterus and then sectioned perpendicular to the inner canal into four axial 4 mm thick slices using a custom-built cervical slicer (details of slicer device are given in Ref. [1]).

Table 21: Specimen information. G stands for gravida, equivalent to the total number of pregnancies. TPAL stands for term, preterm, aborted, and living deliveries, corresponding, respectively, to each of the four digits. CS = cesarean section, VTOP= voluntary termination, SAB = spontaneous abortion (miscarriage), VD = vaginal delivery, FT = full term. For each patient, there is a corresponding point on Figure 3 positioned at the mean value of the associated permeability measurements. *Patient NP5's records were ambiguous. There was one full term birth (not known if vaginal or caesarian) and one abortion (not known if voluntary or spontaneous).

Patient	Age	G	TPAL Parity	Obstetric History	Surgical Indication	Weeks Gestation	Specimens Tested $n_{specimens}$
NP1	36	0	0000	No prior pregnancies.	endometriosis	–	2
NP2	41	4	2022	2 FT CS, 1 VTOP, 1 SAB	uterine fibroids	–	4
NP3	44	5	2032	2 FT VD, 1 VTOP, 2 SAB	pelvic pain	–	4
NP4	44	2	2002	1 FT VD, 1 FT CS	uterine fibroids	–	1
NP5	46	2	1011	1 FT *	fibroids	–	15
NP6	48	4	4004	4 FT VD	menorrhagia	–	4
PG1	24	6	4014	4 FT CS, 1 SAB	suspected accreta	23	1
PG2	30	3	1011	1 FT CS, 1 VTOP	accreta	34 4/7	4
PG3	34	2	1001	1 FT CS	suspected percreta	35 3/7	2
PG4	35	3	2002	1 FT VD, 1 FT CS	fibroids, dysmenorrhea, menorrhagia	36	5
PG5	38	3	2002	2 FT CS	suspected accreta	35 4/7	4
PG6	40	3	2002	2 FT CS	suspected percreta	34	1

Each slice was labeled according to position from the internal *os*. Slices were stored flat at -80 °C until testing. Twelve hours before planned mechanical tests, slices were equilibrated in PBS at 4 °C and then tested with a nondestructive indentation mechanical testing routine [118]. After indentation testing, 8 mm diameter biopsies were taken in the mid stromal region, with the cut direction parallel to the inner canal. Samples were then microtomed to 1 mm thick cylindrical disks. After another equilibration in PBS (approximately 30 min for thin specimens), each sample was placed in the permeation chamber such that the direction of flow was parallel to the inner canal. Once the specimen was seated within the chamber, a pressure head ΔP of 10 cm of PBS (9.79 kPa) was applied and the flow rate downstream was measured after reaching a steady state (see Discussion section for steady-state analysis). Hydraulic permeability k was then calculated according to Darcy's law.

5.2.2.3 Apparatus Validation

The apparatus was used to test the permeability of Acrylamide/Bis-Acrylamide gels (19:1 ratio) of 6% to 30% concentrations in 3% increments (v/v) (SigmaAldrich no. A9926). The resulting permeability data were fit to an exponential regression which achieved an R^2 value of 0.986 after gel wet/dry weight concentration corrections were made (R^2 before corrections was 0.982). Acrylamide gel properties are sensitive to protocol, environment, and mixing ratios, but the permeability measurements we observed in the 20% concentration range were on the same order (about double) the permeability estimated for similar gels in Ref. [119] using microindentation techniques. Although 3% is just outside our experimental range for polyacrylamide, an extrapolation from our concentration-corrected exponential regression curve estimates a permeability value on the same order, but with a factor of 0.27 compared to measurements by Grattoni et al. [120] at 3% concentration. Our measurements fall in between these two sources' estimates, with some of the variation attributable to differences in preparation.

5.2.2.4 Measurement Uncertainty

The total error for permeability measurements was calculated as the root of the sum of the squares of the camera distance measurement uncertainty, the specimen height uncertainty, the water column (pressure source) uncertainty, and the dimensional variability of the custom machined parts of the experimental rig which affect the flow path diameter. The numerical computation error is negligible in the permeability calculation. The uncertainty in length measurement using the Canon T1i digital camera from a fixed distance of 38 cm (lens-to-capillary) was measured to be less than 0.4 mm per 100 mm using a precision calibration ruler positioned at representative locations in-frame. The dye progression was tracked for a minimum of 2 cm after steady state flow was confirmed visually (by inspecting data mid-test) and/or after four time constants worth of time had elapsed. This translates to a maximum error of 5% in velocity during the steady state observation period (this error was usually much smaller because the dye was normally tracked longer at steady state). Computer-assisted visual fitting of a straight line was used to

characterize the slope at steady state. Trial fittings were compared to least-squares regressions and fell within 2% error. The visual fit method was preferred due to the ability of a human operator to easily distinguish between actual data points and data points caused by image noise. The uncertainty in specimen height is 0.05 mm, or 5% of the typical specimen height. The uncertainty in the flow path diameter was 0.05 mm which translates to a flow area uncertainty of 2.5% for an average diameter of 4.05 mm. The root of the sum of squared uncertainties results in a 6% uncertainty for a given computed permeability value.

5.2.2.5 Results

Figure 43 shows a typical downstream dye displacement versus time for a PG specimen (specimen PG4). For human cervical tissue permeation experiments, it typically took three or more hours to reach a steady state flow condition, depending on the tissue's solid modulus, exact thickness, and hydraulic permeability.

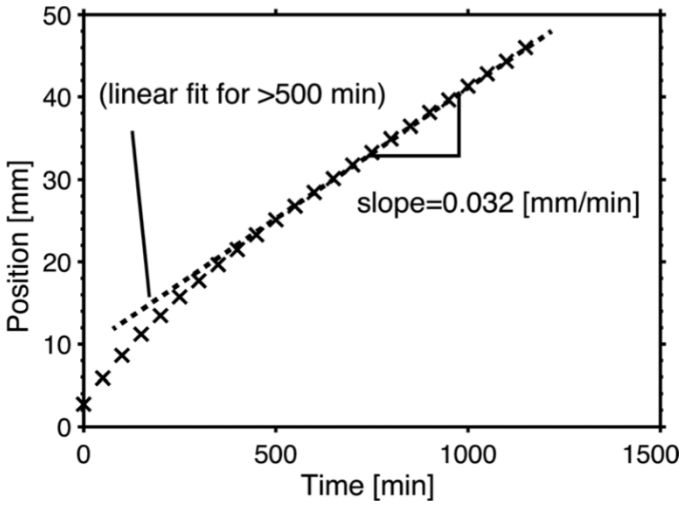

Figure 43: A typical plot of dye progression over the course of a cervical tissue permeation test for a PG specimen. The visible straightening of the curve signifies steady-state conditions.

We experimentally observed the time of flow rate stabilization in the order of magnitude predicted by an analytical solution of a poroelastic material with estimates for the tissue solid modulus from our previous uniaxial compression tests (see Discussion, section 4.4).

The mean hydraulic permeability k for NP tissue was $2.1\times10^{-14}\,m^4/N\cdot s$ (range: $3.2\times10^{-15}-4.6\times10^{-14}\,m^4/N\cdot s$), and the average k for PG tissue was $3.2\times10^{-13}\,m^4/N\cdot s$ (range: $3.2\times10^{-14}-1.4\times10^{-12}\,m^4/N\cdot s$). Figure 44 reports the average hydraulic permeability k for each whole cervix according to age. Overall, the PG tissue tested in this study was more permeable than the NP tissue. However, an age-matched comparison cannot be made because the patient ages for NP tissue (NP age range: 36–48) was higher than the PG tissue (PG age range: 24–40). This difference in permeability could be attributed to an age effect or a remodeling effect.

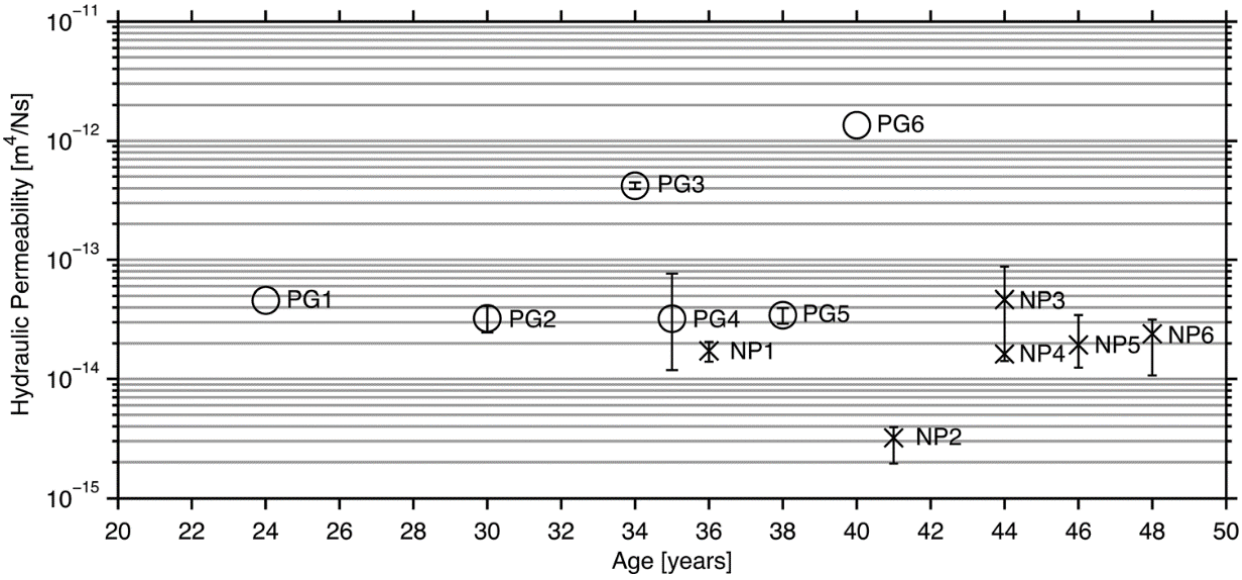

Figure 44: Permeability of human cervical tissue specimens, pregnant (PG) and nonpregnant (NP).

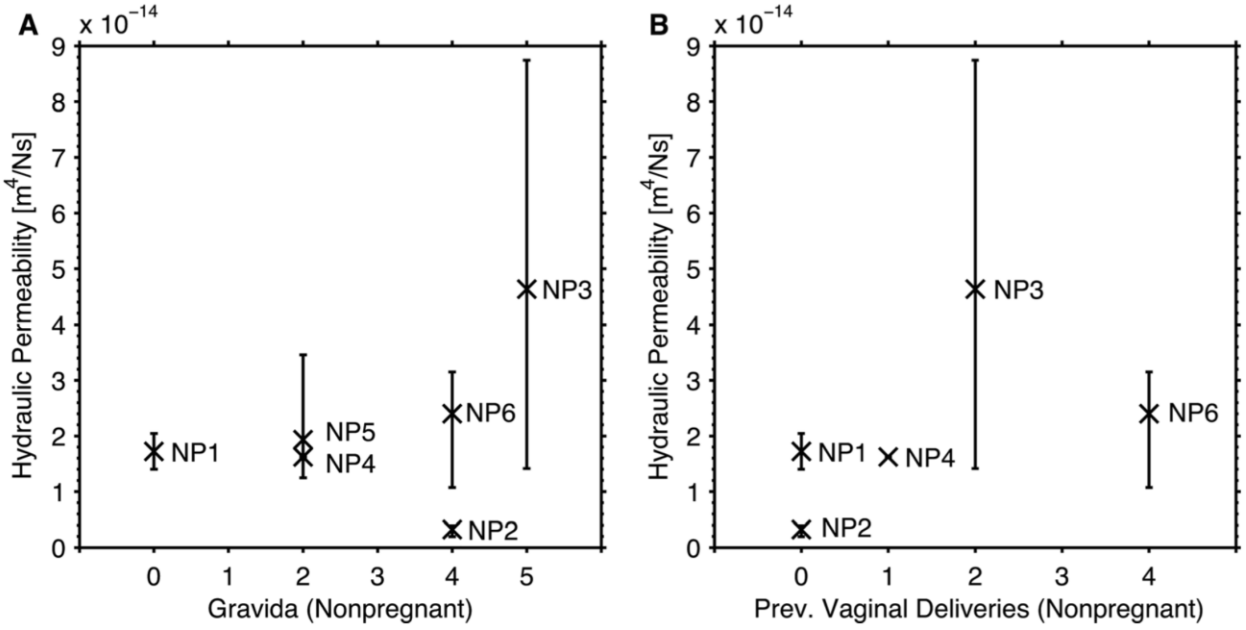

Figure 45: (a) Nonpregnant permeability versus gravida (number of pregnancies). (b) Nonpregnant permeability versus number of prior vaginal births (linear plot). There was not enough obstetric information to include specimen NP5 in panel B. Each point represents the mean permeability from all specimens from a given patient. The error bars represent the minimum and maximum measured permeability values (range) for a given patient.

A logistic statistical model using the generalized estimating equation (GEE) method [121], [122] was fitted to our results in the R statistics package with the individual specimens grouped according to patient and then pregnancy status. This method accounts for varying sample sizes for each patient and includes compensation for outlier effects. Application of the model found an NP permeability of $2.23\times10^{-14}\,m^4/N\cdot s$ (standard error: $4.3\times10^{-15}\,m^4/N\cdot s$) and a PG permeability of $1.73\times10^{-14}\,m^4/N\cdot s$ (standard error: $1.1\times10^{-13}\,m^4/N\cdot s$) with no significant difference (p-value: 0.157).

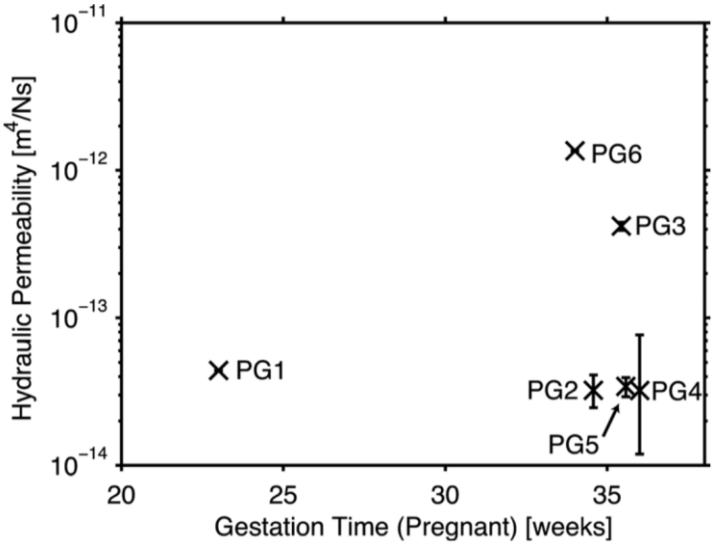

Figure 46: Mean hydraulic permeability of the specimens for each pregnant patient versus gestation time at hysterectomy. Each data point is the mean permeability across all specimens from a given patient. Error bars represent the minimum and maximum measured permeability values for a given cervix sample.

Due to the limited number of samples per slice, we found no statistically significant trend in the hydraulic permeability of the tissue samples according to their position from the internal *os* (i.e. slice number). The error bars in Figure 44 represent the spread of the permeability readings for all specimens from each respective cervix. For the NP tissue, we noted a gradual trend of increasing permeability with increasing age (Figure 44) and gravida, the number of prior pregnancies (Figure 45(a)).

The lowest NP average permeability we measured corresponds to a patient who had no prior vaginal deliveries (NP2). Additional experiments are required to draw a statistical conclusion. Because of the scarcity of early-term hysterectomy procedures, we were only able to obtain one sample from prior to 33 weeks of gestation. There is not a discernible trend between our PG1 specimen at 23 weeks and the remaining specimens which fall between 34 and 36 weeks (Figure 46). Permeability measurements beyond 34 weeks fall in a range between $1.4\times10^{-12}\ \mathrm{m}^4/\mathrm{N}\cdot s$ and $3.2\times10^{-14}\ \mathrm{m}^4/\mathrm{N}\cdot s$.

5.2.2.6 Discussion

A crucial element missing from current diagnostic techniques for CI is the integration of cervical material properties to determine the mechanical strength of the cervix during pregnancy. The most recent rodent

studies of cervical remodeling [100], [108]–[110], [123], [124] give clear evidence that cervical remodeling occurs in progressive stages, that remodeling is facilitated by a shift in cervical extracellular (ECM) matrix components, and that there are distinct molecular pathways that differentiate normal term ripening from premature cervical remodeling. The corresponding cervical mechanical property changes during these remodeling events are unknown, and because of the lack of mechanical testing data on cervical tissue, characterizing its mechanical function during normal and abnormal pregnancy remains elusive. To build a framework to quantify such mechanical and material properties, our group conducts mechanical and biochemical tests on ex vivo human cervical tissue samples to elucidate ECM-material property relationships. Our regimen of mechanical tests are tailored to account for the complex nonlinear, time dependent, and anisotropic material properties of the cervical tissue. The study presented here comprises two main components of our continued work to characterize the mechanical behavior of cervical tissue. First, we developed and built a mechanical testing fixture to directly measure the hydraulic permeability of soft tissues. Second, we measured the hydraulic permeability k of ex vivo human cervix specimens in the NP and PG states. The permeability measurements reported here provide material characteristics for the cervix which identify the poroelastic contribution to the time-dependent deformation mechanisms of the tissue.

We measured the hydraulic permeability k of NP tissue to be in the range of 10^{-15} $\mathrm{m}^4/\mathrm{N}\cdot s$ to 10^{-14} $\mathrm{m}^4/\mathrm{N}\cdot s$ and we measured k for PG tissue to be in the range of 10^{-14} $\mathrm{m}^4/\mathrm{N}\cdot s$ to 10^{-12} $\mathrm{m}^4/\mathrm{N}\cdot s$. The permeability k values of the NP tissue matched well with the permeabilities reported for other load-bearing collagenous tissues, such as cartilage [125] and human lumbar annulus fibrosis [114] that have permeabilities on the order of 10^{-15} $\mathrm{m}^4/\mathrm{N}\cdot s$ to 10^{-14} $\mathrm{m}^4/\mathrm{N}\cdot s$. In addition, we were confident we reached a steady-state fluid flow in our experiments because our testing times were well beyond the time constant estimated using an analytical solution for transient permeation in a biphasic (i.e. poroelastic) material [126]. See Figure 43. The solution for the characteristic time constant to reach steady state is

$\tau \sim h^2/(\pi^2 H_A k)$, where h is specimen height, k is a hydraulic permeability, and H_A is a confined compression modulus. Based on our previously reported confined compression results of another set of cervical tissue samples [37], we can estimate H_A for PG tissue to be 1 kPa, and from this study we can use the lowest permeability measured for PG tissue to be on the order of $10^{-14}\ \mathrm{m}^4/\mathrm{N}\cdot s$. Therefore, a conservative estimate of the characteristic time to reach steady state is $\tau \sim 169$ min, and our tests were generally held for durations longer than 4τ.

5.2.2.7 Limitations and Considerations

This study presents the first measurements of hydraulic permeability of human cervical tissue. These values provide a necessary material parameter when characterizing the time-dependent mechanical behavior of cervical tissue. Due to the nature of obtaining human cervical tissue and the complexity of its underlying ECM, we were faced with study design limitations and were forced to make simplifying assumptions when analyzing the tissue. All specimens tested in this study were obtained from patients who were indicated for hysterectomy due to nonmalignant conditions such as uterine fibroids, ovarian cysts, or menstrual pain, or complications in pregnancy such as placenta accreta or placenta previa. The effects of such conditions on the mechanical properties on the cervix are unknown. Our specimens, especially PG ones that were collected from patients with confirmed placenta accreta or previa, may be influenced by these unknown factors. Due to specimen availability, it was difficult to conduct statistical analysis of our data to analyze the influence of age, gravida, and gestational week on permeability. Overall, PG tissue was more permeable than NP tissue, as expected, due to the known ECM turnover and collagen network remodeling that happens during cervical remodeling. However, we did not have properly age-matched specimens to make a statistical comparison between the two groups. In addition, it was difficult to understand if there was an effect of age on tissue permeability for the NP specimens because it was not possible to control for obstetric history, especially if we accounted for a detailed analysis of the number of previous pregnancies, previous vaginal deliveries, previous miscarriages, and previous terminations.

Another group conducted ultrasound attenuation experiments on in vivo cervical tissue and suggested that women can have significantly different starting points for the microstructure (and by extension, inherent mechanical properties) of their cervical tissue [89]. The large spread of permeability values between the patients, particularly between PG cervices, highlights this point as well. Our results suggest that women can have significantly different cervical tissue properties and these material properties may be influenced by multiple combined factors (e.g. genetics, vaginal flora, oral contraceptive use, smoking, cervical surgical procedures, obstetric history, etc.). Our work underscores the need of patient-specific longitudinal studies of the ripening process and continued mechanical studies of cervical tissue to develop in vivo tools to measure cervical material properties. For this study, all permeation tests were conducted on mid-stromal samples in the direction parallel to the inner canal. Previous work by other groups used magnetic resonance tensor diffusion [127] and X-ray [128] to study and image three seamless zones of structured collagen in the stroma: the innermost and outermost zones contain collagen fibers preferentially aligned in the longitudinal direction and the middle zone contains collagen fibers preferentially aligned in the circumferential direction. We have assumed for this work that the mid-stromal region contained preferentially-aligned collagen fibers in the circumferential direction, where fibers were arranged circularly around the inner canal. Therefore, all samples were tested such that these circumferential fibers were presumably perpendicular to the direction of flow. All samples were saved for further histological analysis to confirm this directionality. Furthermore, some specimens contained heterogeneities in the form of small cysts (fluid-filled voids). These cysts were noted for future analysis of large-scale structural strength and such heterogeneities were avoided in this specimen preparation procedure.

5.2.2.8 Future Work.

Integrated biochemical, histological, and mechanical data on whole cervical tissue from women with different obstetric background is limited in the literature. To quantify cervical ECM-material property relationships, we plan to conduct biochemical and histological analysis on the tissue samples tested in this

paper, including both the tested tissue and tissue from adjacent sites. We plan to analyze the collagen crosslinking content, glycosaminoglycan content, and collagen directionality for each of the whole cervices collected. We know that the hyaluronic acid (HA) and fixed charged density (FCD) of the tissue increases with cervical maturation during pregnancy, and we also know this ECM change is accompanied by a turnover of the collagen fibrils to a more disorganized and less crosslinked network. The increase in HA and FCD would essentially increase the viscosity of the interstitial fluid and decrease the hydraulic permeability of the tissue, and the increase in collagen turnover would increase the hydraulic permeability. Therefore, ECM components must be measured to determine their contribution to the overall permeability. In addition to our planned biochemical and histological analysis, we will measure permeability of cervical tissue in different anatomical directions and at varying levels of strain. Additional mechanical tests in different modes of deformation will also be conducted to further characterize the complex nature of the tissue. In this paper, we report apparent hydraulic permeability measurements. These measurements assume a constant permeability value that does not depend on strain from either specimen clamping or from interstitial fluid drag. In the results presented here, no strain was applied via clamping, but there may be small effects from fluid drag. In future experiments, we will impose varying strain levels and varying fluid pressures to the same specimen to quantify the intrinsic permeability k_0 (the permeability at zero strain from the pressure gradient or clamping) and the strain sensitivity M_0 [125].

5.2.2.9 Conclusions

There is a strong need to determine the etiologies of CI, to develop in vivo diagnostic tools that measure cervical strength, and to identify potential therapeutic treatments to arrest premature dilation. This study is a necessary first step to understand the differences of cervical mechanical properties between women with different obstetric backgrounds. Here we present experimentally measured hydraulic permeability of human cervical tissue from NP and PG hysterectomy patients, which can be implemented directly into a poroelastic-type material model to estimate cervical mechanical behavior. We found an order

of magnitude difference between the mean permeability of the NP and PG tissues and we found a large variation between the permeabilities of different cervical samples with similar obstetric backgrounds. These findings highlight the need to develop patient-specific methods for an in vivo, quantitative material property assessment. Continued studies will include additional specimens to obtain appropriate controls and the measurement of direction-dependent and strain-dependent permeability of cervical tissue. This study is the foundation for future studies by our group to characterize cervical remodeling and to develop in vivo imagining techniques to measure cervical material properties.

5.2.2.10 Acknowledgment

We would like to thank Sevan Oungoulian, Ph.D. Candidate in the Musculoskeletal Biomechanics Lab at Columbia University, for his assistance and advice during the development of this experiment, Noelia Zork, M.D., Maternal Fetal Medicine Fellow at the Columbia Medical Center, for her help with specimen collection and analysis, Professor Cande V. Ananth, Ph.D. for his advice on statistical methods, and Taylor Chaintreuil, Undergraduate Research Assistant, for her help with several aspects of the project.

5.3 Relationship Between ADC and Permeability in Hydrogels

5.3.1 Methods

A phantom with polyacrylamide hydrogels (1:19 bis:acrylamide ratio) ranging from 3 to 30% (v/v) polyacrylamide/H2O was created. A full body Philips 3T Achieva scanner with 8-channel head coil was used to scan the phantom at room temperature. Diffusion weighted images were acquired with a single-shot spin echo (SE-EPI) sequence (TR/TE=2000/57 ms, matrix size=112x89, SENSE factor=2, slice thickness=2 mm, gap=1 mm, 7 slices, total scan time=2m30s) using multiple b-factors (0, 10, 20, 40, 80, 120, 160, 200, 240, 300, 500, 800, 900, 1000, 1200, 1500 s/mm^2) and diffusion sensitizing gradients in 3 orthogonal directions. A mono-exponential fit was performed to generate ADC maps from the data.

Hydraulic permeability measurements of separate polyacrylamide hydrogel phantoms with the same concentrations (3-30% v/v) were performed using a custom permeation experiment developed in our lab and originally used to measure the permeability of human cervical tissue. The experiment applies a fluid pressure gradient across a specimen and measures the resulting flow rate, giving the permeability.

5.3.2 Results

All image analysis on ADC maps was performed using Osirix, an open source image viewer. ROIs were created inside each phantom on all three slices centered within the phantoms. Mean ADC and standard deviation were recorded in each ROI for each specimen, and the results were fitted to a linear curve using least squares regression (R^2=0.995). Over three slices, ROI average ADC values all had a standard deviation within 2% of the mean. ADC was observed to decrease linearly with increasing polyacrylamide concentration, consistent with expectation (Figure 48). Permeability was found to decrease exponentially with linearly increasing polyacrylamide concentration (R^2=0.986) (Figure 47). This trend was stronger after corrections were made for gel concentration using the dry weight of each specimen.

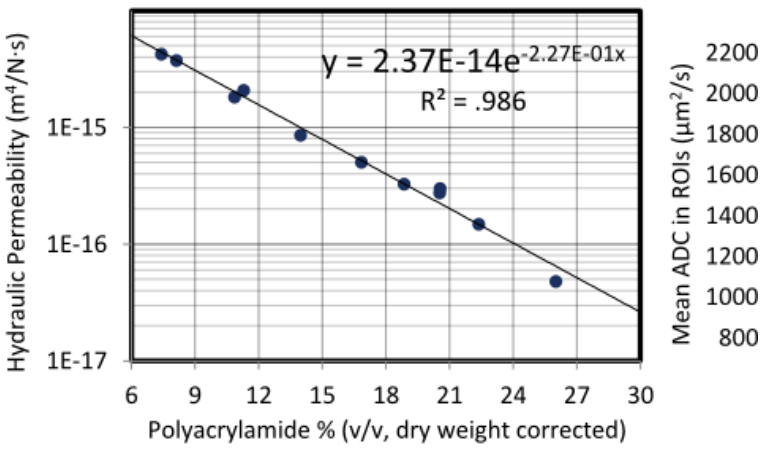

Figure 47: Permeability of polyacrylamide gels from 3 to 30% v/v.

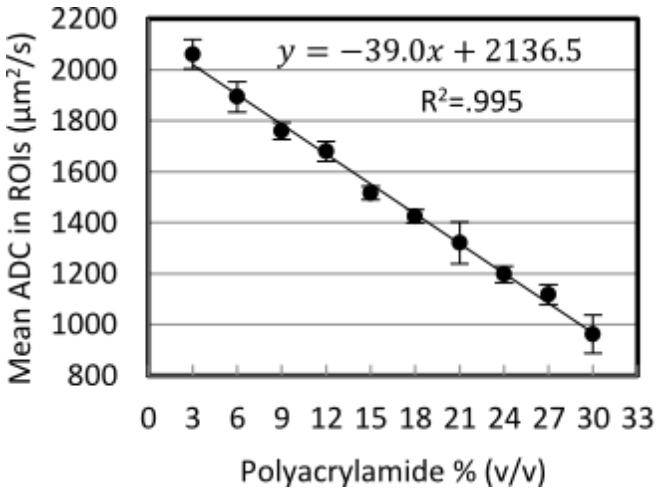

Figure 48: Apparent Diffusion Coefficient of polyacrylamide gels from 3 to 30% v/v.

5.3.3 Discussion

Research on the relationship between hydraulic permeability and MRI ADC is limited. In this study, a strong correlation between ADC and permeability has been characterized in polyacrylamide

hydrogels. There is a need for future studies in the field to explore what relationship between may exist between permeability and diffusion in cervical tissue. Cervical ADC might be able to quantify permeability differences linked to microstructural organization and tissue strength. Additionally, diffusion tensor data will be paired with direction-dependent permeability tests on grown collagen scaffolds to learn about the impact of microstructure directionality on this technique.

6 Conclusion

With this work, we add to the body of engineering knowledge new tools and methods which can be used to study preterm dilation of the cervix, measure cervical material mechanical properties, and predict how much dilation will occur under certain loading conditions. Our finite element models can simulate with new detail the mechanical deformation that occurs during pregnancy. With a mechanics-based mathematical platform for evaluating PTB interventions, educated decisions can be made and new interventions can be designed. In addition, advances made with respect to the relationship between permeability and diffusion in hydrated materials and tissues have broad potential applications throughout biomechanics as experimental, diagnostic, and predictive tools.

References

[1] K. M. Myers, A. Paskaleva, M. House, and S. Socrate, “Mechanical and biochemical properties of human cervical tissue.,” *Acta Biomater.*, vol. 4, no. 1, pp. 104–16, Jan. 2008.

[2] W. Bürzle and E. Mazza, “About Puncture Testing Applied for Mechanical Characterization of Fetal Membranes,” *J Biomech Eng*, vol. 136, no. November 2014, pp. 1–8, 2016.

[3] S. Beck, D. Wojdyla, L. Say, A. P. Betran, M. Merialdi, J. H. Requejo, C. Rubens, R. Menon, and P. F. A. Van Look, “The worldwide incidence of preterm birth: A systematic review of maternal mortality and morbidity,” *Bull. World Health Organ.*, vol. 88, no. 1, pp. 31–38, 2010.

[4] H. Blencowe, S. Cousens, D. Chou, M. Oestergaard, L. Say, A.-B. Moller, M. Kinney, and J. Lawn, “Born too soon: the global epidemiology of 15 million preterm births.,” *Reprod. Health*, vol. 10 Suppl 1, no. Suppl 1, p. S2, 2013.

[5] J. A. Martin, B. E. Hamilton, P. D. Sutton, S. J. Ventura, F. Menacker, S. Kirmeyer, T. J. Mathews, and V. Statistics, “Births: Final Data for 2011,” *Natl. Vital Stat. Repots*, vol. 62, no. 1, pp. 1–69, 2013.

[6] T. J. Mathews and M. F. MacDorman, “Infant mortality statistics from the 2010 Period Linked Birth/Infant Death data set,” *Natl. Vital Stat. Reports*, vol. 62, no. 8, pp. 1–33, 2013.

[7] W. M. W. Callaghan, M. M. F. MacDorman, S. S. A. Rasmussen, C. Qin, and E. E. M. Lackritz, “The contribution of preterm birth to infant mortality rates in the United States.,” *Pediatrics*, vol. 118, no. 4, pp. 1566–73, 2006.

[8] C. G. Solomon and J. D. Iams, “Prevention of Preterm Parturition,” *N Engl J Med*, vol. 3703370, pp. 254–61, 2014.

[9] M. G. Gravett, C. E. Rubens, and T. M. Nunes, “Global report on preterm birth and stillbirth (2 of 7): discovery science,” *BMC Pregnancy Childbirth*, vol. 10, no. 1, pp. 1–16, 2010.

[10] S. S. Hassan, R. Romero, D. Vidyadhari, S. Fusey, J. K. Baxter, M. Khandelwal, J. Vijayaraghavan, Y. Trivedi, P. Soma-Pillay, P. Sambarey, A. Dayal, V. Potapov, J. O’Brien, V. Astakhov, O. Yuzko, W. Kinzler, B. Dattel, H. Sehdev, L. Mazheika, D. Manchulenko, M. T. Gervasi, L. Sullivan, A. Conde-Agudelo, J. A. Phillips, and G. W. Creasy, “Vaginal progesterone reduces the rate of preterm birth in women with a sonographic short cervix: a multicenter, randomized, double-blind, placebo-controlled trial,” *Ultrasound Obstet. Gynecol.*, vol. 38, no. 1, pp. 18–31, Jul. 2011.

[11] M. House and S. Socrate, “The cervix as a biomechanical structure.,” *Ultrasound Obstet. Gynecol.*, vol. 28, no. 6, pp. 745–9, Nov. 2006.

[12] J. Y. Vink, S. Qin, C. O. Brock, N. M. Zork, H. M. Feltovich, X. Chen, P. Urie, K. M. Myers, T. J. Hall, R. Wapner, J. K. Kitajewski, C. J. Shawber, and G. Gallos, "A new paradigm for the role of smooth muscle cells in the human cervix.," *Am. J. Obstet. Gynecol.*, vol. 215, no. 4, p. 478.e1-478.e11, 2016.

[13] J. E. Norman and A. H. Shennan, "Prevention of preterm birth-why can't we do any better?," *Lancet*, vol. 381, no. 9862, pp. 184–185, 2013.

[14] M. Dziadosz, T.-A. Bennett, C. Dolin, A. W. Honart, A. Pham, S. S. Lee, S. Pivo, and A. S. Roman, "Uterocervical angle: A novel ultrasound marker to predict spontaneous preterm birth," *American Journal of Obstetrics and Gynecology*, vol. 214, no. 1 SUPPL. 1. p. S32, 2016.

[15] E. H. Bishop, "Pelvic Scoring for Elective Induction.," *Obstet. Gynecol.*, vol. 24, pp. 266–268, Aug. 1964.

[16] R. B. Newman, R. L. Goldenberg, J. D. Iams, P. J. Meis, B. M. Mercer, A. H. Moawad, E. Thom, M. Miodovnik, S. N. Caritis, and M. Dombrowski, "Preterm Prediction Study," *Obstet. Gynecol.*, vol. 112, no. 3, pp. 508–515, Sep. 2008.

[17] K. M. Myers, H. Feltovich, E. Mazza, and J. Vink, "The Mechanical Role of the Cervix In Pregnancy," pp. 1–46.

[18] J. Vink, S. Qin, P. Praditpan, C. V. Ananth, K. Yoshida, K. Myers, M. Sheetz, R. Wapner, G. Gallos, and J. Kitajewski, "201: Human cervical smooth muscle stretch increases matrix metalloproteinase secretion: a new mechanism to explain premature cervical remodeling," *Am. J. Obstet. Gynecol.*, vol. 214, no. 1, p. S122, Jan. 2016.

[19] K. M. Waldorf, N. Singh, A. R. Mohan, R. C. Young, L. Ngo, A. Das, J. Tsai, A. Bansal, L. Paolella, B. R. Herbert, S. R. Sooranna, G. M. Gough, C. Astley, K. Vogel, A. E. Baldessari, T. K. Bammler, J. MacDonald, M. G. Gravett, L. Rajagopal, and M. R. Johnson, "Uterine overdistention induces preterm labor mediated by inflammation: Observations in pregnant women and nonhuman primates," *Am. J. Obstet. Gynecol.*, vol. 213, no. 6, p. 830.e1-830.e19, 2015.

[20] H. Mahmoud, A. Wagoner Johnson, E. K. Chien, M. J. Poellmann, and B. McFarlin, "System-level biomechanical approach for the evaluation of term and preterm pregnancy maintenance.," *J. Biomech. Eng.*, vol. 135, no. 2, p. 21009, 2013.

[21] K. M. Myers, H. Feltovich, E. Mazza, J. Vink, M. Bajka, R. J. Wapner, T. J. Hall, and M. House, "The mechanical role of the cervix in pregnancy," *J. Biomech.*, vol. 48, no. 9, pp. 1511–1523, 2015.

[22] M. Fernandez, M. House, S. Jambawalikar, N. Zork, J. Vink, R. Wapner, and K. Myers, "Investigating the mechanical function of the cervix during pregnancy using finite element models derived from high-resolution 3D MRI," *Comput. Methods Biomech. Biomed. Engin.*, vol. 19, no. 4,

pp. 404–417, Mar. 2016.

[23] S. Badir, E. Mazza, R. Zimmermann, and M. Bajka, “Cervical softening occurs early in pregnancy: Characterization of cervical stiffness in 100 healthy women using the aspiration technique,” *Prenat. Diagn.*, vol. 33, pp. 737–741, 2013.

[24] M. House, R. McCabe, and S. Socrate, “Using imaging-based, three-dimensional models of the cervix and uterus for studies of cervical changes during pregnancy.,” *Clin. Anat.*, vol. 26, no. 1, pp. 97–104, Jan. 2013.

[25] A. P. Paskaleva, “Biomechanics of Cervical Function in Pregnancy - Case of Cervical Insufficiency by,” 2007.

[26] K. M. Myers, C. P. Hendon, Y. Gan, W. Yao, K. Yoshida, M. Fernandez, J. Vink, and R. J. Wapner, “A continuous fiber distribution material model for human cervical tissue,” *J. Biomech.*, vol. 48, no. 9, pp. 1533–1540, 2015.

[27] S. A. Maas, B. J. Ellis, G. A. Ateshian, and J. Weiss, “FEBio: finite elements for biomechanics.,” *J. Biomech. Eng.*, vol. 134, no. 1, p. 11005, Jan. 2012.

[28] “Preterm birth: Fact sheet N°363,” 2015.

[29] U. M. Reddy, R. Goldenberg, R. Silver, G. C. Smith, R. M. Pauli, R. J. Wapner, J. Gardosi, H. Pinar, M. Grafe, and M. Kupferminc, “Stillbirth classification-developing an international consensus for research: executive summary of a National Institute of Child Health and Human Development workshop.,” *Obs. Gynecol*, vol. 114, 2009.

[30] I. J. D., “Prevention of Preterm Parturition,” *N. Engl. J. Med.*, vol. 370, no. 3, pp. 254–261, 2014.

[31] V. Berghella, S. Blackwell, B. Anderson, S. Chauhan, J. Copel, C. Gyamfi, D. Johnson, G. Saade, H. Simhan, and L. Simpson, “Progesterone and preterm birth prevention: translating clinical trials data into clinical practice,” *Am. J. Obstet. Gynecol.*, vol. 206, no. 5, pp. 376–386, May 2012.

[32] K. M. Myers, S. Socrate, A. Paskaleva, and M. House, “A study of the anisotropy and tension/compression behavior of human cervical tissue.,” *J. Biomech. Eng.*, vol. 132, no. 2, p. 21003, Feb. 2010.

[33] W. Yao, K. Yoshida, M. Fernandez, J. Vink, R. J. Wapner, C. V. Ananth, M. L. Oyen, and K. M. Myers, “Measuring the compressive viscoelastic mechanical properties of human cervical tissue using indentation,” *J. Mech. Behav. Biomed. Mater.*, vol. 34, pp. 18–26, 2014.

[34] N. Zork, J. Vink, K. Yoshida, S. Cremers, H. Jiang, C. Ananth, R. Wapner, J. Kitajewski, and K.

Myers, “746: The affect of parity on the distribution of collagen crosslinks in the human cervix,” *Am. J. Obstet. Gynecol.*, vol. 210, no. 1, pp. S366–S367, Jan. 2014.

[35] M. Zilianti, A. Azuaga, F. Calderon, G. Pages, and G. Mendoza, “Monitoring the effacement of the uterine cervix by transperineal sonography: a new perspective.,” *J. Ultrasound Med.*, vol. 14, no. 10, pp. 719–724, Oct. 1995.

[36] M. House, R. a Bhadelia, K. M. Myers, and S. Socrate, “Magnetic resonance imaging of three-dimensional cervical anatomy in the second and third trimester.,” *Eur. J. Obstet. Gynecol. Reprod. Biol.*, vol. 144 Suppl, pp. S65-9, May 2009.

[37] M. House, H. Feltovich, T. J. Hall, T. Stack, a. Patel, and S. Socrate, “Three-Dimensional, Extended Field-of-View Ultrasound Method for Estimating Large Strain Mechanical Properties of the Cervix during Pregnancy,” *Ultrason. Imaging*, vol. 34, no. 1, pp. 1–14, Jan. 2012.

[38] G. Pearsall and V. Roberts, “Passive mechanical properties of uterine muscle (myometrium) tested in vitro,” *J. Biomech.*, 1978.

[39] J. Benson-Martin, P. Zammaretti, G. Bilic, T. Schweizer, B. Portmann-Lanz, T. Burkhardt, R. Zimmermann, and N. Ochsenbein-Kölble, “The Young’s modulus of fetal preterm and term amniotic membranes.,” *Eur. J. Obstet. Gynecol. Reprod. Biol.*, vol. 128, no. 1–2, pp. 103–7, 2006.

[40] M. L. Oyen, S. E. Calvin, and R. F. Cook, “Uniaxial stress-relaxation and stress-strain responses of human amnion.,” *J. Mater. Sci. Mater. Med.*, vol. 15, no. 5, pp. 619–24, May 2004.

[41] M. Fernandez, J. Vink, K. Yoshida, R. Wapner, and K. M. Myers, “Direct measurement of the permeability of human cervical tissue.,” *J. Biomech. Eng.*, vol. 135, no. 2, p. 21024, 2013.

[42] C. S. Buhimschi, I. A. Buhimschi, A. M. Malinow, and C. P. Weiner, “Intrauterine Pressure During the Second Stage of Labor in Obese Women,” *Obstet. Gynecol.*, vol. 103, no. 2, pp. 225–230, Mar. 2004.

[43] C. S. Buhimschi, I. A. Buhimschi, A. M. Malinow, and C. Weiner, “Intrauterine Pressure During the Second Stage of Labor in Obese Women,” *Obstet. Gynecol.*, vol. 103, no. 2, pp. 225–230, Mar. 2004.

[44] M. Jabareen, A. S. Mallik, G. Bilic, A. H. Zisch, and E. Mazza, “Relation between mechanical properties and microstructure of human fetal membranes: an attempt towards a quantitative analysis.,” *Eur. J. Obstet. Gynecol. Reprod. Biol.*, vol. 144 Suppl, pp. S134-41, May 2009.

[45] P. Frigo, C. Lang, M. Sator, R. Ulrich, and P. Husslein, “MEMBRANE THICKNESS AND PROM - HIGH-FREQUENCY ULTRASOUND,” *PRenat. Diagn.*, vol. 18, no. 4, pp. 333–337, 1998.

[46] F. G. Cunningham, K. J. Leveno, S. L. Bloom, J. C. Hauth, D. J. Rouse, and C. Y. Spong, "Chapter 6. Parturition," in *Williams Obstetrics, 23e*, New York, NY: The McGraw-Hill Companies, 2010.

[47] G. Ateshian, "Modeling the matrix of articular cartilage using a continuous fiber angular distribution predicts many observed phenomena," *J. …*, vol. 131, no. 6, pp. 1–34, 2009.

[48] G. Ateshian, "Anisotropy of fibrous tissues in relation to the distribution of tensed and buckled fibers," *J. Biomech. …*, vol. 129, no. 2, pp. 240–9, Apr. 2007.

[49] Y. Lanir, "Constitutive equations for fibrous connective tissues," *J. Biomech.*, 1983.

[50] G. van Baaren, J. Y. Vis, F. F. Wilms, M. A. Oudijk, A. Kwee, M. M. Porath, G. Oei, H. C. J. Scheepers, M. E. A. Spaanderman, K. W. M. Bloemenkamp, M. C. Haak, A. C. Bolte, C. J. Bax, J. M. J. Cornette, J. J. Duvekot, B. W. A. Nij Bijvanck, J. van Eyck, M. T. M. Franssen, K. M. Sollie, F. Vandenbussche, M. Woiski, W. A. Grobman, J. A. M. van der Post, P. M. M. Bossuyt, B. C. Opmeer, and B. W. J. Mol, "Predictive value of cervical length measurement and fibronectin testing in threatened preterm labor.," *Obstet. Gynecol.*, vol. 123, no. 6, pp. 1185–92, 2014.

[51] A. Mauri, M. Perrini, A. E. Ehret, D. S. A. De Focatiis, and E. Mazza, "Time-dependent mechanical behavior of human amnion: Macroscopic and microscopic characterization.," *Acta Biomater.*, pp. 25–31, Sep. 2014.

[52] A. Mauri, M. Perrini, J. M. Mateos, C. Maake, N. Ochsenbein-Koelble, R. Zimmermann, M. Ehrbar, and E. Mazza, "Second harmonic generation microscopy of fetal membranes under deformation: normal and altered morphology.," *Placenta*, vol. 34, no. 11, pp. 1020–6, Nov. 2013.

[53] W. Yao, K. Yoshida, M. Fernandez, J. Vink, and J. Ronald, "Measuring the Material Parameters of Human Cervical Tissue using Indentation."

[54] R. L. Goldenberg, J. D. Iams, B. M. Mercer, P. J. Meis, A. H. Moawad, R. L. Copper, A. Das, E. Thom, F. Johnson, D. McNellis, M. Miodovnik, J. P. Van Dorsten, S. N. Caritis, G. R. Thurnau, and S. F. Bottoms, "The preterm prediction study: the value of new vs standard risk factors in predicting early and all spontaneous preterm births. NICHD MFMU Network.," *Am. J. Public Health*, vol. 88, no. 2, pp. 233–238, 1998.

[55] M. J. Fernandez, A. E. Ehret, E. Mazza, M. House, J. S. Vink, R. Wapner, and K. M. Myers, "The effect of fetal membrane prestretch on cervical loading during pregnancy," in *Proceedings of the 39th annual meeting of the American Society of Biomechanics*, 2015, pp. 4–5.

[56] J. Wolff, P. Maquet, and R. Furlong, *The Law of Bone Remodelling*. Berlin: Springer-Verlag, 1986.

[57] W. Wilson, "Stresses in the local collagen network of articular cartilage: a poroviscoelastic fibril-reinforced finite element study," *J. Biomech.*, vol. 37, no. 3, pp. 357–366, Mar. 2004.

[58] F. Baaijens, C. Bouten, and N. Driessen, “Modeling collagen remodeling.,” *J. Biomech.*, vol. 43, no. 1, pp. 166–75, Jan. 2010.

[59] H. Mahmoud, A. Wagoner Johnson, E. K. Chien, M. J. Poellmann, and B. McFarlin, “System-level biomechanical approach for the evaluation of term and preterm pregnancy maintenance.,” *J. Biomech. Eng.*, vol. 135, no. 2, p. 21009, Feb. 2013.

[60] N. M. Fisk, D. Ronderos-Dumit, Y. Tannirandorn, U. Nicolini, D. Talbert, and C. H. Rodeck, “Normal amniotic pressure throughout gestation,” *BJOG An Int. J. Obstet. Gynaecol.*, vol. 99, no. 1, pp. 18–22, 1992.

[61] J. T. Conrad, W. L. Johnson, W. K. Kuhn, and C. A. J. Hunter, “Passive stretch relationships in human uterine muscle.,” *Am. J. Obstet. Gynecol.*, vol. 96, no. 8, pp. 1055–1059, Dec. 1966.

[62] B. Arabin and Z. Alfirevic, “Cervical pessaries for prevention of spontaneous preterm birth: Past, present and future,” *Ultrasound Obstet. Gynecol.*, vol. 42, no. 4, pp. 390–399, 2013.

[63] J. Iams, R. Goldenberg, P. Meis, B. Mercer, M. Atef, D. Anita, T. Elizabeth, M. Donald, R. Copper, J. Francee, and J. Roberts, “The Length of the Cervix and the Risk of Spontaneous Premature Delivery,” *N. Engl. J. Med.*, vol. 334, no. 9, pp. 567–573, 1996.

[64] M. M. Cannie, O. Dobrescu, L. Gucciardo, B. Strizek, S. Ziane, E. Sakkas, F. Schoonjans, L. Divano, and J. C. Jani, “Arabin cervical pessary in women at high risk of preterm birth: a magnetic resonance imaging observational follow-up study.,” *Ultrasound Obstet. Gynecol.*, vol. 42, no. 4, pp. 426–33, Oct. 2013.

[65] A. C. Gimovsky, A. Suhag, A. Roman, B. L. Rochelson, and V. Berghella, “Pessary versus cerclage versus expectant management for cervical dilation with visible membranes in the second trimester,” *J. Matern. Neonatal Med.*, no. August 2015, pp. 1–4, 2015.

[66] E. Nohuz, M. Albaut, L. De Simone, C. Fabre, D. Lemery, D. Gallot, and F. Vendittelli, “Comment je fais… un cerclage du col utérin en consultation, sans suture ni anesthésie,” *Gynécologie Obs. Fertil.*, vol. 43, no. 6, pp. 465–467, 2015.

[67] M. Goya, L. Pratcorona, C. Merced, C. Rodó, L. Valle, A. Romero, M. Juan, A. Rodríguez, B. Muñoz, B. Santacruz, J. C. Bello-Muñoz, E. Llurba, T. Higueras, L. Cabero, and E. Carreras, “Cervical pessary in pregnant women with a short cervix (PECEP): an open-label randomised controlled trial.,” *Lancet*, vol. 379, no. 9828, pp. 1800–6, May 2012.

[68] S. Liem, E. Schuit, M. Hegeman, J. Bais, K. De Boer, K. Bloemenkamp, J. Brons, H. Duvekot, B. N. Bijvank, M. Franssen, I. Gaugler, I. De Graaf, M. Oudijk, D. Papatsonis, P. Pernet, M. Porath, L. Scheepers, M. Sikkema, J. Sporken, H. Visser, W. Van Wijngaarden, M. Woiski, M. Van Pampus, B. W. Mol, and D. Bekedam, “Cervical pessaries for prevention of preterm birth in women

with a multiple pregnancy (ProTWIN): A multicentre, open-label randomised controlled trial," *Lancet*, vol. 382, no. 9901, pp. 1341–1349, 2013.

[69] K. H. Nicolaides, A. Syngelaki, L. C. Poon, G. Picciarelli, N. Tul, A. Zamprakou, E. Skyfta, M. Parra-Cordero, R. Palma-Dias, and J. Rodriguez Calvo, "A Randomized Trial of a Cervical Pessary to Prevent Preterm Singleton Birth," *N. Engl. J. Med.*, vol. 374, no. 11, pp. 1044–1052, 2016.

[70] K. H. Nicolaides, A. Syngelaki, L. C. Poon, C. de Paco Matallana, W. Plasencia, F. S. Molina, G. Picciarelli, N. Tul, E. Celik, T. K. Lau, and R. Conturso, "Cervical pessary placement for prevention of preterm birth in unselected twin pregnancies: a randomized controlled trial.," *Am. J. Obstet. Gynecol.*, vol. 214, no. 1, p. 3.e1-9, Jan. 2016.

[71] M. Goya, M. de la Calle, L. Pratcorona, C. Merced, C. Rodó, B. Muñoz, M. Juan, A. Serrano, E. Llurba, T. Higueras, E. Carreras, and L. Cabero, "Cervical pessary to prevent preterm birth in women with twin gestation and sonographic short cervix: a multicenter randomized controlled trial (PECEP-Twins)," *Am. J. Obstet. Gynecol.*, no. February, pp. 145–152, 2015.

[72] A. R. Westervelt, M. Fernandez, and J. Vink, "A Parameterized Ultrasound-Based Finite Element Analysis of the Mechanical Environment of Pregnancy," *J. Biomech. Eng.*

[73] E. C. Gillespie, "Principles of uterine growth in pregnancy.," *Am. J. Obstet. Gynecol.*, vol. 59, no. 5, pp. 949–59, May 1950.

[74] G. O. Shimon Degani, Zvi Leibovitz, Israel Shapiro, Ron Gonen, "Myometrial Thickness in Pregnancy : Longitudinal Sonographic Study," *J Ultrasound Med*, vol. 17, pp. 661–665, 1998.

[75] "Dr. Arabin GmbH & Co. KG. Cerclage Pessary non-perforated." [Online]. Available: http://www.dr-arabin.de/cerclage-pessary-non-perforated. [Accessed: 01-Jan-2016].

[76] D. N. Danforth, "The fibrous nature of the human cervix, and its relation to the isthmic segment in gravid and nongravid uteri.," *Am. J. Obstet. Gynecol.*, vol. 53, no. 4, pp. 541–560, Apr. 1947.

[77] J. M. Gonzalez, R. Romero, and G. Girardi, "Comparison of the mechanisms responsible for cervical remodeling in preterm and term labor," *J. Reprod. Immunol.*, vol. 97, no. 1, pp. 112–119, Mar. 2013.

[78] D. Stygar, "Increased Level of Matrix Metalloproteinases 2 and 9 in the Ripening Process of the Human Cervix," *Biol. Reprod.*, vol. 67, no. 3, pp. 889–894, Sep. 2002.

[79] M. Dziadosz, T.-A. Bennett, C. Dolin, A. West Honart, A. Pham, S. S. Lee, S. Pivo, and A. S. Roman, "Uterocervical angle: a novel ultrasound screening tool to predict spontaneous preterm birth," *Am. J. Obstet. Gynecol.*, vol. 214, no. 1 SUPPL. 1, p. S32, Mar. 2016.

[80] D. Le Bihan, “Molecular diffusion, tissue microdynamics and microstructure.,” *NMR Biomed.*, vol. 8, no. 7–8, pp. 375–86, 1996.

[81] P. J. Basser, J. Mattiello, and D. LeBihan, “MR diffusion tensor spectroscopy and imaging.,” *Biophys. J.*, vol. 66, no. 1, pp. 259–67, Jan. 1994.

[82] D. Le Bihan, J. F. Mangin, C. Poupon, C. a Clark, S. Pappata, N. Molko, and H. Chabriat, “Diffusion tensor imaging: concepts and applications.,” *J. Magn. Reson. Imaging*, vol. 13, no. 4, pp. 534–46, Apr. 2001.

[83] D. Le Bihan, “Looking into the functional architecture of the brain with diffusion MRI.,” *Nat. Rev. Neurosci.*, vol. 4, no. 6, pp. 469–80, Jun. 2003.

[84] C. Howson, M. Kinney, and J. Lawn, “Born too soon.,” Geneva, 2012.

[85] R. L. Goldenberg, J. F. Culhane, J. D. lams, and R. Romero, “Epidemiology and causes of preterm birth.,” *Lancet*, vol. 371, 2008.

[86] P. Hovi, S. Andersson, J. G. Eriksson, A.-L. Järvenpää, S. Strang-Karlsson, O. Mäkitie, and E. Kajantie, “Glucose regulation in young adults with very low birth weight.,” *N. Engl. J. Med.*, vol. 356, no. 20, pp. 2053–2063, 2007.

[87] J. D. Iams, F. F. Johnson, J. Sonek, L. Sachs, C. Gebauer, and P. Samuels, “Cervical competence as a continuum: a study of ultrasonographic cervical length and obstetric performance.,” *Am J Obs. Gynecol*, vol. 172, 1995.

[88] A. Thomas, S. Kümmel, O. Gemeinhardt, and T. Fischer, “Real-time sonoelastography of the cervix: tissue elasticity of the normal and abnormal cervix.,” *Acad. Radiol.*, vol. 14, no. 2, pp. 193–200, Feb. 2007.

[89] B. L. McFarlin, W. D. O’Brien, M. L. Oelze, J. F. Zachary, and R. C. White-Traut, “Quantitative ultrasound assessment of the rat cervix.,” *J. Ultrasound Med.*, vol. 25, no. 8, pp. 1031–40, Aug. 2006.

[90] H. Feltovich, K. Nam, and T. J. Hall, “Quantitative ultrasound assessment of cervical microstructure.,” *Ultrason. Imaging*, vol. 32, no. 3, pp. 131–42, Jul. 2010.

[91] B. L. McFarlin, T. a Bigelow, Y. Laybed, W. D. O’Brien, M. L. Oelze, and J. S. Abramowicz, “Ultrasonic attenuation estimation of the pregnant cervix: a preliminary report.,” *Ultrasound Obstet. Gynecol.*, vol. 36, no. 2, pp. 218–25, Aug. 2010.

[92] Y. Labyed, T. a Bigelow, and B. L. McFarlin, “Estimate of the attenuation coefficient using a clinical

array transducer for the detection of cervical ripening in human pregnancy.," *Ultrasonics*, vol. 51, no. 1, pp. 34–9, Jan. 2011.

[93] H. Feltovich, T. J. Hall, and V. Berghella, "Beyond cervical length: Emerging technologies for assessing the pregnant cervix," *Am. J. Obstet. Gynecol.*, vol. 207, no. 5, pp. 345–354, 2012.

[94] D. N. Danforth, A. Veis, M. Breen, H. G. Weinstein, J. C. Buckingham, and P. Manalo, "The effect of pregnancy and labor on the human cervix: changes in collagen, glycoproteins, and glycosaminoglycans.," *Am. J. Obstet. Gynecol.*, vol. 120, no. 5, p. 641, 1974.

[95] H. Mochiyama, E. Shimemura, and H. Kobayashi, "Shape Control of Manipulators with Hyper Degrees of Freedom," *Int. J. Rob. Res.*, vol. 18, no. 6, pp. 584–600, Jun. 1999.

[96] T. Shimizu, M. Endo, and Z. Yosizawa, "Glycoconjugates (glycosaminoglycans and glycoproteins) and glycogen in the human cervix uteri," *Tohoku J. Exp. Med.*, vol. 131, no. 3, pp. 289–299, 1980.

[97] K. Myers, S. Socrate, D. Tzeranis, and M. House, "Changes in the biochemical constituents and morphologic appearance of the human cervical stroma during pregnancy," *Eur. J. Obstet. Gynecol. Reprod. Biol.*, vol. 144, no. SUPPL 1, pp. 82–89, 2009.

[98] P. C. Leppert, "The Extracellular Matrix of the Uterus, Cervix, and Fetal Membranes: Synthesis, Degradation, and Hormonal Regulation," 1991.

[99] M. House, D. L. Kaplan, and S. Socrate, "Relationships between mechanical properties and extracellular matrix constituents of the cervical stroma during pregnancy.," *Semin. Perinatol.*, vol. 33, no. 5, pp. 300–7, Oct. 2009.

[100] M. L. Akins, K. Luby-Phelps, R. A. Bank, and M. Mahendroo, "Cervical softening during pregnancy: regulated changes in collagen cross-linking and composition of matricellular proteins in the mouse.," *Biol. Reprod.*, vol. 84, no. 5, pp. 1053–1062, May 2011.

[101] D. N. Danforth, J. C. Buckingham, and J. W. J. Roddick, "Connective tissue changes incident to cervical effacement.," *Am. J. Obstet. Gynecol.*, vol. 80, pp. 939–945, Nov. 1960.

[102] D. N. Danforth, "The morphology of the human cervix.," *Clin. Obstet. Gynecol.*, vol. 26, no. 1, pp. 7–13, Mar. 1983.

[103] P. C. Leppert, "Cervical softening, effacement and dilatation: A complex biochemical cascade," *J Matern Fetal Med*, vol. 1, pp. 213–23, 1992.

[104] P. C. Leppert, "The biochemistry and physiology of the uterine cervix during gestation and parturition," *Prenat. Neonatal Med.*, vol. 3, pp. 103–105, 1998.

[105] P. C. Leppert, “Anatomy and physiology of cervical ripening,” *Clin. Obstet. Gynecol.*, vol. 38, no. 2, p. 267, 1995.

[106] R. A. Word, X. H. Li, M. Hnat, and K. Carrick, “Dynamics of cervical remodeling during pregnancy and parturition: mechanisms and current concepts.,” *Semin Reprod Med*, vol. 25, 2007.

[107] B. Timmons, M. Akins, and M. Mahendroo, “Cervical remodeling during pregnancy and parturition,” *Trends Endocrinol. Metab.*, 2010.

[108] R. Holt, B. C. Timmons, Y. Akgul, M. L. Akins, and M. Mahendroo, “The molecular mechanisms of cervical ripening differ between term and preterm birth.,” *Endocrinology*, vol. 152, no. 3, pp. 1036–1046, Mar. 2011.

[109] M. Mahendroo, “Cervical remodeling in term and preterm birth: insights from an animal model.,” *Reproduction*, vol. 143, no. 4, pp. 429–438, Apr. 2012.

[110] Y. Akgul, R. Holt, M. Mummert, A. Word, and M. Mahendroo, “Dynamic changes in cervical glycosaminoglycan composition during normal pregnancy and preterm birth.,” *Endocrinology*, vol. 153, no. 7, pp. 3493–3503, Jul. 2012.

[111] X. Xu, Y. Akgul, M. Mahendroo, and A. Jerschow, “Ex vivo assessment of mouse cervical remodeling through pregnancy via 23Na MRS.,” *NMR Biomed.*, vol. 23, no. 8, pp. 907–912, Oct. 2010.

[112] W. Gu, “New insight into deformation-dependent hydraulic permeability of gels and cartilage, and dynamic behavior of agarose gels in confined compression,” *J. Biomech.*, vol. 36, no. 4, pp. 593–598, Apr. 2003.

[113] M. a Soltz and G. A. Ateshian, “Experimental verification and theoretical prediction of cartilage interstitial fluid pressurization at an impermeable contact interface in confined compression.,” *J. Biomech.*, vol. 31, no. 10, pp. 927–34, Oct. 1998.

[114] W. Y. Gu, X. G. Mao, R. J. Foster, M. Weidenbaum, V. C. Mow, and B. a Rawlins, “The anisotropic hydraulic permeability of human lumbar anulus fibrosus. Influence of age, degeneration, direction, and water content.,” *Spine (Phila. Pa. 1976).*, vol. 24, no. 23, pp. 2449–55, Dec. 1999.

[115] V. C. Mow, S. C. Kuei, W. M. Lai, and C. G. Armstrong, “Biphasic creep and stress relaxation of articular cartilage in compression? Theory and experiments.,” *J. Biomech. Eng.*, vol. 102, no. 1, pp. 73–84, Feb. 1980.

[116] Y. C. Fung, *Biomechanics*. New York, NY: Springer New York, 1993.

[117] W. M. Deen, *Analysis of transport phenomena (topics in chemical engineering)*, vol. 3. Oxford University Press, New York, 1998.

[118] K. M. Myers, M. L. Oyen, K. Yoshida, M. Fernandez, J. Vink, and R. Wapner, "Time-Dependent Indentation Response of Human Cervical Tissue," in *ASME 2012 Summer Bioengineering Conference*, 2012, pp. 1255–1256.

[119] M. Galli and K. Comley, "Viscoelastic and poroelastic mechanical characterization of hydrated gels," *J. Mater. …*, no. August 2008, pp. 973–979, 2009.

[120] C. A. Grattoni, H. H. Al-Sharji, C. Yang, A. H. Muggeridge, and R. W. Zimmerman, "Rheology and Permeability of Crosslinked Polyacrylamide Gel.," *J. Colloid Interface Sci.*, vol. 240, no. 2, pp. 601–607, Aug. 2001.

[121] S. L. Z. Kung-Yee Liang, "Longitudinal Data Analysis Using Generalized Linear Models," *Biometrika*, vol. 73, no. 1, pp. 13–22, 1986.

[122] L. P. Z. Ross L. Prentice, "Estimating Equations for Parameters in Means and Covariances of Multivariate Discrete and Continuous Responses," *Biometrics*, vol. 47, no. 3, pp. 825–839, 1991.

[123] M. L. Akins, K. Luby-Phelps, and M. Mahendroo, "Second harmonic generation imaging as a potential tool for staging pregnancy and predicting preterm birth," *J. Biomed. Opt.*, vol. 15, no. 2, p. 26020, 2010.

[124] S. Yousefi, N. Kehtarnavaz, M. Akins, K. Luby-Phelps, and M. Mahendroo, "Separation of preterm infection model from normal pregnancy in mice using texture analysis of second harmonic generation images," in *2010 Annual International Conference of the IEEE Engineering in Medicine and Biology*, 2010, pp. 5314–5317.

[125] M. H. Holmes and V. C. Mow, "The nonlinear characteristics of soft gels and hydrated connective tissus in ultrafiltration," *J. Biomech.*, vol. 23, no. 11, pp. 1145–1156, 1990.

[126] M. A. Soltz and G. A. Ateshian, "Interstitial Fluid Pressurization During Confined Compression Cyclical Loading of Articular Cartilage," *Ann. Biomed. Eng.*, vol. 28, no. 2, pp. 150–159, 2000.

[127] S. Weiss, T. Jaermann, P. Schmid, P. Staempfli, P. Boesiger, P. Niederer, R. Caduff, and M. Bajka, "Three-dimensional fiber architecture of the nonpregnant human uterus determined ex vivo using magnetic resonance diffusion tensor imaging.," *Anat. Rec. A. Discov. Mol. Cell. Evol. Biol.*, vol. 288, no. 1, pp. 84–90, Jan. 2006.

[128] R. M. Aspden, "Collagen organisation in the cervix and its relation to mechanical function.," *Coll. Relat. Res.*, vol. 8, no. 2, pp. 103–112, Mar. 1988.

Appendix

A.1 inp2feb Documentation

A.1.1 Purpose

The objective of this project was to create a streamlined software tool to convert .inp files from Trelis to .feb files for solving within the FEBio finite element solver. This program facilitates the use of Trelis and FEBio to perform analyses on geometries with defined boundary conditions, contact definitions, etc. While Trelis is a valuable tool with its wide material modeling capabilities, it lacks the specialized soft tissue constitutive models that FEBio provides. This tool will make the process of building complex models for FEBio easier for researchers studying biomechanics.

In the following documentation, you will find:

- Instructions for use
- Sample .febformat file
- Summary of .INP to .FEB mapping
- Summary of Trelis (CUBIT) commands to use for:
    - Defining element sets (.INP) and parts (FEBio/PreView)
    - Assigning material definitions to geometry
    - Defining contact interfaces and boundary conditions
- Differences in Geometrical Definitions between CUBIT and FEBio

A.1.2 Instructions for use

Please ensure that the following files are all located in the same directory:

- inp2feb.py – this is the main file from which the program can be launched
- inp2feb_module.py – this is the supporting module that contains many of the methods necessary for transcription
- At least one FEBio format file with the extension: '.febformat'

Once inp2feb.py is run, a GUI will open, as shown in the below figure:

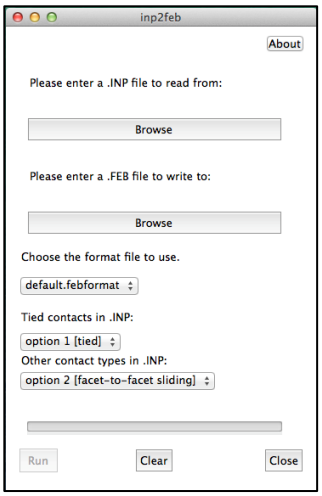

Figure 1. Screenshot of GUI

The GUI is designed to lead the user step-by-step from top to bottom to choose to options that they want implemented in the EFB file. Firstly, the 'About' button expands the window to give the user a brief set of instructions for the user to follow, as well as the purpose of the program. The expanded window looks as follows:

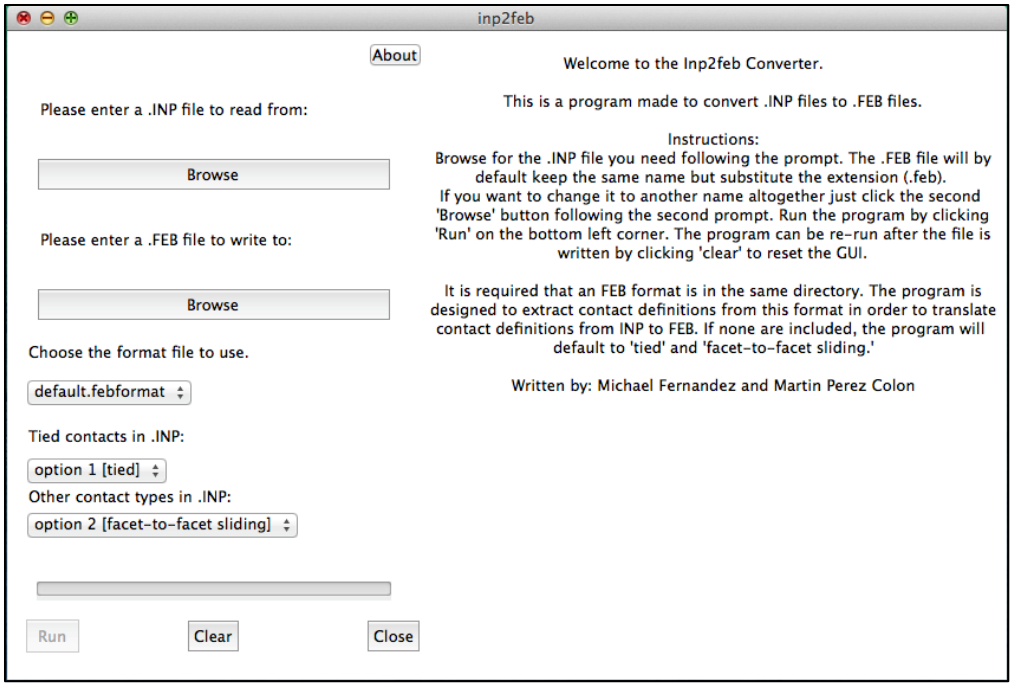

Figure 2: Screenshot of GUI with view of instructions when 'About' is selected

A.1.3 Table of widgets and their purposes

Browse Button	Opens a Finder window to allow the user to search for a .inp file to transcribe.
Format file dropdown list	Lists the FEBio format files in the directory where the program is run from. The program reads files with the extension, .febformat.
Contact dropdown lists	Allows the user to select a contact algorithm to use for particular contact definitions in the .inp file. Contact algorithms are found in the .febformat, which allows the user to fine tune the algorithms. Contact definitions are automatically updated if a new format file is selected. If no contact definitions are given, the program will use default definitions built into the program that are listed in the dropdown lists.
Run button	This button runs the program. It remains disabled until both the .inp file that's going to be read and the .feb file that the program will be written to are selected. Once run, the program displays the processes occurring above the progress bar.

Clear button	This button clears the choices that the user has selected. The Browse buttons revert back their initial state and the Run button is once again disabled. This allows the program to be used repeatedly.
Close button	Closes the program.

Once the .feb file is created, the format file that was used can be re-used. Once the program is finished and the .feb file is written, it is ready to be imported into PreView to be viewed or be processed with FEBio.

Further note on material definitions:

It is crucial that the material definitions listed in the .febformat file have the same name as the materials assigned to geometries in the .inp file. The program will map the material assignments accordingly, but unless the materials carry the same name (case sensitive) the program will not be able to carry out this task.

A.1.4 Sample .febformat file

The following is an example of a format file that can be used in xml format. The areas that are highlighted are important for the user to note, for these are the areas where the user will have to adjust and add to the code so that they transcribe a model with proper behavior and material properties:

```
<?xml version="1.0" encoding="ISO-8859-1"?>
 <febio_spec version="2.0">
     <Module type="solid"/>
     <Control>
         <time_steps>1000</time_steps>
         <step_size>0.001</step_size>
         <max_refs>5</max_refs>
         <max_ups>10</max_ups>
         <dtol>0.001</dtol>
         <etol>0.01</etol>
         <rtol>0</rtol>
         <lstol>0.9</lstol>
         <time_stepper>
             <dtmin>1e-009</dtmin>
             <dtmax>0.1</dtmax>
             <max_retries>30</max_retries>
             <opt_iter>10</opt_iter>
             <aggressiveness>1</aggressiveness>
         </time_stepper>
         <analysis type="static"/>
     </Control>
     <Globals>
         <Constants>
             <T>0</T>
             <R>0</R>
             <Fc>0</Fc>
```

```
        </Constants>
    </Globals>
    <Material>
<material id="1" name="some_material" type="EFD neo-Hookean">
            <E>0.01</E>
            <v>0.3</v>
            <beta>4,4,4</beta>
            <ksi>0.7,0.7,0.7</ksi>
        </material>
    </Material>
    <Geometry>
        <Nodes>
        </Nodes>
    </Geometry>
    <Boundary>
    </Boundary>
    <Loads>
    </Loads>
    <LoadData>
        <loadcurve id="1" type="smooth">
            <point>0,0</point>
            <point>1,1</point>
        </loadcurve>
    </LoadData>
```

#***Here the user should insert the various material properties that their geometries will exhibit. The program will automatically attempt to match the materials defined in the FEB format to the materials in the .INP file, and then apply the material to the relevant element***

```
    <Contact>
<contact name="option 1" type="tied">
            <laugon>0</laugon>
            <tolerance>0.2</tolerance>
            <penalty lc="2">0.1</penalty>
            <minaug>0</minaug>
            <maxaug>10</maxaug>
        </contact>
        <contact name="option 2" type="facet-
to-facet sliding">
            <laugon>0</laugon>
            <tolerance>0.2</tolerance>
            <penalty lc="3">0.1</penalty>
            <two_pass>1</two_pass>
            <auto_penalty>1</auto_penalty>
            <fric_coeff>0</fric_coeff>
            <fric_penalty>0</fric_penalty>
            <search_tol>0.01</search_tol>
            <minaug>0</minaug>
            <maxaug>10</maxaug>
            <gaptol>0</gaptol>
            <seg_up>0</seg_up>
        </contact>
    </Contact>
    <Output>
        <plotfile type="febio">
            <var type="contact gap"/>
            <var type="contact pressure"/>
            <var type="contact traction"/>
            <var type="displacement"/>
            <var type="stress"/>
        </plotfile>
```

Here are two examples of contact definitions that we have employed, but the user should define the kinds of contact that they wish to use in the model. Once read from the file and given to the user, the new .FEB file

```
    </Output>
</febio_spec>
                                (End of file)
```

A.1.5 Summary of useful Trelis (CUBIT) commands for creating .inp files for inp2feb

Fixed surface boundary conditions

```
create displacement on surface 4 5 6 dof all fix 0
```

Surface pressure boundary conditions

```
sideset 1 surface 1 2 3
sideset 1 name " pressure_surface"
create pressure name "pressure" on sideset 1 magnitude 10
```

Material definitions

To define a material and associate it with geometry in Trelis, you must create a material, create a block, add geometric bodies to the block, and associate the block with your material. A block will become an element set (ELSET) within the .inp file, and subsequently a “part” in FEBio.

Creating material definition:

```
create material "uterus" property_group "CUBIT-ABAQUS"
```

Creating block:

```
block 1 uterus
```

Assigning material to block:

```
block 1 material 'uterus'
```

Naming block (optional):

Note: If you name a block, the name you use will become the element set name in FEBio.

```
block 1 name 'uterus'
```

A.1.6 Contact interfaces

Before defining a contact interface, at least two contact regions must be created. The `create contact region` commands will automatically create sidesets, which you refer to by id number when defining the tied or sliding interface.

```
create contact region on surface 1 2
create contact region on surface 3 4
```

A.1.6.1 Tied contact between two surface regions

```
create contact pair master contact region 1 slave contact region 2 tied on
General off Exterior off
```

A.1.6.2 Sliding contact between two surface regions

```
create contact pair master contact region 1 slave contact region 2 tied off
General off Exterior off
```

A.1.7 Exporting the ABAQUS .inp file

```
export abaqus "my_model.inp" dimension 3 overwrite cubitids
```

A.2 Differences in Geometric Definitions between Trelis and FEBio

For the most part, geometry definitions are similar between Trelis and FEBio, but there are a few key differences. For these instances, the program has a module with a built-in library that allows the node numbering definitions to be translated.

Nodes are transferred with their locations and numbering staying the same. The differences in geometric definitions occur in how nodes are organized to form solid elements. Both programs recognize the same classes of structures: elements, element sets, node sets, surfaces, etc.; but there are multiple ways to define these structures, even with the same geometry. Take, for example, elements. In FEBio, they are defined as follows:

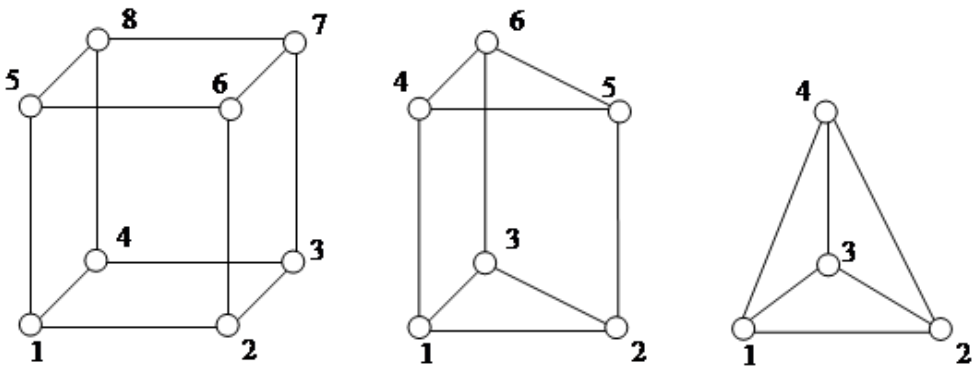

http://help.mrl.sci.utah.edu/help/index.jsp?topic=%2Forg.febio.help.febio_um%2Fhtml%2F3.8.2.html&cp=2_2_7_1

From left to right, the three different element types are: 8-node trilinear hexahedral (‘hex8’), 6-node linear pentahedral, also colloquially called ‘wedges,’ (‘penta6’), and the 4-node linear tetrahedral (‘tet4’). The conversion of node numbering for these fundamental types from Trelis to FEBio is supported.